CANMET

Canada Centre for Mineral and Energy Technology

Centre canadien de la technologie des minéraux et de l'énergie

Metals Technology Laboratories

Laboratoires de la technologie des métaux

Energy, Mines and Resources Canada

Energie, Mines et Ressources Canada

Canada

THE ENERGY OF OUR RESOURCES · THE POWER OF OUR IDEAS

L'ENERGIE DE NOS RESSOURCES · NOTRE FORCE CREATRICE

FLEET TECHNOLOGY LIMITED

E83382.FR

ENGINEERING CRITICAL ASSESSMENT OF A SERVICE-DAMAGED VESSEL

FINAL REPORT BY

L. Malik and M.J. Pates
Materials Technology Centre
A Division of FLEET TECHNOLOGY LIMITED
311 Legget Drive
Kanata, Ontario, K2K 1Z8

Work on this project was conducted under the auspices of
the Department of Energy, Mines and Resources

DSS FILE NUMBER: 009SQ.23440-8-9184

DSS CONTRACT NUMBER: 23440-8-9184/01-SQ

EMR SCIENTIFIC AUTHORITY: Mr. N. Smith

THIS WORK WAS SUPPORTED BY THE FEDERAL PANEL ON ENERGY R&D (PERD)

MICROMEDIA

117 pp

93-01533/

ACKNOWLEDGEMENTS

The authors would like to express their appreciation to the following organizations for technical and financial contributions:

Federal Government of Canada (Department of Energy, Mines and Resources - CANMET), Amerada Mineral Corp. of Canada, Amoco Corporation (Canada), Dow Chemical Canada Inc., Dow Chemical U.S.A., Esso Petroleum Canada, Fleet Technology Limited, Mobil Oil Canada, NOVA Corporation of Alberta, NOVACOR Chemicals (Canada) Ltd., Ontario Hydro Research Division, Petro Canada Products, Polysar Rubber Corp., PowerTech Research and Development, Shell Canada, Suncor Inc., Sun Oil, Syncrude Canada, Ultratest Canada.

The authors would particularly like to thank Dr. A. Glover (NOVA-Alberta), Mr. E. Sperling (Amoco-Canada), Mr. D. Oulton (NOVACOR Chemicals) and Messrs. N. Smith and R. Orr of CANMET for chairing the various sub-committees set up to guide the project to a successful completion, and for their constructive comments in compiling the final report.

TABLE OF CONTENTS - VOLUME I

Page

Abstract (iv)

1.0 INTRODUCTION 1

2.0 OBJECTIVES AND DESCRIPTION OF THE PROJECT 3

3.0 THE PRESSURE VESSEL HISTORY 4

4.0 PREPARATION OF VESSEL FOR PROGRAM 5

4.1 Background 5
4.2 Removal of Reinforcing Pads 5
4.3 Patch Removal and Repair 6
4.3.1 Patch Insert Procedure 6
4.4 Nozzle Closing Design and Procedures 6
4.4.1 Introduction 6
4.4.2 Method of Sealing Nozzles 7
4.4.3 Welding Procedures 7

5.0 NON-DESTRUCTIVE EVALUATION (NDE) 8

5.1 Magnetic Particle Inspection (MPI) 8
5.2 Manual UT Inspection - Task 1 (UT-1 and Task 2 (UT-2) 8
5.3 Automated UT Inspection 9
5.3.1 Technique A - Time of Flight Diffraction (TOFD) 9
5.3.2 Technique B - Automatic Pulse Echo 10
5.4 Observations 11

6.0 FRACTURE MECHANICS EVALUATION - PRELIMINARY ANALYSIS 12

6.1 Introduction 12
6.2 The CTOD Design Curve Approach 13
6.3 Collapse Analysis 15
6.4 Input Data 16
6.4.1 Flaw Sizes 16
6.4.2 Stresses 16
6.4.3 CTOD Fracture Toughness 17
6.5 Results and Concluding Remarks 18

TABLE OF CONTENTS (Cont'd)

Page

7.0 MECHANICAL PROPERTIES OF THE VESSEL STEEL AND WELDS .. 20

8.0 FRACTURE MECHANICS EVALUATION - DETAILED ANALYSIS 22

8.1 Introduction 22
8.2 Advantages of the Complex Analysis 22
8.3 Collapse Modified Strip Yield Model and the Failure Assessment Diagram 23
8.4 Input Data 26
8.4.1 Material Fracture Toughness Data (CTOD/CTOD-R Curves) 26
8.4.2 Crack Size 26
8.4.3 Stress Calculations 27
8.4.4 Stress Intensity Factor 28
8.5 Prediction of Burst Pressure for Failures From Various Defects 29
8.6 Observations and Predictions 31

9.0 BURST TEST 32

9.1 Preliminary Examination of the Burst Vessel 33
9.2 Strain Gauge Monitoring During the Burst Test 33
9.2.1 Background 33
9.2.2 Evaluation 33
9.2.3 Observations 34
9.3 Acoustic Emission Monitoring During the Burst Test 34
9.3.1 Background 34
9.3.2 Evaluation 35
9.3.3 Observations 37

10.0 POST-BURST TEST METALLURGICAL ANALYSIS 38

10.1 Introduction 38
10.2 Flaw Sizes 38
10.3 Metallurgical Examination of the Regions Containing Flaws 38
10.3.1 Splitter Plate End Flaw 38
10.3.2 Weld C3 Flaws 39
10.3.3 Demister Ring Flaw 39
10.3.4 Manway Reinforcing Pad Flaw 39

10.4 Summary 40

TABLE OF CONTENTS (Cont'd)

Page

11.0 DISCUSSION - POST-BURST TEST FRACTURE MECHANICS ANALYSIS 41

11.1 Introduction 41
11.2 Analysis 42
11.2.1 Burst Pressure 42
11.2.2 Propagation in Brittle Mode 44
11.2.3 Failure Initiation Site 45
11.3 Observations 47

12.0 GENERAL DISCUSSION 49

12.1 Non-Destructive Inspection for Sizing Flaws 49
12.2 Validity and Conservatism of the ECA Procedures Employed 52

13.0 CONCLUDING SUMMARY 54

14.0 REFERENCES 56

TABLES AND FIGURES

ABSTRACT

A Government-Industry collaborative program was carried out in Canada to validate an Engineering Critical Assessment (ECA) of a service damaged pressure vessel, culminating in a burst test in 1990. The vessel, a compressor knock-out drum, was selected as a typical example of pressure vessels presently being utilized in petrochemical plants. The non-stress relieved vessel had been in service for ten years in a wet hydrogen sulphide environment and flaws had subsequently been detected at or near several welds on the inner surface of the vessel.

During the project, non-destructive inspection was performed in order to characterize the flaws for length and depth, using Magnetic Particle Inspection (MPI) and manual Ultrasonic Inspection (UT). Two mechanized UT techniques were used in selected locations to provide additional data. ECA analyses were carried out at two levels of complexity using the flaw sizes estimated by the manual ultrasonic inspection. The preliminary analysis used the CTOD design curve approach for prediction of unstable fracture initiation and a separate plastic collapse analysis. The material toughness used in the analysis was lower bound, and estimated from data drawn from the literature. Actual material toughness determined from a patch removed from the vessel was used for the detailed analysis. The detailed analysis used was based on the collapse modified strip yield model, similar to Level 2 analysis in PD6493-1991.

The pressure vessel was next prepared for a hydrostatic burst test by welding in a replacement patch and sealing the nozzles. Linear strain gauges were placed at selected locations to monitor the membrane stress and acoustic emission sensors were employed with the objective of detecting the sites for crack growth and failure at an early stage.

A failure analysis of the vessel was conducted after completion of the burst test. Sections containing those defects that were considered as significant by the pre-burst test ECA analyses and characterized by the various UT techniques were removed from the pressure vessel and the actual crack depths measured. These measurements were then used for post-burst test fracture mechanics analysis.

This report presents the results of the non-destructive evaluation and the ECA analyses performed before the burst test, and compares them with the results obtained in the post burst test analysis. It was found that the manual ultrasonic inspection overestimated the flaw sizes. This, in conjunction with the assumption regarding the flow stress of the material, led to failure pressure predictions significantly below the actual burst failure pressure. Even with the use of actual flaw sizes, the predicted critical failure pressure represented a safety factor of ≈1.5 with respect to the burst pressure, indicating that the ECA methodology used gave a conservative assessment of flaws.

1.0 INTRODUCTION

The petro-chemical and energy utility industries require a methodology which will allow petroleum production, refining and the governing regulatory authorities to make technically and financially sound decisions for the repair or replacement of pressure vessels which suffer damage during service.

Engineering Critical Assessment (ECA) is a means for deciding on the necessity and timing of a vessel repair or replacement. ECA procedures, which are based on the principles of fracture mechanics, can be used to assess the risk of operation of a damaged vessel by predicting the amount of damage which can lead to premature failure, and thus determine the need for repair or replacement of a vessel. The total cost to repair or replace a damaged vessel can be high not only in terms of the economics of repair, but also that of lost production and safety of workers and the public. Considerable savings can thus be realized if unnecessary and unscheduled shutdowns can be avoided.

Valid ECA procedures would allow both the owners and insurance underwriters of pressure vessels to assess the integrity of the vessel, thereby avoiding costly and unnecessary repairs, and at the same time, reducing the probability of failure during service to an acceptably low level.

In general, pressure vessels of interest to the members of this program are fabricated and operated under the jurisdiction of the various Canadian Provincial authorities. These authorities have adopted CSA Standard B51-Boiler, Pressure Vessel and Pressure Piping Code [1]. This standard, in turn, incorporates the provisions of the ASME Boiler and Pressure Vessel Code.

This program was focused on moderately thick pressure vessels typically fabricated from SA516 Grade 70 material up to 38 mm in wall thickness, which are generally not required to be stress relieved as per the ASME Code. These vessels are normally built and operated under the provisions of ASME Code Section VIII - Pressure Vessels [2,3]. Elements of an ECA methodology are already incorporated into some sections of the ASME Code, but are particular to the sections regulating nuclear vessels (Section III and Section XI) [4,5]. However, these procedures are currently based on linear-elastic fracture mechanics and may not be suitable for the vessels (generally $\leq$38mm) which are the subject of the work described herein.

A three year Government-Industry collaborative program was therefore launched in Canada in 1988 to validate an engineering critical assessment (ECA) approach for a service-damaged pressure vessel, of which a key component was a burst test performed in 1990. The pressure vessel, a knock-out drum, was selected as a typical example of the plain carbon manganese pressure vessels currently being utilized in North American process plants. Cracking was detected at several weld locations on the inner surface of the vessel after ten years of wet hydrogen sulphide service. The cracking was so extensive that the vessel was subsequently withdrawn from service.

This report presents the results of the non-destructive evaluation and ECA analyses carried out, and compares them with the results given by the analysis performed after the vessel had been hydrotested to failure and actual flaw sizes measured by post-burst test metallurgical analysis. The report also comments on the validity of the methods for the application of ECA to this type of vessel.

2.0 OBJECTIVES AND DESCRIPTION OF THE PROJECT

A cooperative program between the Metals Technology Laboratories of CANMET and a number of representative organizations from the petroleum, gas transmission and electric utility industries* was initiated with the objective to assess the validity and conservatism of an engineering critical assessment (ECA) approach when applied to a pressure vessel containing damage induced by sour service. The program comprised the following four stages:

(a) a non-destructive inspection of the vessel to locate and fully characterize planar flaws in the pressure vessel. The techniques employed included those commonly used in the industry at shut downs (magnetic particle inspection (MPI) on both inner and outer surfaces, and manual ultrasonic inspection (UT) of all weld zones) as well as some more sophisticated mechanized ultrasonic (A-UT) techniques at selected weld zones;

(b) fracture mechanics predictions to estimate the critical pressure to cause vessel failure from the existing flaws. A preliminary analysis used membrane stresses and lower bound crack tip opening displacement (CTOD) values from the literature. The more detailed analysis used measured mechanical property values (including CTOD-R curves) and more complex stress analysis. The flaw sizes used in both approaches were those sized by manual UT inspection;

(c) a hydrostatic burst test of the pressure vessel to failure; the vessel was monitored by acoustic emission, strain gauges and pressure transducers.

(d) a post-burst test analysis to determine actual flaw sizes in order to establish the level of conservatism in the fracture mechanics approach and to assess the accuracy of the selected NDE methods.

---

* The industry organizations financially supporting the program were: Amerada Mineral Corporation of Canada; Amoco Corporation (Canada); Dow Chemical (U.S.A.); Esso Petroleum, Canada; Mobil Oil, Canada; Nova Corporation of Alberta; NOVACOR Chemicals (Canada) Limited; Ontario Hydro Research Division; Petro Canada Products; Polysar Rubber Corporation; Power Tech Research and Development; Shell Canada; Suncor Inc.; Syncrude Canada.

3.0 THE PRESSURE VESSEL HISTORY

The pressure vessel was a compressor knockout drum and was fabricated in 1975 to ASME Section VIII - Division 1 (1974) design rules using SA 516 Gr 70 steel in the 'as-rolled' condition for the shell, and as forged and heat treated condition for the heads. The vessel was donated by a member of the consortium, and can be considered as being representative of vessels in sour service at that time. It was approximately 6m long and 1.8m diameter, with a nominal wall thickness of 28.6mm. All major circumferential and longitudinal welded joints were fabricated using the submerged arc welding process, whilst welding of the nozzles and attachment fillets utilized both flux cored and shielded metal arc processes. The vessel was not stress relieved on completion of fabrication and thus entered service in the "as-welded" condition.

Figure 1 illustrates all the welded seams and major nozzle locations; it also shows the position of four internal fillet welds. Fillet welds F1 and F2 attached a demister support ring to the internal vessel wall and both welds were continuous. Fillets S1 and S2 attached a splitter plate to the internal wall adjacent to the nozzle inlet at N1.

The vessel was placed in sour service in 1976, operating at a temperature of 38°C and a pressure of about 3000 kPa. The vessel remained in service until 1986 when cracks were detected at the following four areas on the internal surface, using fluorescent magnetic particle inspection.

(a) Fillets F1 and F2
(b) T-joints at both V1 and V2 intersections with circumferential weld C2.
(c) Manway to vessel weld MW1.
(d) Circumferential weld C3.

The vessel was subsequently repaired by welding but within one year further cracking had appeared in the repaired locations and at additional weld areas. Repairs were again performed and the areas monitored with both Magnetic Particle and Ultrasonic Inspection techniques at one month intervals.

A reinforcing ring over fillets F1 and F2, and an additional reinforcing pad over MW1 were installed on the external surface in the Fall of 1987 but a further inspection in November of the same year showed additional cracking throughout the vessel interior. The cracking was considered to be so extensive that the vessel was withdrawn from service in January 1988.

4.0 PREPARATION OF VESSEL FOR PROGRAM

4.1 Background

When the vessel was received, it was found that there were several areas that required refurbishing. This was necessary in order to be able to prepare the vessel for satisfactory NDE, to provide vessel material properties evaluation and to prepare the vessel for the hydrostatic burst test. Initially, the vessel was sand blasted over its complete inner surface and over the weld areas on the outside surface. The following tasks were then undertaken.

4.2 Removal of Reinforcing Pads

As previously mentioned, the vessel had had additional reinforcements attached to the outside surface during service. It was decided to remove these for two reasons: first, to allow proper access for the NDE procedures from the outside surface, and secondly, to return the vessel to its original design geometry. The reinforcements removed were:

(a) a full encirclement band on the outside of the shell corresponding to demister ring fillet welds F1 and F2 (see Figure 1). The band was made up of four sections of 38mm plate, each section being butt welded together onto a 3mm thick backing bar such that there was no penetration into the vessel wall at these welds. The band was attached to the outside wall by circumferential fillet welds (20mm leg length) on either side of the band.

The band was removed by air-arc gouging the fillets to within 2.5mm of the vessel wall and finally by grinding to the root of the fillet. The butt welds were air-arc gouged to the interface with the backing bar and each backing bar ground out to remove each quarter section of the band.

The weld areas on the vessel shell were ground smooth and inspected by MPI. Several linear indications were recorded and these were removed by grinding to a maximum depth of 1.5mm.

(b) an additional pad attached to the original reinforcement pad around Manway MW1. This additional reinforcing pad was 25mm thick and attached by fillet weld to the nozzle neck and the original repad. It was removed and ground areas tested by MPI in the same manner as the reinforcing band described previously.

Figure 2 depicts the vessel with the reinforcing band at F1/F2 removed but the second re-pad at MW1 still in position.

4.3 Patch Removal and Repair

Based on the results of the initial MPI and manual ultrasonic inspections, an area of the shell free of flaws was removed to provide the test specimens for material properties. It was also ensured that this area included material from both the can sections, and longitudinal and circumferential welds and their associated heat affected zones. The location of the patch removed is shown in Figure 3 and the procedure for its replacement with new material is briefly summarized below.

4.3.1 Patch Replacement Procedure

A replacement patch (dimensions of 800 X 900 X 28.5mm) was prepared from the same specification material as the shell wall (SA516 Gr 70) and was rolled to the contour of the pressure vessel. The insert plate and the pressure vessel shell were prepared with a joint design consisting of a 60-75° included angle bevel, 5mm land, and a 3-6mm root opening. The area around the cut-out in the pressure vessel shell was subjected to a hydrogen bake-out treatment and the patch insert preset to the outside of the pressure vessel by ~2.4mm to allow for anticipated distortion and contraction during welding. Finger bars were used to fair the insert plate and two additional strongbacks were welded to the corners of the patch and pressure vessel shell as shown in Figure 4.

The pressure vessel shell and the patch insert plate were fitted with heating elements and insulating blankets (Figure 5), and prior to welding, the preheat temperature was stabilized at ~204°C.

All welding was completed in the flat (1G) position using 3.2mm, E48018-1 (AWS E7018-1) electrodes. Magnetic particle inspection was carried out after backgouging the root and MPI, RT and UT inspection was performed on completion of welding.

4.4 Nozzle Closing Design and Procedures

4.4.1 Introduction

Prior to hydro testing, all nozzles on the vessel apart from those selected for fill and vent, had to be designed and detailed for pressure seal at an anticipated maximum pressure of 12,700 kPa.

4.4.2 *Method of Sealing Nozzles*

Design calculations determined that the existing flanges could not withstand the maximum anticipated test pressure of 12,700 kPa and a decision was made to discard them. To avoid bolting and the possibility of leaking gaskets, two alternatives were considered:

(1) Cut off the flanges and provide each nozzle with a weld cap, or

(2) leave the flanges intact and insert flat blanks into each nozzle.

Option (2) was considered as being the preferred method.

The material used for the blanks in the design calculation was SA516-70 plate using a specified minimum yield stress of 265 MPa.

Calculations were made using methods and formulas given in ASME Section VIII, Division 1, paragraph UG-34 [6]. The method of attachment and minimum weld sizes were in accordance with Figure UG-34(g), and all welds at nozzle blanks were checked for minimum throat dimensions required by UG-34(g) as well as for adequate strength in shear using a 60% efficiency factor.

Each nozzle was checked for the presence of sufficient reinforcement in accordance with paragraph UG-41 of ASME Section VI-A, Division I [7]. In performing the calculations, 12,700 kPa was used as the maximum design pressure and the specified minimum tensile stress of 480 MPa and 410 MPa were used for the plate and pipe materials respectively.

4.4.3 *Welding Procedures*

All welding of blanks, inlet and vent nozzles was performed using approved welding procedures. Arc starts and craters, as well as all completed layers, were peened and ground. Dry magnetic particle inspection was performed after deposition of the root beads, after filling in about half the joint thickness, and after the capping passes had been deposited. Figure 6 depicts the MPI of the root pass on the sealing of manway nozzle MW1, which was the last to be sealed.

5.0 NON-DESTRUCTIVE EVALUATION (NDE)

Non-destructive testing (NDE) was performed on the pressure vessel as part of the overall project. The NDE was carried out in accordance with typical industry practice in order to establish planar flaw depths and lengths for the fracture mechanics predictions. A further objective was to demonstrate the viability of current industry practice to provide data for an ECA methodology.

The NDE consisted of MPI, manual UT of all weld zones, and two mechanized ultrasonic techniques used in selected areas.

5.1 Magnetic Particle Inspection (MPI)

Magnetic Particle Inspection of the pressure vessel was conducted according to ASME Section V, Article 7 and all welds were inspected internally using wet fluorescent magnetic particle and externally using black magnetic ink onto a white background lacquer. All indications were measured and recorded. Selected indications on the inside surface were photographed.

A magnetoscope with an adjustable yoke using continuous AC current was used for all MPI inspection.

5.2 Manual UT Inspection - Task 1 (UT-1) and Task 2 (UT-2)

Manual UT inspection of the pressure vessel was conducted according to ASME Section V, Articles 4 and 5, using the pulse-echo technique [8].

All ultrasonic scanning was performed from the vessel outer surface with the exception of flaw sizing at nozzles MW1 and N3.

Forty-five degree (45°) and sixty degree (60°) shear wave transducers were used on all major longitudinal and circumferential welds V1, V2, C1, C2 and C3. Sixty degree (60°) shear wave transducers were used for the reinforcement fillet welds at nozzles N1, N1A, N2, N3 and MW1.

Flaw depths were measured where possible using the 6 db 'drop off' method, with a 60° shear wave transducer of 2.25 MHz, 13mm square with a 25mm shoe.

The overall results of both the MPI and manual UT inspection are given in Table 1 'Weld Flaw Summary'.

The results of this manual UT inspection were used in the preliminary and detailed fracture mechanics evaluations. From the preliminary analysis, several flaws were identified as of significance, and the detailed results of the manual UT for five of these principal 'cracks' are shown in Table 2.

After the results of both mechanized UT techniques (described in Section 5.3 below) were reviewed, a second manual UT inspection was conducted on selected areas of fillets F1 and F2 and on the defect described as #19 associated with weld C3. The data from the second manual inspection of F1 and F2 could, therefore, be directly compared to the results given by both automated techniques.

The results of the second manual examination are also shown in Table 2, and photographs of typical cracks referred to in this table are shown in Figures 7 to 10 inclusive.

5.3 Mechanized UT Inspection

Mechanized ultrasonic inspection was performed using two different techniques on the same areas of the vessel. These areas were the fillet weld toes at the demister ring, and selected on the basis of the preliminary fracture mechanics evaluation which indicated that the cracks at the toes of these welds could be critical. (Refer to Section 6.0 of this report for a review of the preliminary fracture analysis.)

5.3.1 Technique A - Time of Flight Diffraction (TOFD)

Technique A employed a UT inspection system originally developed for accurate crack sizing and characterization in nuclear components. This system was used in pulse-echo and crack-tip diffraction modes. For Time Of Flight Diffraction (TOFD), a 10 MHz compression wave transducer was used on 45° and 60° wedges, and for pulse-echo, both compression wave and 45° shear wave transducers of 4 MHz were used. In addition, the on-line data processing facilities enabled real-time imaging in a variety of formats.

In the pulse-echo mode, Technique A performed conventional 'code-compliant' inspection. The on-line display was a conventional waveform, with amplitude and time-base scales, similar to that used for the previously described manual ultrasonic inspection.

The main advantage of Technique A for crack sizing was the Time Of Flight Diffraction (TOFD) mode. TOFD relies solely on the time separation between signals diffracted from the crack tip rather than reflected energy. The technique does not rely on the amplitude of the response and is thus independent of the quality of the coupling, the material attenuation, and the defect orientation. In addition, a broad beam of energy is used, and the accuracy is therefore not dependent on the focus of the transducer.

A real-time image was presented along the weld axis, allowing the operator to monitor the inspection by showing the true length of the defect and an indication of the location and depth. The actual crack depth was determined later, during off-line processing of the data.

The crack depths at F1 and F2 were measured from the outside surface of the pressure vessel using a pair of transducers moved parallel to the weld seam in a 'pitch and catch' format and utilizing a motorized transducer manipulator similar to the method illustrated schematically in Figure 11. The same zero (0) datums as for the manual inspection were used in order to compare the data. The results are given in Table 3 together with the data from the other UT work as a comparison.

In addition, a 1.2m length of circumferential seam weld C2 was selected by the project team as a blind test where MPI and manual UT had shown no reportable indications. Mechanized inspection using TOFD supported the manual data wherein no planar flaws were recorded, the only reportable indications being two slag inclusions located in the weld body.

An attempt was made using the equipment available to examine the manway nozzle MW1. However, the attempt was unsuccessful due to geometry restrictions and the presence of a second reinforcement pad.

5.3.2 Technique B - Automatic Pulse Echo

Technique B also employed a mechanized UT inspection system developed for accurate crack sizing and imaging. The system is capable of single or multi channel operation in pulse-echo or tandem modes. The on-line data processing facility also enabled real-time imaging in a variety of formats.

Welds F1 and F2 were selected for examination in order to directly compare the results with the other techniques, again using the same datum point. The cracks were characterized from the outside surface of the pressure vessel using a pair of 45° shear wave transducers moved parallel to the weld seam in a pitch and catch mode, and using a motorized manipulator similar to that used in Technique A. The flaws were sized for depth using a db drop off method and shear wave probes of 4 MHz frequency.

A-Scan data was obtained using a mechanized weld scanner with one angle transducer chosen. The scan was carried out from both sides of the X axis (near and far side) in the same manner as for the two angle transducer scan.

The crack depths were calculated using digitized A-Scan data collected by the multi-transducer array and computer imaging software, utilizing the synthetic aperture focusing technique. The technique was based on a statistical-geometrical reconstruction scheme, utilizing echo amplitude and transit time information. For a given view type, the technique generated a reflector probability distribution corresponding to the selected plane. The probability distribution was computed from probe position and echo range data for all probe positions included in the reconstruction. The results are shown in Table 3.

5.4 Observations

The results of all ultrasonic inspections are given in Table 3. It can be seen from these data that, in general, the manual UT technique estimated the defects to have the largest depths, while the mechanized Technique A (TOFD) defined the defects as being significantly shallower. The second mechanized method, Technique B, estimated defect depths to be in between these two extremes.

The accuracy of each of these methods is fully discussed in Section 11.0 of this report which includes the actual crack depths determined in the post-burst test analysis.

6.0 FRACTURE MECHANICS EVALUATION - PRELIMINARY ANALYSIS

6.1 Introduction

On completion of the magnetic particle and manual ultrasonic inspections, a preliminary fracture mechanics analysis was performed in order to predict the possible locations of failure, failure pressure and failure mode during the hydrostatic burst test.

All the calculations were based on the CTOD design curve approach and used fracture toughness data extracted from the literature and not the actual vessel material properties. This is frequently the case in practice since at the time of the engineering critical assessment the material property data, if established at the time of fabrication, may not be easily accessible.

The CTOD design curve approach followed was that of the original BSI Published Document 6493-1980 [9], a document which has been used successfully and extensively around the world for engineering critical assessments. Also, Davey and Garwood [10] have shown that under elastic-plastic conditions, for ductile tearing at least, CTOD appears to better characterize the crack growth resistance under biaxial loading than does the J-integral.

A separate collapse analysis was also performed which in conjunction with the CTOD design curve approach, is equivalent to the Level I analysis in PD6493-1991.

6.2 The CTOD Design Curve Approach

The CTOD design curve assessment method utilizes fracture toughness data generated from small-scale test specimens to assess the risk of fracture. The assessment aims at determining safe allowable defect sizes rather than their critical values. The fracture assessment is carried out using the following equations:

$$\delta = \frac{2\pi\bar{a}\sigma_{ys}}{E}\left(\frac{\sigma_1}{\sigma_{ys}}\right)^2 \quad \text{for } \sigma_1 \leq 0.5\sigma_{ys} \qquad [6\text{-}1a]$$

$$\delta = \frac{2\pi\bar{a}\sigma_{ys}}{E}\left(\frac{\sigma_1}{\sigma_{ys}} - 0.25\right) \quad \text{for } \sigma_1 > 0.5\sigma_{ys} \qquad [6\text{-}1b]$$

where

δ = crack tip opening displacement (CTOD)

$\bar{a}$ = half length of an allowable through thickness defect

σ_{YS} = yield strength

σ_1 = effective applied stress, taken to be $\sigma_a K_t + \sigma_R$

σ_a = applied stress

σ_R = residual stress

K_t = stress concentration factor

For a given surface crack of known dimensions, the $\bar{a}$ parameter can be derived from Figure 12 in BSI PD 6493:1980 [9]. The applied stress, σ_a, is a function of internal pressure of the vessel and, in the present case, was calculated using standard thin shell formulae for axial and hoop stresses as follows:

$\sigma_a = \frac{PD}{4e}$ for a circumferential crack, [6-2a]

$\sigma_a = \frac{PD}{2e}$ for an axial crack, [6-2b]

where P = internal pressure of vessel
D = diameter of the vessel
e = thickness of the wall of the vessel

By substituting for σ_a into Equation [6-1], crack driving force plots (i.e. applied CTOD as a function of internal pressure) can be obtained. Knowing the material toughness therefore, these plots can then be used to infer the failure pressure (see Figure 12, for example).

6.3 Collapse Analysis

A separate analysis is carried out to assess the risk of plastic collapse of uncracked ligaments, and this was performed at the time using the methodology [11] given in the proposed revisions to BSI PD 6493:1980 [10] (now issued as BSI PD 6493:1991). Plastic collapse of the material adjacent to the defect under consideration (i.e. the ligament ahead of a surface crack) occurs when the S_r value, defined as the ratio of the effective net section stress, σ_n and the flow strength of the material exceeds 0.8. Flow strength is assumed to be the average of yield and ultimate strengths up to a maximum of 1.2 σ_{YS}. For a surface crack in a plate under normal bending restraints, the effective net section stress is given by:

$$\sigma_n = \frac{P_b + \sqrt{[P_b^2 + 9P_m^2 (1 - \alpha)^2]}}{3(1 - \alpha)^2} \qquad [6\text{-}3]$$

$$\alpha = \frac{a}{e} \cdot \left(1 + \frac{e}{c}\right)^{-1} \quad W \geq 2(c + e)$$

$$= \frac{2a}{e} \cdot \frac{c}{W} \quad W \leq 2(c + e)$$

where

P_b	=	primary bending stress
P_m	=	primary membrane stress
a	=	depth of surface defect
c	=	half length of a surface defect
e	=	wall thickness
W	=	plate width

The above treatment of net section stress was considered to be reasonable for internal surface defects in shells subjected to internal pressure [10].

6.4 Input Data

6.4.1 Flaw Sizes

The crack size dimensions used in the calculations were those given by the magnetic particle and manual ultrasonic inspections as described in Section 5.0. Dimensions of the local geometries in which the cracks were located were taken from either the original fabrication drawings or from measurements direct from site. Figures 13a-13g illustrates the crack size models assumed in the calculations.

It should be noted that where complex arrays of cracks were present, the deepest and the longest crack was taken as the representative case. In this respect, the cracks at the toes of the demister ring fillet welds (F1 and F2), Figure 13a, were taken to be represented by a single fully circumferential crack with a depth of 7.62mm. Similarly, in the vicinity of the circumferential weld, designated as C3, there was an array of small circumferential and axial cracks. Consequently, all the circumferential cracks were represented by a single 3.56mm deep, 203mm long crack, (Figure 13b(i)). The axial cracks were similarly modelled by a crack 7.62mm deep and 95.25mm long. These assumptions were therefore conservative.

Other cracks are described in the remaining illustrations in Figure 13. For those cracks which showed extensive curvature or complex shapes, e.g. around the splitter plate fillets (S1 and S2) or the manway (MW1), the worst case defects perpendicular to or parallel to the pressure vessel axis were used.

6.4.2 Stresses

The far field membrane stress perpendicular to the defect was calculated using Equation [6-2]. For defects located at toes of fillet welds, e.g. demister ring cracks at F1 and F2, the stress concentration factor, K_t, was reduced from 3 to 1 when defect depths exceeded 0.15 x wall thickness [9]. No standard K_t factors were cited for defects located at the manway (MW1). Consequently, numerical analysis was performed for this region assuming that both the manway and the pressure vessel were internally pressurized. Stress concentration factors were obtained as a function of distance away from the manway nozzle pipe in the direction parallel to the pressure vessel axis. It was found that for manway defect 1, assumed to be located 50mm away from the manway nozzle pipe, (see Figure 13g), K_t was evaluated to be 1. For manway defect 2, a value of 1.6 was calculated. These values were then used in the fracture mechanics calculations. For all other defects, K_t was assumed to be 1.

Fracture mechanics analysis requires input of residual stress which may have been induced as a result of welding. Yield magnitude residual stresses are normally assumed to be present in a vessel that has not been post weld heat treated. It was believed that this assumption was far too conservative for the present vessel, which had been subjected to several pressure tests during its service life.

Research and experience with other vessels has shown that principal benefits of pressure testing of cracked components is the relief of residual stresses accompanied by an increase in fracture stress. Further, with regard to cracking at toes of fillet welds in pressure vessels, Dunmore and Parlane [12] have shown that cracks with depths greater than 0.15 x wall thickness generally tend to lie in a compressive residual stress field. Their work allowed for the effect of in-service hydrotest, and on the basis of their results, it was considered reasonable to assume that for cracks in the present vessel, the residual stress component was zero.

However, in order to assess the significance of the residual stress input, additional calculations were carried out assuming the presence of either half-yield or quarter-yield level residual stresses.

6.4.3 CTOD Fracture Toughness

Details of the welding procedures for this vessel were not available, but the mill test reports for shell material and the semi-elliptical heads were obtained. These, however, did not contain toughness data. The vessel was made from ASME SA 516 Grade 70 hot rolled steel for the shell and the heads had been hot forged. The chemical analysis and strength details as taken from the mill sheets are given in Table 4.

The information given in Table 4 was used to carry out a literature search for fracture toughness data for the ASME SA516 Grade 70 steel. A similar search for the weld metal was not carried out since exact details of the welding procedure were not available. The results of the literature search are given in Table 5. It was considered that since the fracture toughness data for parent steel would also be used for weld metal, and since the actual vessel steel and welded regions may have deteriorated as a result of hydrogen charging, lower bound data were needed. In this respect, Bellamy's Charpy data at 0°C was used and then converted to CTOD using the Barsom and Rolfe's [13] correlation:

$$\frac{K_{IC}^2}{E} = 0.221\ (C_v)^{1.5} \qquad [6\text{-}4]$$

Assuming plane strain conditions for conservatism:

$$\delta = \frac{K_{IC}^2}{2\sigma_{ys}E} \qquad [6\text{-}5]$$

Thus

$$\delta = \frac{0.221\ (C_v)^{1.5}}{2\sigma_{ys}} \qquad [6\text{-}6]$$

Assuming a value of 21J for Charpy energy and 340 MPa for yield strength, Equation [6-6] resulted in a CTOD toughness of 0.031mm. This value of fracture toughness was believed to be conservative and was used for cracks located in weld metal, heat affect zone and parent steel.

6.5 Results and Concluding Remarks

Typical plots of CTOD crack driving forces for two defects are shown in Figure 14. The plots indicate a failure pressure due to unstable fracture (assumed to occur at a CTOD of 0.031mm) and also due to plastic collapse. This information has been summarized in Table 6 for the zero residual stress assumption.

It can be seen that failure by fracture at a pressure of 5.1 MPa was predicted at axial cracks in weld C3 (Figure 14a). It should be recalled that at this location, the small intermittent cracks were assumed to be represented by a single larger crack, 95.25mm long and 7.62mm deep (Figures 9 and 13(b)). Although this assumption could be too severe for a majority of C3 axial cracks, their tips appeared to lie in the weld heat affected zone, which could have a low fracture toughness. Failure by fracture from this region, therefore, could not be ruled out.

The next crack that was predicted to cause fracture at a pressure of 6.7 MPa was the manway crack #4 (Figure 13g). This crack represented radial defects located at the edge of the manway inlet pipe. Fracture analysis was performed assuming an edge crack in a 125 mm wide, 12.7 mm thick plate, subjected to tensile loading. It was believed that any unstable propagation of these cracks was likely to be arrested when the propagating crack reached the wall of the pressure vessel. In this respect, it was considered that catastrophic failure of the vessel from these defects was unlikely. This supposition was further strengthened by the belief that the edge crack in flat plate treatment of these defects would be very conservative.

The axial crack associated with weld C1 was the next predicted defect to cause failure (Figure 13c). As with axial cracks in weld C3, the tips appeared to be residing in the weld heat affected zone and due to potential low toughness, failure by fracture could not be ruled out.

The largest defects located and sized by manual NDE were at the toes of the demister ring fillet welds (F1 and F2). This analysis indicated that these cracks would cause fracture at a pressure of 8 MPa. The manway defects 1 and 2 followed closely behind with fracture being predicted at pressures of 8.5 MPa and 8.8 MPa respectively. For manway defect #1, further calculations were carried out assuming that the crack lay in the pressure vessel wall alone and did not see the effect of the repad. In this case, the fracture pressure was computed to be 4.9 MPa and plastic collapse pressure to be 12.8 MPa.

In light of the assumptions made regarding the effective flaw sizes to arrive at the results given in Table 6, and considering that the fracture toughness of the whole of the vessel could have deteriorated significantly due to hydrogen embrittlement, it was considered that unstable fractures could initiate from any one of the sites discussed above. The most likely sites for failure were the cracks at demister ring fillet weld toes (F1 and F2), manway welds, and axial cracks located at circumferential welds C1 and C3.

However, if the fracture toughness of vessel materials had not deteriorated significantly and was high, plastic collapse could dominate. In that case, plastic collapse is predicted to take place at axially oriented defects in the following order: cracks at welds C3, C1, V2 and axial cracks at the splitter plate fillet welds S1 and S2 (Figure 14b). The plastic collapse pressures of these cracks were predicted in the range 8.6 to 9.9 MPa which is approximately three times the operating pressure of the vessel.

7.0 MECHANICAL PROPERTIES OF THE VESSEL STEEL AND WELDS

In order to proceed to the detailed fracture analysis, using a more complex fracture mechanics approach, it was necessary to determine the actual properties of the pressure vessel. The patch removed from the vessel, as described in Section 4.3, was subsequently reduced in size and several coupons removed from this area as defined in Figure 15. The removed specimens were tested to give the following data:

(i) weld metal tensile properties for weld C2 (see Table 7 for results).

(ii) base material tensile properties using one specimen each aligned parallel to, and transverse to the circumferential weld C2 (see Table 7 for results).

(iii) CVN toughness of weld metal (welds C2 and V1), heat affected zone (welds C2 and V1), and base material with specimens oriented both parallel to and perpendicular to weld C2 (see Table 8 for results).

(iv) CTOD-R curve data for weld metal C2, HAZ (weld C2) and base material with specimens oriented parallel as well as perpendicular to weld C2. A set of three specimens was tested at room temperature for each location (see Table 9 for data).

For predicting the instability behaviour during the burst test, an average CTOD-R curve for each location was needed. This was done by fitting a parabolic equation to the CTOD curves such that

$$\text{CTOD (mm)} = k\,(\Delta a)^n \qquad [7\text{-}1]$$

where Δa was the crack growth. The constants k and n for each curve are reported in Table 9. The average CTOD-R curve was then represented by the equation

$$\text{CTOD (mm)} = k_{avg}(\Delta a)^{n_{avg}} \qquad [7\text{-}2]$$

Analysis of the data showed that the CTOD-R curve for specimens parallel to the pressure vessel axis was higher than that for specimens oriented parallel to the hoop stress. Further, the comparison of the average CTOD-R curve showed that the resistance to fracture could be ranked as follows:

Base Material (axial stress) > Base Material (hoop stress) > Heat Affected Zone > Weld Metal

The rankings based on CVN toughness is different (see Table 8), presumably because of differences in yield strength of materials being sampled.

8.0 FRACTURE MECHANICS EVALUATION - DETAILED ANALYSIS

8.1 Introduction

In Section 6.0 predictions based on a preliminary analysis, viz, the CTOD design curve and plastic collapse analysis corresponding to Level 1 in the proposed revisions to PD6493:1980 [11], were presented. These were deemed to be too conservative, primarily because of the lower bound fracture toughness (.031 mm CTOD) assumed for all the material containing cracks.

This section presents the predictions of a detailed analysis based on the Collapse Modified Strip Yield Model (Level 2 analysis in the proposed revisions to PD6493 and now issued as PD6493:1991).

8.2 Advantages of the Detailed Analysis

The advantages of the detailed over the preliminary analysis reported in Section 6.0 are:

(i) It is not empirical as is the CTOD design curve approach for applied stress greater than 0.5 yield strength;

(ii) The plastic collapse solution is already incorporated whereas the preliminary analysis requires a separate assessment in this regard;

(iii) The CTOD design curve has a variable safety factor inherent in it, whereas the detailed analysis has none.

(iv) In the CTOD design curve approach, the treatment of stress is conservative in that it is assumed that there exists a uniform tensile stress, equal to the maximum tensile stress across the section.

By using the actual fracture toughness of the region of interest and a more accurate stress analysis, and due to the absence of a built-in safety factor, the detailed approach reduces the degree of conservatism inherent in the preliminary analysis, and provides a critical assessment.

8.3 Collapse Modified Strip Yield Model and the Failure Assessment Diagram

The CTOD, δ, ahead of a crack in a thin plate (plane stress condition) based on Garwood's modification of the original strip yield model for collapse (assuming elastic-perfectly plastic material) is given by the equation:

$$\delta = \frac{8}{\Pi} \cdot \sigma_f^2 \cdot \frac{a}{E \cdot \sigma_y} \ln \cdot \sec\left(\frac{\Pi}{2} \cdot S_r\right) \qquad [8\text{-}1]$$

From Equation [8-1] above, the author has developed a failure assessment diagram (Figure 16) whose locus is described by the equation below.

$$\sqrt{\delta_r} = \sqrt{\frac{\delta_I}{\delta_{mat}}} = S_r\left\{\frac{8}{\Pi^2} \cdot \ln \sec \cdot \left(\frac{\Pi}{2} \cdot S_r\right)\right\}^{-1/2} \qquad [8\text{-}2]$$

where δ_I = crack opening displacement induced at the crack tip, assuming linear elastic fracture mechanics conditions prevail; and is given by $\{(K_1^P)^2/\sigma_y \cdot E\}$, K_1^P being the applied stress intensity.

δ_{mat} = material fracture toughness measured in terms of CTOD,

S_r = σ_n/σ_f,

σ_n = effective stress on the net section of the material ahead of the flaw, and for surface crack in a plate under normal bending restraint is given by:

$$\sigma_n = \frac{P_b + \sqrt{[P_b^2 + 9P_m^2 (1 - \alpha)^2}}{3(1 - \alpha)^2} \qquad [8\text{-}3]$$

$$\alpha = \frac{a}{e}\left[1 + \frac{e}{c}\right]^{-1} \qquad W \geq 2(c + e)$$

$$= 2\frac{a}{e} \cdot \frac{c}{W} \qquad W \leq 2(c + e)$$

P_b	=	Primary bending stress
P_m	=	Primary membrane stress
c	=	half length of surface flaw
e	=	wall thickness
W	=	plate width
σ_f	=	flow stress at plastic collapse (assumed to be the lower of $1.2\sigma_y$ or $0.5(\sigma_y + \sigma_u)$
σ_y	=	yield strength
σ_u	=	ultimate tensile strength
a	=	flaw size (half length of through thickness flaw, depth of surface flaw, etc.)
E	=	Young's modulus

The parameter δ_r in Equation [8-2] above represents the ratio of the crack driving force to the material resistance. The maximum allowable value of this ratio for safe conditions decreases from 1 as the ratio of applied stress to yield strength increases (Figure 16). This is because an increase in applied stress leads to local crack tip plasticity and hence a crack driving force that exceeds the one calculated from linear elastic fracture mechanics. Consequently, the allowable elastic component of the driving force is reduced as applied stress increases towards yield. Thus in Figure 16, the locus represents the allowable ratio of elastic driving force to material fracture toughness at any S_r value and $(1 - \sqrt{\delta_r})$ represents the driving force due to crack tip yielding effects.

In practice there generally are self-equilibrating secondary stresses (residual, thermal) also present in addition to the primary membrane and bending stresses. Since there is no inherent safety factor in this detailed procedure, it is suggested that plasticity interaction between the primary and secondary stresses be taken into account and this is achieved by incorporating a correction factor ρ as follows:

$$\sqrt{\delta_r} = \sqrt{\frac{\delta_r}{\delta_{max}}} + \rho$$

where ρ can be estimated from Figure 17. It should be noted that the value for ρ is 0 when

$$\sigma_n > 1.05\ \sigma_y$$

or $S_r > 0.875$ assuming $\sigma_f = 1.2\sigma_y$

Secondly, the applied stress intensity due to the secondary stresses is incorporated into δ_t as follows:

$$\delta_t = \frac{(K_1^P + K_1^S)^2}{\sigma_y \cdot E}$$

where K_1^P and K_1^S are the stress intensities due to primary and secondary stresses respectively. Further,

$$K_1^P = [1/\Phi]\ [M_m \cdot P_m + M_b \cdot P_b]\ [\Pi\, a]^{1/2} \qquad [8-4]$$

and

$$K_1^S = [1/\Phi]\ [M_m \cdot Q_m + M_b \cdot Q_b]\ [\Pi a]^{1/2} \qquad [8-5]$$

where, for flat plates, M_m, M_b and ϕ are given in Reference [11]. P_m, P_b, Q_m and Q_b are respectively the primary membrane stress, the primary bending stress, the secondary membrane stress and the secondary bending stress.

As far as the magnitudes of Q_m and Q_b are concerned, there are no thermal stresses to be considered for the pressure vessel burst test. The residual stresses in the absence of any measurements would generally be assumed to be yield level. However, for a vessel in service for several years there must have been some mechanical stress relief, especially due to hydro tests carried out during its operational life. Further, as the net section stress (σ_n) increases, the magnitude of residual stresses assumed in the analysis is recommended to be reduced such that:

$$\sigma_R = (1.2 - S_r)\sigma_y \quad \text{for } S_r \geq 0.2$$

Thus, as S_r approaches 1, the contribution of residual stresses to the applied CTOD does not exceed 0.2 σ_y, even if the actual magnitude is higher.

8.4 Input Data

The implementation of the detailed analysis requires knowledge of the following four elements:

- Material Fracture Toughness
- Defect Size
- Stresses at Defect Locations

and

- Stress Intensity Factors

8.4.1 Material Fracture Toughness Data (CTOD/CTOD-R Curves)

The evaluation of material properties from the vessel was described in Section 7.0 and the data summarized in Tables 7, 8 and 9.

8.4.2 Crack Size

The crack sizes used for calculation of driving forces and burst pressure were the same as those used in the preliminary analysis given in Section 6.0 and these are shown in Figures 13a to 13g. These sizes were based on the results of the manual non-destructive inspection carried out [12], and the same assumptions were made as in the preliminary analysis with respect to the defect model. These are repeated here:

(i) where several defects were present in the same plane, the deepest and longest defect was taken as the representative case if there was no interaction between them based on PD6493 (1980). If there was interaction, the defect lengths were based on guidance in PD6493 (1980) [9].

(ii) for an array of parallel cracks, the deepest and longest defect was used. This was a conservative assumption.

(iii) for defects showing extensive curvature or complex shape, worst case cracks perpendicular to or parallel to the pressure vessel were used. This was the case for all defects apart from that defined as defect 1 at the manway location MW1.

8.4.3 Stress Calculations

The far field membrane stresses, perpendicular to the defect, were calculated using the following equations:

$$P_m = \frac{P.D}{4.e} \quad \text{for axial stress, (circumferential flaws)} \qquad [8\text{-}6a]$$

$$= \frac{P.D}{2.e} \quad \text{for hoop stress, (axial flaws)} \qquad [8\text{-}6b]$$

where P = internal pressure of vessel
D = diameter of the vessel (1830mm)
e = wall thickness of the vessel (28.6mm).

The stress concentration factor K_t was taken to be 1, except for the defect designated as Defect 1 because of the relatively large given depth of the flaws in the manway region (Figures 8 and 13g). More detailed stress analysis was carried out for this location since the burst pressure corresponding to this defect was one of the lowest in the preliminary analysis.

The flaw shown as linear in Figure 13g was in fact symmetrical with respect to the plane containing the pressure vessel longitudinal axis and the centre of the manway. It extended at shell I.D. surface for about 87° along the circumference of a circle of ≈355mm radius concentric with the manway circumference. The average depth was reported to be 5mm whereas close to one of its extremities the depth was in the range 8.9 to 11.3mm.

A 2-D finite element stress analysis was performed with the objective of establishing the magnitude of primary stresses (membrane and bending) at the location of the defect as a function of the internal pressure, assuming that no flaw was present. The shell I.D. wall region containing manway Defect 1 was directly under the reinforcing pad, and the stress analysis took into account the presence of this pad and the bi-axial nature of the loading due to the internal pressure.

This analysis is fully described in Reference [14].

8.4.4 Stress Intensity Factor

The stress intensity factor due to the primary and secondary stresses are given by Equations 8-4 and 8-5 presented earlier in Section 8.3.

An additional correction factor, M_t, generally needs to be applied for bulging effects associated with defects in a pressure vessel. However, for internal surface defects, the value is 1 [11].

Manway defect 1 in Figure 13g was curved and therefore could have an effect on the stress intensity factor solution. In order to assess this aspect, the stress intensity factor due to a circumferential surface crack (radius =355 mm) in a 1500 mm radius circular plate with a 292 mm radius hole at the centre was modelled using the virtual displacement method [14].

The resulting solution suggested that for a surface crack of given length and depth, the curved crack had a slightly lower effective stress intensity factor. However, the flat plate solution was employed for the stress intensity factor calculations to retain a certain degree of conservatism in the analysis.

8.5 Prediction of Burst Pressure for Failures From Various Defects

The burst pressures for failures from various defects were computed using two approaches.

The first approach was based on a single valued crack initiation CTOD toughness of the material, δ_i, which is generally taken to be the CTOD value on the CTOD-R curves corresponding to a crack growth of 0.2mm. The steps involved in the assessment were as follows:

(i) calculate σ_f (lower of $1.2\sigma_y$ or $0.5\ (\sigma_y + \sigma_u)$)

(ii) calculate σ_n as a function of the primary stresses (Equation 8-3). Since bending stresses are zero or negligible, this equation reduces to:

$$\sigma_n = \frac{P_m}{1-\alpha}$$

(iii) calculate S_r as a function of primary stress,

$$S_r = \frac{\sigma_n}{\sigma_f} = \frac{P_m}{\sigma_f\ (1-\alpha)} \qquad [8\text{-}7]$$

(iv) calculate $\sqrt{\delta_r}$,

$$\sqrt{\delta_r} = \sqrt{\frac{\delta_I}{\delta_{mat}}} + \rho = \frac{(K_I^P + K_I^S)}{\sqrt{\sigma_y \cdot E \cdot \delta_i}} + \rho$$

$$= \frac{1}{\phi} \cdot \frac{M_m\ (P_m + Q_m)\ (\Pi\, a)^{1/2}}{\sqrt{\sigma_y \cdot E \cdot \delta_i}} + \rho$$

In the absence of residual stress, the above equation is reduced to:

$$\sqrt{\delta_r} = \frac{1}{\phi} \cdot M_m \cdot \sqrt{\frac{\Pi\, a}{\sigma_y \cdot E \cdot \delta_i}} \cdot P_m \qquad [8\text{-}8]$$

Equations 8-7 and 8-8 show that in the absence of residual stresses, S_r and $\sqrt{\delta_r}$ are proportional to P_m - the membrane stress, and the locus of S_r, $\sqrt{\delta_r}$ with increasing values of P_m is a straight line. This straight line can be plotted on the Fracture Assessment Diagram, and the intersection of the straight line with the FAD represents the value of S_r at failure (see schematic Figure 16 for example).

The membrane stress and therefore the internal pressure at failure can be calculated from the S_r value.

If there were residual stresses present, then $\sqrt{\delta_r}$ would not vary linearly with P_m, and calculations at various values of P_m need to be individually performed and plotted.

The defects shown in Figures 13a(i), 13b(ii) and 13g were either the longest or had a relatively low calculated burst pressure based on the preliminary analysis in Section 6.0 and were initially chosen to examine:

(i) the effect of residual stresses, whose magnitude was assumed to be 0.25 σ_y,

(ii) the effect of crack tip location for defects in Figure 13b(ii) and 13g (base material vs. weld metal, the latter having the lowest CTOD toughness) and,

(iii) the effect of defect size, since for manway defect 1 in Figure 13g it was not readily apparent if defect depth was 8.89 or 11.43 mm.

A representative FAD for defect 1 at the manway is given in Figure 18 and the failure pressures calculated for all defects, along with the assumptions made are summarized in Table 10.

The second approach was based on the CTOD-R curve and the instability analysis [14]. The driving force curves for various membrane stress levels were plotted and the one which is just tangential to the CTOD-R curve sought. The corresponding stress level represented the failure stress from which the failure pressure can be calculated. Further, the crack growth (Δa) value at the point of tangency corresponds to the stable crack growth that can be anticipated before unstable fracture ensues. Such analysis was carried out for defects in Figures 13a and 13b(ii) only, with and without the presence of 0.25 yield strength level residual stresses, and for the defect 13b(ii) only, with the crack tip being in base material or the weld metal.

A representative plot for C3 axial defect modelled in Figure 13b(ii) is shown in Figure 19. The calculated failure pressures are shown in Table 11 and these are about the same as those calculated from single valued CTOD toughness in Table 10.

8.6 Observations and Predictions

Generally, the ranking of the defects in terms of the corresponding failure pressures was the same as that obtained after the preliminary analysis. This was to be expected since the main difference between the two approaches had been to take into account the much better fracture resistance of the material than was assumed in the preliminary analysis. The failure was now predicted to occur at higher stresses (i.e. higher S_R ratios) and the predominant failure mode was by collapse.

The effect of residual stresses on the failure stress was minimal which is also to be expected due to the relatively high fracture toughness of the material and due to the net section stress at failure exceeding the yield strength value.

It should also be noted that in the Level 2 PD6493 approach, the membrane stress cannot exceed the flow stress (defined as 1.2 σ_y) and this implies that for this pressure vessel, the burst pressure cannot exceed ≈11.3 MPa. However, the material has a high work hardening capacity, typical of A516 Gr 70 steels and this would have a considerable influence on the actual collapse properties of the vessel. The ultimate collapse of the vessel, assuming high resistance to fracture, could be controlled by the ultimate strength of the vessel (579 MPa) and this would correspond to vessel collapse at a pressure exceeding 17 MPa.

While the calculated failure pressures above suggest that either defect 1 in Figure 13g or the defect modelled in 13b(ii) should be the failure site of the burst test, it should be noted that within the accuracy of the predictions, any one of these defects could give rise to the failure.

For the most likely situation of crack tips in base material and negligible residual stresses, the failure pressures range from 9.5 to 11.1 MPa for the five most likely failure sites as summarized below.

Defect Identity	Reference in Figures	Failure Pressure - Predicted MPa		
		Preliminary Analysis		Detailed Analysis
		Unstable Fracture	Plastic Collapse	
Weld C3, Defect #19	Figs. 9 & 13b(ii)	5.10	8.6	9.5
Manway MW1, Defect 1	Figs. 8 & 13g(i)	8.5	16.8	9.5
Weld C1, Axial Defect	Fig. 13c	7.8	9.5	10.7
Weld V2, Axial Defect	Fig. 13e	—	9.9	11.0
Splitter Plate Axial Defect S2	Figs. 10 & 13f	—	9.8	11.1

9.0 BURST TEST

The vessel was delivered to the test facility in Alberta and mounted in the horizontal position for hydrostatic burst test after the preparation work described earlier in Section 4 and completion of the detailed fracture mechanics evaluation.

A period of 48 hours was required before the burst test in order to hook up the strain gauges and the acoustic sensors for the acoustic emission monitoring during pressurization. For pressurization, 13 mm diameter hoses rated at 27600 kPa, were also installed. Finally, those areas predicted to fail (see table in Section 8.6) were clearly identified on the outside of the vessel so that they could be monitored visually from a distance during the test.

The data acquisition and monitoring units for both strain gauging and acoustic emission were located approximately 150 meters from the vessel. Two Haskel GW 35 pumps, each rated at 30000 kPa max. fluid pressure, were connected to the pumping line. One of the pumps was isolated and was to be used only if required.

The vessel was filled with water to a pressure of 1400 kPa and left overnight to check for any leaks both in the vessel and in the pressure lines. No leaks occurred and the system pressure held overnight.

The pressure sequence to be used for the test was a ramping approach with hold points and pressure drops. This ramping sequence was requested by the contractor responsible for acoustic emission monitoring and was proposed in order to allow for the capture of all significant acoustic information. The sequence is shown in Figure 20.

Pumping began at 0830 hours at a vessel metal temperature of 18°C. The predicted failure pressure range of 9500 to 11,100 kPa was exceeded without incident. A decision was made at this point to pressurize to failure and the second pump was brought on line. Failure finally occurred in a dramatic fashion approximately six hours after initial start-up and at a pressure of 16400 kPa which was 570% of the operating pressure. The release of energy was such that the vessel rotated off its supports and a wave of water cascaded approximately 75 meters.

The burst test pressure chart is reproduced as Figure 21 and a photograph of the burst vessel taken shortly after the event is shown in Figure 22.

9.1 Preliminary Examination of the Burst Vessel

On-site examination of the burst vessel showed that failure initiated at the toe of the fillet weld at the splitter plate behind nozzle N1. This had been one of the areas predicted to fail at a pressure of 11,100 kPa. The fracture was approximately 7.0 meters in length, with one end finally arresting in the weld attaching the nozzle of the top head as shown in Figure 23 and the other in the base material adjacent to weld V2 on the bottom can section midway between the central weld C2 and bottom head weld C3. The fracture surfaces showed chevron marking indicating propagation in a brittle manner.

The fracture surfaces were protected from environmental damage and removed for metallurgical analysis within 24 hours of the completion of the burst test.

Also, areas of the vessel containing the other flaws of interest were identified and removed for assessment of actual flaw sizes, and for comparison with sizes given by non-destructive inspection. This information is reported in Section 10 of this report. Using the information so obtained, the pre-burst test fracture mechanics analysis was reviewed and is reported in Section 11.0.

9.2 Strain Gauge Monitoring During the Burst Test

9.2.1 Background

The purpose of strain gauge monitoring during the burst test was to have the ability to calculate the stress if the vessel failed before general yielding occurred. Twenty general purpose 45° single plane rosette strain gauges were mounted at selected areas on the outside of the test vessel. A number of strain gauge rosettes were placed near defect locations where failure had been predicted by fracture mechanics calculations. Figure 24 illustrates the locations of the strain gauge rosettes.

Monitoring was performed by measuring strain from three channels per rosette. The rosettes were aligned to measure strain along the longitudinal axis, 45° from the longitudinal axis and in the circumferential direction of the vessel.

9.2.2 Evaluation

The first evidence of local yielding was observed at the toe of the manway repad fillet weld (MW1) at approximately 7000 kPa. General yielding of the vessel in the circumferential (hoop) direction was observed in the shell plate at pressures between 10,200 and 10,800 kPa. Typically, circumferential and longitudinal welds began to yield in the hoop direction between 11200 kPa and 11500 kPa. Most strain gauges continued to provide data from three to four percent strain at which point the adhesive attaching the gauges to the vessel began to disbond. Figure 25 shows a typical plot of pressure versus circumferential strain in the upper shell.

Compressive strain was observed from a number of strain gauges placed on circumferential and longitudinal welds. In most cases, the compressive strain was observed in the longitudinal stress direction near the general yielding pressure and beyond.

9.2.3 Observations

(a) The strain gauges only gave information about yielding during the burst test. The yielding in the circumferential direction was accurately recorded by the strain gauges.

(b) Compressive strain at circumferential and longitudinal welds was caused by the shell base metal yielding (bulging) adjacent to the stronger welds. Another factor that may have caused compressive strain in some locations were restraining forces that developed from weld internals, nozzles and the vessel skirt.

(c) Stresses cannot be easily calculated from strain data after yielding has occurred.

9.3 Acoustic Emission Monitoring During the Burst Test

9.3.1 Background

Normally, acoustic emission (AE) would be utilized as a screening device for in-service pressure vessels to identify areas that may contain conditions that affect the integrity of the vessel. Once areas of significant activity within the vessel have been identified, follow-up inspection by various non-destructive evaluation (NDE) techniques would be required to locate and size any defects that could be detrimental to vessel integrity. Usually, the AE test would run at 110% of the operating pressure while the vessel was in operation or it would be shut down and a hydrotest performed to 1.5 times that of the design pressure.

For the purposes of this program defects in the test vessel were located by wet fluorescent magnetic particle testing and sized by various ultrasonic techniques as previously described. The planned objective of the AE program was to determine if acoustic emission could identify growing defects and predict potential failure initiation sites prior to failure. The AE evaluation would concentrate on AE activity gathered from initial pressurization to a typical hydrotest of 1.5 times the test vessel design pressure with the objective of early identification of potential failure sites.

The reported operating pressure of the vessel was 2900 kPa and according to the records, this vessel was hydrotested to 5500 kPa while in service, which was 190% of the operating pressure and 1.5 times the design pressure. As reported in Section 3.0, the vessel had been out of service for approximately 18 months and during preparation a patch had been removed and replaced from the vessel to obtain material mechanical properties. All but 2 of the nozzles were sealed by welded plugs and none of these modifications were post weld heat treated prior to hydro test.

Prior to pressurization, an attenuation test was performed to determine the number of sensors required and proper spacing of the sensors. This test showed low attenuation indicating that any AE noise travelled easily throughout the vessel. A total of 19 AE sensors were placed on the vessel and a number of these were placed near defect locations where failure had been predicted by ECA calculations. A planned view of the vessel identifying the location of the AE sensors is found in Figure 26.

The initial pressurization schedule for the burst test was designed around an AE evaluation program called MONPAC. This was an acoustic emission based system for evaluating the structural integrity of metal vessels. This technique had been developed from a database of laboratory, prototype studies and field test experience. Under normal circumstances minimal AE data filtering is performed during the MONPAC evaluation.

Initially the vessel was pressurized to 1400 kPa before AE data was gathered. The MONPAC portion of the test included hold periods at 90%, 100%, 105%, and 110% of the operating pressure as illustrated in Figure 20. The vessel was then unloaded to 90% of the operating pressure before proceeding to hold periods at 150% and 190% (hydrotest portion of the test) of the operating pressure. Again, the vessel was unloaded; this time to 110% of the operating pressure before proceeding to hold periods at 230%, 270%, 300%, 345% (10000 kPa) and 380% (11000 kPa) of the operating pressure. AE activity increased dramatically between 10000 and 11000 kPa as general yielding began.

9.3.2 Evaluation

The initial evaluation performed followed the MONPAC procedure of examining strictly the unfiltered AE data from each of the 19 sensors. The MONPAC and hydrotest portion of the test revealed a high (C or D) intensity rating from each sensor suggesting that follow-up examination by methods other than AE would have been required in most areas of the vessel, if this had been an in-service AE test. A C-D intensity rating suggested a significant amount of AE activity.

The post-burst test analysis determined that the majority of defects did not extend, but became blunted. They also contained sulphide deposits which were found in pre-existing cracks. As a result of these observations, further evaluation was performed to re-assess the AE data during the MONPAC portion and the hydrotest portion of the test. The additional analysis included filtering of the AE data, source location plots, examination for the presence of the Kaiser Effect, i.e. the absence of significant data prior to the previous stress levels and a comparison of AE monitoring of other vessels with known flaws in which a burst test was performed.

Filtering was performed by removing long time waterborne AE signals and long duration echoing of signals caused by the very low attenuation of the vessel. The majority of sensors indicated reduced intensity ratings with the removal of these long duration signals. After filtering, only two locations had C ratings; one near the demister ring and the other at the top head. Sensor #19 at the splitter plate location gave very little emission. Table 12 compares the intensity ratings of unfiltered and filtered data.

Source location plots shown in Figure 27, utilizing AE data from Sensors 1 through 9 only, revealed significant AE signals from the replacement patch location. Also, some nozzle areas, especially nozzle N1A located in the upper shell section, showed significant amounts of activity. Two other areas that revealed significant AE activity were in the vicinity of the N1 splitter plate and in the area of circumferential weld C3 between Sensors #7 and #9. Defects were identified in both these areas before the burst test. Bar graphs found in Figures 28(a) to (c) comparing the number of AE events versus sensor location clearly show the areas of most activity.

The Kaiser Effect was defined as the absence of AE until previously applied stress levels are exceeded. Vessels with severe defects emitting significant AE will produce signals below the previous maximum, this being known as the Felicity effect. The Felicity effect was seen during initial pressurization below the original operating pressure. However, once the pressure was dropped and then re-pressurized through the previous maximum at 110% and 190% of the operating pressure, the Felicity effect did not occur.

Comparison of similar tests indicates that a vessel that has been out of service for a long period of time can exhibit unusual short bursts of AE activity as the pressure passes through previous maximum levels. This phenomenon was seen during this test.

9.3.3 *Observations*

(a) Acoustic Emission monitoring during the MONPAC and hydrotest portion of the burst test did not predict the failure initiation site at the splitter plate. The vessel failed well beyond yield and any crack extension at the defect sites likely occurred beyond 190% of the operating pressure (1.5 times the design pressure).

(b) The analysis of unfiltered AE data normally incorporated by the MONPAC procedure for an in-service pressure vessel was not adequate for the evaluation of the test vessel. Additional analysis, including filtering and source location, were required because of a number of factors that included low attenuation, the vessel being out of service for an extended period of time and new, non-stress relieved, welds.

(c) The Kaiser Effect was observed in this test, meaning no emission occurred before previous maximum stress levels both after the MONPAC and hydrotest portion of the test. If extensive crack growth was present, AE activity should occur before the previous maximum stress.

(d) The low attenuation in this test vessel, coupled with the high number of sensors utilized, distorted the unfiltered AE data normally used in the initial evaluation. Once the erroneous data was filtered, the amount of AE activity of concern dropped dramatically.

(e) The cause of AE activity in the areas of cracks at circumferential weld C3 and in the vicinity of the N1 splitter plate could not be determined with any degree of confidence. It was thought that this AE activity, which occurred below the hydrotest pressure, may have been caused by deposits producing acoustic emission within cracks attributed to the vessel being out of service for an extended period of time. Another possibility was that plastic deformation caused by crack blunting resulted in AE activity.

(f) Source location plots determined that the patch welds and nozzle closing welds caused a large amount of AE activity. Experience had indicated that non-stress relieved welds generate significant irrelevant AE activity.

10.0 POST-BURST TEST METALLURGICAL ANALYSIS

10.1 Introduction

This particular task had the primary objective of measuring the sizes of the principal flaws by fractographic methods and to directly compare their actual dimensions with the respective values as assessed by the three ultrasonic inspection techniques employed in the program. By means of a metallographic approach, it was also possible to describe the nature of the flaws in relation to their initiation and growth.

10.2 Flaw Sizes

The fractographic and metallographic investigation enabled the maximum actual sizes of the flaws to be measured. These are compared with those obtained by ultrasonic inspection in Tables 13 and 14.

It can be seen from Table 13 that the TOFD UT technique was reasonably accurate in providing estimations of actual crack depths. However, it should be noted that TOFD in this case tended to undersize the defects. Particular reference is made to the NDE of the demister ring flaws at fillet welds F1 and F2. Further work may suggest that the magnitude of the undersizing error may diminish with increasing real flaw depth.

In contrast to TOFD, the other UT techniques used in the program overestimated the defect depths, most notably the manual pulse echo method. The digitized pulse echo technique did produce an anomaly in the corrected data such that an existing defect depth of 2.36 mm was reclassified as undetected (i.e. no depth, whereas initially there was an overestimation of more than 100% of the same defect.

10.3 Metallurgical Examination of the Regions Containing Flaws

10.3.1 Splitter Plate End Flaw (Figure 13f)

As mentioned in the previous section, the pressure vessel failure initiated at the toe of the fillet weld 'S2' at the splitter plate behind nozzle N1 (Figure 29). There was a flaw present at the toe of fillet weld S1 as well; however, it was evident that fracture initiated at weld S2 where the crack had grown to a depth of ≈ 12 mm before failure.

At weld S2, the pre-existing crack had a depth of 4.76 mm max. and was at the weld toe, ≈ 12 mm from the splitter plate end. During the hydrostatic burst test, a pop-in had initiated from the flaw [15] which was followed by stable crack growth and then the final fast fracture (Figure 30). Metallography revealed the presence of a single non-post weld heat treated weld pass at the fracture surface and established the starting point of the pop-in to be at the approximate junction between the intercritical HAZ and the base material as shown in Figure 31, which also shows the hardness of the various regions. A macro-etch of the fracture site at S2 confirmed the speculation that it had been subject to a repair weld at some earlier point in the history of the vessel (Figure 32).

10.3.2 Weld C3 Flaws (Figures 13b(ii) and (iv))

Both the axial and the circumferential flaws were associated with repair welds on the inside surface of the bottom head (Figures 33 and 34). The repair welds were assumed to have been done in-situ and after the vessel had seen some service. In both cases, the repairs were done on top of or in association with ghost outlines of some prior weld beads on the inside surface of the head. These latter welds were evidently some cosmetic repairs to the material surface associated with head forming as they had a normalized structure and no heat affected zone.

The axial flaw was associated with a nearly circular patch of shielded metal arc welding, ~ 55 mm diameter (Figure 35). On sectioning, the depth of the repair weld was found to be less than 6 mm. The cracks were believed to be hydrogen or SSC related and were present at the hoop loaded portions of the periphery. The crack had initiated in the HAZ and had traversed perpendicular to the surface and then arrested in the base material. Figure 36 shows a shear crack that was growing out of the top of the original crack during the hydrotest.

The Vickers microhardness of the coarse-grained HAZ was measured at 458 (100g load) and 418 (300g load) which are quite high considering that according to the mill test report, the steel for the head had 0.19% C, 1.15% Mn and no other alloying elements.

The circumferential crack is shown in Figure 37 and is typical of HAZ hydrogen embrittlement cracking of a discontinuous nature, partially transgranular and partially intergranular, in a microstructure of predominantly martensitic appearance.

10.3.3 Demister Ring Flaw (Figure 13a)

No metallographic examination was carried out for the demister ring fillet welds. The main focus was to establish the flaw depth and one of the typical exposed surfaces containing the flaw is shown in Figure 38. It was evident that no crack growth had occurred during the burst test.

10.3.4 Manway Reinforcing Pad Flaw (Figure 13g)

The fractographic examination indicated that this flaw did not exceed 2 mm in depth. In contrast, the manual ultrasonic inspection sized the depth to be up to 11 mm. The large discrepancy was believed to be due to the awkward geometry of the weld since the flaw was present at the root of the fillet weld, a location where the corner also made a perfect reflector (Figure 39). The flaw was judged to be typical of a lack of fusion/cold lap region in the root pass.

10.4 Summary

The metallographic examination carried out indicated that most of the significant flaws were associated with in-service weld repairs, which are not uncommon in moderately thick walled pressure vessels having fillet welded internal attachments. These repairs occasionally had high HAZ hardnesses indicating less than optimum welding procedures, and no consideration of techniques alternative to post weld heat treatment to reduce HAZ hardness (e.g., the temper bead technique). The flaws however after initiating in the HAZ usually had an orientation perpendicular to the surface, and had arrested once they reached unaffected base metal.

Most flaws examined showed no evidence of crack growth during the burst test, i.e., only crack blunting was observed.

The fracture initiation site was unique in that it displayed a significantly large pop-in feature within the region of stable tearing, prior to the final failure.

The TOFD UT technique provided estimates of crack depth that were closest to but slightly smaller than the actual depths measured during the post-burst test examination. The other UT techniques used in this project were conservative, i.e. they overestimated the flaw size.

11.0 DISCUSSION - POST-BURST TEST FRACTURE MECHANICS ANALYSIS

11.1 Introduction

Following the post-burst test metallurgical failure analysis, which established the actual defect sizes, the fracture mechanics analyses performed prior to the burst test were reviewed.

As shown in Sections 6.0 and 8.0 of this report, predictions were made for failure pressures based on flaw sizes established by NDE. These predictions, for zero residual stress assumption, are reproduced in Table 15 for both the preliminary and detailed analyses.

The defects, in the order of their increasing failure pressures as predicted by the detailed analysis, were:

Defect	Figure	
Manway Defect	8 and 13g(i)	
Weld C3 Axial Defect	9 and 13b(ii)	
Weld C1 Axial Defect	13c	
Weld V2 Axial Defect	13e	] roughly
Splitter Plate Axial Defect	10 and 12f	] equal

The metallurgical failure analysis indicated the flaw tips to be always located in the base metal. Ignoring further the residual stresses (in light of the high actual burst pressure) the predicted failure pressures for the above listed defects were in the range 9.5 to 11.1 MPa (Table 10).

In contrast, the results of the burst test were as follows:

(a) the failure occurred at 16.4 MPa internal pressure;

(b) the fracture initiated from the axial crack at the splitter plate end after some stable tearing;

(c) the fracture propagated in a brittle manner as indicated by chevron markings on most of the fracture surfaces.

The objectives for this post burst test analysis were therefore to address the following questions:

(i) Why was the burst pressure so much higher than the predicted range?

(ii) Why did the failure initiate from a crack which had approximately the fourth lowest predicted failure pressure?

(iii) Why did the fracture propagate in a brittle manner?

11.2 Analysis

11.2.1 Burst Pressure

Both previous analyses made a conservative assumption that material fails by plastic collapse when the net section stress exceeds the flow stress, which is defined as the lower of (1.2 x yield strength) or the average of yield and ultimate tensile strengths. For the SA516 Gr 70 steel used in the fabrication of the pressure vessel, this approach limits maximum net section stress in the hoop direction to 367 MPa, which would correspond to a maximum internal pressure of ≈ 11.3 MPa in the absence of flaws or stress concentrations.

For the SA516 Gr 70 steel in question, the ultimate tensile strength was 579 MPa in the hoop direction and, in the absence of flaws, this corresponds to an internal pressure of ≈ 17.8 MPa. Since the CTOD exhibited by materials in the tension mode can be considerably higher than in the bending mode of the CTOD specimen, and because of the high work hardening capacity of the SA516 Gr 70 steel, the net section stress can considerably exceed the flow stress calculated in the detailed analysis.

Assuming that the size of the axial crack at the splitter plate end was the same as used in the earlier analysis and assuming that the flow stress was 579 MPa (the ultimate tensile strength) instead of 367 MPa (1.2 X yield strength), then for the zero residual stress assumption,

$$\alpha = \frac{a}{e}\left[1 + \frac{e}{c}\right]^{-1} = 0.04$$

$$\sigma_n = \frac{P_m}{1-\alpha} = \frac{P_m}{0.96}$$

$$S_r = \frac{\sigma_n}{\sigma_f} = \frac{P_m}{556} \qquad (11\text{-}1)$$

where

α	=	parameter related to defect size and wall thickness
a	=	crack depth;
e	=	wall thickness
c	=	half length of a surface defect
P_m	=	membrane stress;
σ_n	=	net section stress;
σ_f	=	flow stress

and following the detailed analysis,

$$\sqrt{\delta_i} = \frac{1}{\phi} \cdot \frac{M_m \cdot P_m \sqrt{\pi a}}{\sqrt{\sigma_y E \delta_i}}$$

$$= 0.79 \times 10^{-3} P_m \qquad (11\text{-}2)$$

where ϕ and M_m are geometry related, σ_y is the yield strength, E the elastic modulus and δ_i the CTOD value at crack initiation.

The line defined by Equations (11-1) and (11-2) intersects the Level 2 Failure Assessment Diagram (FAD) at $S_r > 0.99 \approx 1.0$ [14]. The corresponding membrane stress (nominal hoop stress), would therefore be ≈ 556 MPa, which corresponds to an internal pressure of ≈ 17.1 MPa. The actual failure pressure was 16.4 MPa, slightly lower than the calculated value. This difference was likely due to the bending stresses present, as discussed in Section 11.2.3.

The actual failure pressure of 16.4 MPa corresponds to a membrane stress of ≈ 533 MPa, and if at failure S_r = 1.0 and σ_f = 579 MPa, then $\alpha \approx 0.08$. Assuming that the surface crack length at the splitter plate end was 28.5 mm and that during stable ductile tearing this dimension did not change, then the crack depth at the time of failure can be computed to be ≈ 7.0 mm. Thus, if the defect grew to a depth of 7 mm or more before failure, it would suggest that net section stress had reached the ultimate tensile strength.

The photomicrograph of the fracture surface was shown in Figure 30 and shows that the crack had grown to a total depth of at least 8.73 mm and more likely to 12.7 mm before fast fracture ensued.

The above is a simplistic approach to illustrate the changes in burst pressure with the assumed flow stress. The biaxial stress state present at the splitter plate end would be expected to influence these numbers.

11.2.2 Propagation in Brittle Mode

By reference to Figure 30, there was initially a small pop-in, i.e. a crack jump ≈ 3.97 mm, which initiated at the intercritical HAZ/base material region [15]. This pop-in was arrested in the base metal, either due to its good inherent crack arrest toughness (>50J CVN toughness at room temperature) and/or the crack shape and the limited stored energy in the early stages of the hydro test.

This event was followed by stable tearing in the base metal to a depth of about 12.7 mm before the final fast crack propagation, which was in the cleavage mode. This type of change in crack propagation mode had been observed before [16]. Thus, Milne reports that in a vessel containing fatigue sharpened defects in its crotch corners and pressurized at 24°C, a ductile crack initiated and with increasing pressure, grew by 12.7 mm. At this stage, the cracking mode changed to cleavage and the vessel failed catastrophically.

The reasons for the triggering of cleavage fracture were believed to be two fold. First, laboratory data on fracture resistance of the material (CTOD-R curve) was obtained under a strain controlled situation whereas the crack propagation behaviour during the burst test was load controlled, i.e., due to the high stored energy at the peak internal pressure, any instability at the crack tip meant that local strain rate was much higher than that present in the laboratory CTOD-R curve determination. This explanation is consistent with the observation that the base material CVN specimens, when tested at room temperature, showed more than 40% crystallinity.

Secondly, the high internal pressure at failure and correspondingly high hoop stress imply that the steel would have work hardened considerably and therefore may have suffered some toughness degradation before the crack propagated through it.

11.2.3 Failure Initiation Site

As stated, predictions prior to the burst test indicated that there were several other likely failure initiation sites than the one actually observed in the test.

The reasons for this apparent discrepancy could be related to the different material toughness at the location of the various cracks which is, however, unlikely because virtually all cracks are located at weld toes and could be assumed to encounter the same microstructural regions. The post-burst test metallurgical examination is consistent with this view. The more likely explanation is due to a combination of defect sizes and stress state as described below.

(1) The crack sizes used previously were proportionately larger for the "preferred" sites than for the splitter plate end.

As the actual defect sizes were available from post-burst test fractography, the burst pressures using the correct defect sizes were recalculated. The objective of this exercise was to ascertain if both the preliminary and detailed analyses were able to identify the most severe defect. The results of the repeated analyses are compared with the previous results in Table 16. The data included is for the case of zero residual stresses and base material CTOD properties.

Based on actual defect sizes, it was clear that the crack at the splitter plate end was the most severe. In the revised preliminary analysis, all the defects had a relatively small driving force. However, the internal pressure required for plastic collapse was the lowest for the crack at the splitter plate end.

Similarly, the detailed analysis indicated that all the defects would fail by plastic collapse ($S_r = 1$ in the Failure Analysis Diagram) except for the one at the splitter plate end. Here the failure pressure is marginally lower, the burst pressure prediction being 10.8 MPa, corresponding to $S_r = 0.96$. The pressure for plastic collapse, in comparison, is 11.3 MPa. It should be noted that splitter plate end flaw is the only one where the revised (post-burst test) calculation leads to a lower failure pressure.

(2) The membrane and bending stresses used in calculations may have been overestimated for the three "more likely" cracks and underestimated for the splitter plate end location. The former situation is believed to be true for the manway defect where in spite of the complex geometry, 2-D analysis was carried out and bending stresses were assumed to be zero, even though conceivably, compressive bending stresses were present [14].

Conversely, the crack at the splitter plate end was unique in that of all the defects investigated, it was at the end of an attachment weld. At such a location, the following could lead to higher local stresses:

(i) geometric stress concentration;

(ii) higher residual stresses due to the fillet weld around the splitter plate;

(iii) presence of bending stresses due to the additional stiffness of the splitter plate and the associated higher yield strength fillet weld metal which would resist shell expansion during pressurization.

The influence of the first two items should be negligible because the initial defect depth was greater than 15% of the wall thickness. The presence of bending stresses could, however, be a contributing factor causing this location to be the failure site. The importance of these bending stresses can be gauged from the tearing in the splitter plate itself as shown in the photograph in Figure 40 taken after completion of the burst test.

An attempt was made to estimate the magnitude of these bending stresses, using finite element modelling [17]. The finite element mesh for the 2-D model is shown in Figure 41 and includes the fillet weld around the splitter plate. The two dimensional nature of the model meant that the thickness of the splitter plate was modelled to be the same as the length of the vessel. Two cases were considered: a standard case where the elastic modulus was the same everywhere, and a second case where the elastic modulus of the splitter plate and a portion of the shell where it was attached was reduced by a factor of eight. This second case meant that the hoop stress in this region of the shell was the same as that without the splitter plate.

For simplicity, an elastic analysis only was performed and Figures 42 shows the stress distribution for an internal pressure of 1.5 MPa (nominal hoop stress = 48 MPa). In both cases considered, the shell O.D. was in small compression (hoop stress) whereas I.D. surfaces were at = 320 MPa. These numbers indicate a high stress gradient at the I.D. surface and the presence of very high bending stresses. Assuming a linear change in stress from the I.D. to the O.D., the bending stress would be = 170 MPa. In comparison, the nominal hoop stress, in the absence of the splitter plate, at 1.5 MPa internal pressure, is = 48 MPa (Figure 43).

11.3 Observations

(a) The fracture mechanics analyses employed in the program (PD6493 and proposed revisions thereto) made conservative predictions for the failure pressure. This was true when using flaw sizes determined by NDE or by post-burst test fractography in conjunction with lower bound estimate and actual CTOD toughness of the materials, respectively. The critical analysis employed in the detailed approach does not have any built-in safety factor, and it estimated the burst pressure to be 10.8 MPa based on the actual crack size and CTOD toughness. The failure pressure determined from the burst test was 16.4 MPa. This represents a safety factor of slightly greater than 1.5 on the calculated failure pressure.

(b) The origin of this unintended 'safety factor' lies primarily in the calculation of the flow stress (lower of [1.2 X yield strength] and [average of yield and ultimate strengths]) at which plastic collapse is deemed to occur, and which therefore cannot be exceeded at the net section, i.e. at the ligament ahead of the surface crack.

Thus, based on the yield and ultimate strengths of the pressure vessel steel, the flow stress, and therefore the plastic collapse stress, was calculated to be 367 MPa. The actual failure pressure of 16.4 MPa corresponds to a nominal hoop stress of 533 MPa which is substantially higher than the assumed plastic collapse stress (367 MPa), and almost 92% of the ultimate tensile strength of the steel.

The actual plastic collapse stress, however, can be lower than the uniaxial tensile strength on account of biaxial stress state, local bending stresses, etc.

(c) The cleavage crack propagation mode which occurred after some stable tearing was believed to be due to the high stored energy in the system when the peak internal pressure was reached. This approximates a load controlled situation leading to a higher local strain rate in comparison with the strain rate used for laboratory fracture toughness determination.

(d) The fracture initiated at the splitter plate end crack instead of three other sites with similar predicted failure pressures due to the following reasons:

(i) The majority of defects were smaller than indicated by the MPI and manual UT inspection. The crack at the splitter plate end, however, was found to be longer and only slightly less deep than assessed by NDE inspection prior to the burst test.

(ii) bending stresses were not initially considered at the splitter plate end when in fact these were substantial due to the increased local stiffness and the resistance offered to the pressure vessel wall expansion. The magnitude of these bending stresses was demonstrated by the tear in the centre of the splitter plate itself.

12.0 GENERAL DISCUSSION

As mentioned before, the main objective of the program had been to assess the validity and conservatism of the engineering critical assessment (ECA) approach used in the context of pressure vessels containing sour service damage, and which is based on the British Published Document PD6493:1980, and proposed amendments. (These have now been published as PD6493:1991.) This approach focused on the acceptability or otherwise of a flaw at a given point in time and time dependent flaw growth was outside its scope.

The implementation of any ECA approach requires three input parameters, viz.

(i) flaw size
(ii) stresses (applied and residual)
(iii) fracture toughness of the material in which the flaw resides

The applicability of the ECA approach is thus best judged when all the input parameters are accurately established. In reality, that is rarely the case, the greatest uncertainties lying in establishing flaw size, residual stresses and the fracture toughness of the material. There are two types of uncertainties relative to the last input parameter. The first type is due to the normal scatter observed when fracture toughness is measured. The second type relates to situations where pre-fabrication qualifications did not include fracture toughness tests or when such records are not available.

In the present program the focus has been to assess the effectiveness of various NDE techniques in accurately sizing the flaws, and to evaluate the application of the ECA procedure, using both the 'lower bound' fracture toughness, and the actual fracture toughness as determined from a patch removed from the vessel. These aspects are further discussed below.

12.1 Non-Destructive Inspection for Sizing Flaws

The common non-destructive evaluation techniques used for the detection and sizing of planar flaws present in vessels in service are magnetic particle, and manual ultrasonic inspections [18]. These two techniques were used in the program.

While much is known about the use of manual ultrasonic techniques, it was also considered necessary to evaluate mechanized techniques in order to study their relative application and accuracy.

The initial detection of defects was performed using wet fluorescent magnetic particle inspection on the inside surface of welded joints in the vessel and black magnetic ink onto a white contrasting background for inspection of welds on the outer surface. The vessel had been sandblasted before to improve the surface for NDE. By reference to Section 5.0, it can be seen that a majority of defects were found on the inside surface, most of these being associated with welds. Several of these defects were in fact cracks associated with repairs welds that most likely had been made during the service life of the vessel and which were referred to earlier in Section 10.0 of this report.

As expected, wet fluorescent magnetic particle confirmed its usefulness in locating surface breaking cracks where length could be measured. However, the technique was not capable of providing any information on the extent of crack depths and further inspection by ultrasonics to map through thickness depth was necessary.

Manual ultrasonic inspection using pulse echo techniques was able to provide estimates of crack depths for all the geometries on the vessel. However, as can be seen from the data presented in Table 13, crack sizing by this method gave depths which were generally much deeper than those actually found after metallurgical examination of the cracked areas in a post failure analysis.

The ultrasonic inspection was carried out by the pulse echo technique and the sizing was performed by the 6 dB 'drop off' method as outlined in ASME Section V. The time of flight of the pulse is used to estimate the distance from the probe to the defect and subsequently the edges of the defect are delineated by tracking to a 6 dB drop in amplitude. The procedure depends on accurate calibration of the transducers, measurements taken directly from the CRT screen and on the beam spread of the transducer as illustrated in Figure 44. It has been reported that the accuracy of sizing cracks by manual pulse echo techniques is within 2 to 5 mm [19] and the data reported in this work and summarized in Table 13 supports this.

With respect to the two mechanized techniques used in this program, a distinction can clearly be seen in the results of Technique A and Technique B. These two techniques were used to detect and size the cracks at the toes of the fillet welds F1 and F2. This inspection was essentially a scan around the circumference of the vessel and represented a geometrically favourable situation for both mechanized methods.

As stated in Section 5.3, Technique A used the Time of Flight Diffraction method (TOFD) in a 'pitch and catch mode'. The basic principles of TOFD are somewhat different than the pulse echo techniques in that the incident beam interacting with a crack produces diffracted beams at the crack tip. This is illustrated diagrammatically in Figure 45. These diffracted beams are detected by a second probe from which the distance and size of the crack can be calculated. The accuracy of this measurement is further enhanced by data processing programs.

Technique B is a sophisticated "hands off" form of the pulse echo techniques, also using 'pitch and catch' transducers. As with Technique A, the accuracy of measurement is increased by data processing procedures.

From Table 13, it can be seen that the TOFD method was the most accurate in crack depth evaluation. However, it should be cautioned that the technique tended to underestimate the flaw depths which in turn will lead to over-prediction of burst pressure or fracture stress. Technique B, though not as accurate as TOFD, did provide conservative estimates that were more accurate than the manual pulse echo technique. This was a direct result of its automated form and its data processing capability.

In addition to their greater accuracy in sizing as compared with the manual methods, the mechanized techniques had the following advantages:

(a) provided a permanent record;

(b) provided real time output;

(c) data processing procedures intrinsic to these techniques are able to improve the preciseness of the measurements; and

(d) reproducibility for direct comparison during periodic inspections.

In summary then, the manual ultrasonic inspection technique - normally used in the industry to size flaws - tended to over-predict the flaw sizes in the program by 1.5 to 5 mm. The two mechanized techniques employed provided more accurate flaw sizes, though the TOFD technique underestimated the flaw size. However, the techniques are expensive and their effectiveness in the present program was demonstrated for the one relatively simple geometry chosen only.

Since the common industry practice remains to employ the manual ultrasonic technique, the flaw sizes determined by this approach were used in the ECA procedures. If it can be established from literature that the manual ultrasonic procedures always overestimate the flaw depth, then it will add to the margin of safety that is inherent in the ECA approach.

12.2 Validity and Conservatism of the ECA Procedures Employed

The preliminary assessments of failure pressure and failure mode were made using the CTOD design curve and material fracture toughness estimated from relevant data in the literature. Such an approach is relatively quick and easy to apply and is considered as a screening step because of the built-in conservatism resulting from an inherent safety factor of '2' for flaw size and from the lower bound fracture toughness values assumed. In the present program, an additional reason for using the lower bound fracture toughness values in the preliminary analysis was the possibility of toughness degradation due to the presence of residual hydrogen in the pressure vessel steel.

Based on this approach, the failure pressures for unstable fracture from various flaws were predicted to be in the range 5.1 to 8.0 MPa. The lowest estimated failure pressure (5.1 MPa) was for defect #19 which lay transverse to weld C3. In comparison, the actual failure pressure was 16.4 MPa and ignoring the different failure initiation site for the time being, this implies a safety factor of better than three.

Such a degree of conservatism may incorrectly lead to predictions of "unacceptable flaws" when in fact they may be acceptable. If there is time or other constraint against repairs, then it may be worthwhile to perform the more detailed analysis, assuming that the input parameters can be established quickly. In the present program, this involved CTOD testing of specimens with notches located in base metal, heat affected zone and weld metal, and the use of the Failure Analysis Diagram. The flaw sizes used were, however, the same as for the preliminary analysis, i.e. as determined by the manual ultrasonic technique, typical of a field situation.

Generally, the ranking of the defects in terms of their failure pressures was similar to that obtained by the preliminary analysis. This is to be expected as the fracture toughness of the material was much higher than that assumed in the preliminary analysis. The failure pressures are thus higher indicating that, compared to the preliminary analysis, the acceptable flaw size would be somewhat higher.

The predicted locations of failure (lowest failure pressures) were the manway defect #1 and the flaw #19 transverse to weld C3 though three other locations had only marginally higher predicted burst pressures. The estimates of failure pressures were in the order of 7.0 to 9.5 MPa depending upon the assumptions regarding the crack tip location (base metal or weld metal), and the residual stresses. The actual failure pressure (16.4 MPa) thus still represents a safety factor of approximately 1.5 to 2.4. with respect to the predictions of the detailed analysis.

As alluded to before, a portion of the above calculated safety factors is due to the over-estimates of flaw sizes as determined by the manual ultrasonic technique. When the analyses were repeated using the actual flaw sizes as established by post-burst test fractography, the splitter plate end flaw (F2) was confirmed as the most likely failure site while still representing a safety factor of 1.5.

The safety factor of 1.5 arrived at by the post burst test fracture mechanics analysis is predominantly due to the relatively low value of the assumed flow stress of the pressure vessel steel at which plastic collapse is deemed to occur. Most pressure vessel steels of the ASTM A516 type have high work hardening capacity and therefore there will be a certain degree of conservatism associated with the analysis. But for this assumption, the detailed analysis does not have any built in factor of safety and thus would define the critical failure pressure or critical flaw size as the case may be.

In summary, the ECA analyses performed correctly predicted the failure site when the actual flaw sizes were known. Even for the critical analysis carried out, the burst pressure was 50% more than the predicted one. The use of manual NDE based flaw depth further increases this conservatism since the technique consistently overestimated the flaw depths.

13.0 CONCLUDING SUMMARY

There are numerous moderately thick as-welded pressure vessels that are subject to hydrogen charging environments. These may belong to the petroleum production, refining, petrochemical and utility industries. Experience has shown and this program has confirmed, that in the as-welded condition, the weld heat affected zone may be sufficiently hard to be susceptible to sulphide stress cracking. However, even though these cracks can quickly encounter the tougher base material and be arrested, the current approach is to detect them, no matter how small and repair them, frequently without any subsequent post weld heat treatment. Unfortunately, the heat affected zones of such repair welds are once again subject to similar type of cracking as before and thus the cycle of inspection and repairs continues.

In contrast, the engineering critical assessment methodology has made considerable strides in the last decade, and frequently such approaches show that small cracks, especially once their tips have emerged into base material from the heat affected zone, can be safely left in. If such a conclusion can be arrived at with a high degree of confidence, then it would lead not only to considerable cost savings, but also a safer structure since poorly conceived and executed repair welds are often the cause of vessel failures.

The objective of this program was therefore to apply an ECA methodology to a vessel which had seen hydrogen related service and had been retired from duty on account of the numerous planar flaws present therein. The approach followed was to thoroughly inspect the vessel to establish the flaw sizes using a variety of techniques and then use the ECA methodology to predict the vessels failure pressure during a controlled hydrostatic burst test.

A metallographic and fractographic analysis was performed after the burst test to establish the correct flaw sizes and review the ECA predictions. As a result of this analysis, it was concluded that both the simpler preliminary and the more detailed ECA approaches used successfully provided conservative predictions regarding the failure pressure. More specifically:

A. A part of the conservatism in the predictions stemmed from the overestimation of flaw size using the manual ultrasonic inspection - the technique most often used for estimating the depth of flaws in vessels in service.

   Other NDE procedures used in the program, some for limited weld length only, also demonstrated that:

   (i) wet fluorescent magnetic particle inspection provided adequate sensitivity for finding surface breaking flaws in vessels;

(ii) the manual ultrasonic technique tended to overestimate flaw depths by about 1.5 to 5 mm;

(iii) the mechanized pulse-echo technique also overestimated the flaw depth, but to a smaller extent;

(iv) the TOFD technique was most accurate, however it usually underestimated the flaw depth;

(v) acoustic emission monitoring has been used by some to follow crack growth in service. However AE monitoring of the vessel during the burst test only indicated that imperfections were present and the high level of AE activity was not associated with crack growth.

B. A second source of conservatism can be the usually 'lower bound' material toughnesses used, especially in the preliminary analysis making it even more conservative than the detailed analysis. When the same stresses, flaw size and material properties are used the preliminary analysis still gives more conservative results because of built-in safety factor of 2 on flaw size. The detailed analysis has no such inherent safety factor.

However, it should be noted even when the actual material toughness and the actual flaw size as determined from the post-burst test fractography were used in the preliminary and detailed analyses, the actual failure pressures were 1.5 to 2.4 times the predicted values. This difference was largely caused by the high work hardening capacity of the pressure vessel steel.

C. The benefits and success of the ECA approaches used are evident from the fact that:

(i) The failure pressure was ≈ 5 times the design operating pressure even though the vessel had several flaws and had been retired from service.

(ii) The flaw at splitter plate end was correctly identified as the one most likely to cause failure initiation. The burst pressure was still 50% higher than the predicted one with the actual flaw sizes and properties used.

(iii) Several of the flaws were associated with repair welds suggesting that repair of minor cracks which ECA may demonstrate to be acceptable, may instead lead to more severe cracking.

14.0 REFERENCES

[1] Canadian Standards Association, 1986, Boiler Pressure Vessel and Pressure Piping Code; CSA Standard B51-M1986, Rexdale, Ontario, Canada.

[2] Farr, J.R., 1987, The ASME Boiler and Pressure Vessel Code: Overview in Pressure Vessel Codes and Standards. Ed. R.W. Nichols, London: Elsevier Applied Science:1-34.

[3] Farr, J.R., 1987, The ASME Boiler and Pressure Vessel Code: Section VIII - Pressure Vessels in Pressure Vessel Codes and Standards. Ed. R.W. Nichols, London:Elsevier Applied Science: 35-58.

[4] Chockie, L.J., 1987, The ASME Boiler and Pressure Vessel Code: Section III - Rules for Construction of Nuclear Power Plant Components in Pressure Vessel Codes and Standards. Ed. R.W. Nichols, London:Elsevier Applied Science: 59-78.

[5] Chockie, L.J., 1987, The ASME Boiler and Pressure Vessel Code: Section XI - Rules for Inservice Inspection of Nuclear Power Plant Components in Pressure Vessel Codes and Standards. Ed. R.W. Nichols, London:Elsevier Applied Science: 79-104.

[6] ASME Boiler and Pressure Vessel Code: Section VIII - Pressure Vessels - Division I, latest edition.

[7] ASME Boiler and Pressure Vessel Code: Section VI-A - Recommended Rules for Care and Operation of Heating Boilers - Division I, latest edition.

[8] ASME Boiler and Pressure Vessel Code: Section V - Nondestructive Examination, latest edition.

[9] BSI PD6493:1980 "Guidance on Some Methods for the Derivation of Acceptance Levels for Defects in Fusion Welded Joints".

[10] Garwood, S.J. and Davey, T.G., "A Study of Biaxial Loading in A533 B", 9th Intl. Conf. on Structural Mechanics in Reactor Technology, Lausanne, Switzerland, Aug. 1987.

[11] Garwood, S.J., "Crack Tip Opening Displacement (CTOD) Methods for Fracture Assessments: Proposals for Revisions to BSI PD 6493", TWI Research Report 371/1988.

[12] Dunmore, O.J. and Parlane, A.J.A., "Fracture Mechanics Analysis of a Fillet Welded Attachment in a Pressure Vessel". Int. Conf. on Fitness for Purpose Validation of Welded Constructions, The Welding Institute, November 1981.

[13] Barsom, J.M. and Rolfe, S.T., "Correlations Between K_{IC} and Charpy-V-Notch Test Results in the Transition Temperature Range". ASTM STP 466, pp 281-302, 1970.

[14] Malik L. and Chakravarti, A.P., "Fracture Mechanics Evaluation of Pressure Vessel Containing Defects - Level II". Materials Technology Centre Report E93711-2C, July 1990.

[15] Oulton, D., "Post Failure Analysis of Defects in Vessel", Novacor Chemicals (Canada) Ltd., June 1991.

[16] Milne, I., "Application of the CEGB Procedure to the Analysis of HSST Intermediate Vessel Tests V5 and B9", Conf. Proc. Fitness for Purpose Validation of Welded Constructions; Paper No. 35.

[17] Malik, L. and Chakravarti, A.P., "Fracture Prediction of a Defective Vessel - Post-Burst Test Analysis", Materials Technology Centre Report E93711-3C, June 1991.

[18] IIW/IIS, 1988, IIW Recommendation on the Application of an Engineering Critical Assessment in Design, Fabrication and Inspection to Assess the Fitness for Purpose of Welded Structures (draft for public comment), IIW-SST-1093-88.

[19] Halmshaw, R., 1987, "Non-Destructive Testing", London, Edward Arnold.

TABLES AND FIGURES

TABLE 1: Weld Flaw Summary

Weld I.D.	Weld Type	# of Flaws	Comments
V1	1	1	Inside Vessel Surface
V2	1	2	Inside Vessel Surface
C1	2	1	Inside Vessel Surface
C2	1	2	Inside Vessel Surface
C3	2	35	Inside Vessel Surface
F1	4	1	360° Around Vessel Inside Surface (Longitudinally)
F2	4	1	360° Around Vessel Inside Surface (Longitudinally)
S1	4	Numerous	Various Sizes (Longest 32mm)
S2	4	Numerous	Various Sizes (Longest 25mm)
Head to Skirt	N.A.	0	—
Insulation Ring	N.A.	2	From O.D. Surface
Angle Iron Attachment	4	0	—
N1	3	0	Not tested from I.D. surface due to access
N1A	3	0	This nozzle was blanked off (and not through to vessel)
N2	3	0	—
N3	3	2	From I.D. Surface
N5A	3	3	From I.D. Surface
N5B	3	0	—
N6B	3	0	—
N7A	3	0	—
N7B	3	4	From I.D. Surface
N8	3	1	From I.D. Surface
MW1	3	6	(Five Areas) From Vessel I.D. Surfaces (One Under Repad)

WELD TYPE: 1 = Plate to Plate Butt 2 = Plate to Head Butt 3 = Nozzle to Shell 4 = Fillet

Table 2: Manual Ultrasonic Results for Principal Cracks of Interest

Defect Location	Description	Maximum Depth by Manual UT-1 (Full Circumference) (mm)	Position*	Maximum Depth by Manual UT-2 (mm)
Fillet F1	Intermittent for 360° at weld toe	7.62	1	--
			2	--
			3	7.9
Fillet F2	360° complete at weld toe	8.89	1	7.0
			2	7.0
			3	7.6
Manway MW1	960mm of toe cracks on inside surface	11.43	Not Applicable	
Circumferential Weld C3 Defect Designation #19	Weld repair area 95mm in length	7.62	7.11	
Splitter Plate Fillets S1/S2	Numerous cracks at fillet weld toes	5 to 6.35	Not Applicable	

*For F1/F2 1 = 0 to 400mm 2 = 800 to 1200mm 3 = 3400 to 4200mm where 0 = datum

Table 3: Results of All UT Techniques on Demister Ring Fillets F1 and F2

UT Inspection					
Defect Location	Manual UT 1	Position	Mechanized Technique A	Mechanized Technique B	Manual UT 2
F1	7.62	1	2.7	6.4	–
		2	1.9	5.7	–
		3	2.4	7.2	7.9
F2	8.89	1	4.4	–	7.0
		2	3.9	5.4	7.0
		3	4.4	6.4	7.6

*For F1/F2 1 = 0 to 400mm 2 = 800 to 1200mm 3 = 3400 to 4200mm where 0 = datum

Table 4: Details of the Vessel Materials (SA516 Gr 70) Taken From Mill Sheets

	Semi-Elliptical Heads (Hot Forged Nippon Steel)	Shell Plates (Hot Rolled Phoenix Steel)
C	0.19	0.25
Mn	1.15	1.13
P	0.015	0.019
S	0.021	0.013
Si	0.24	0.27
σ_{ys} (N/mm^2)	380	340
σ_{ts} (N/mm^2)	585	555
%E	23	25
Thickness (mm)	31.75	28.6

Table 5: Summary of Fracture Toughness Literature Search for SA516 Gr 70 Steel

Source Reference	Toughness (N/mm$^{3/2}$ or J)	Temp. ℃	Thickness, mm
ASME MPC-24	K_{IC} = 5625	RT	--
Nguyew-Duy, Int. J. Fract. Vol. 18, No. 2, 1982	K_{IC} = 3200	--	--
WRC Bulletin 299	K_{IC} (from CVN) = 4500 K_{IC} = 7000	-- --	-- 40
Wilson, ASTM STP 668	K_{IC} = 4600	93	51 (normalized)
Bellamy, Ontario Hydro Report M83-3-7	C_v = 21,28,30	0	38 (as received)

Table 6: Summary of Failure Pressure Predictions (Zero Residual Stress) - Level I - Preliminary Fracture Analysis

Defect Identity	Failure Pressure, MPa	
	Fracture	Plastic Collapse
Demister Ring Defect - Figure 13a	8.0	15.0
Weld C3 Circumferential Defect - Figure 13b(i)	16.20	18.50
Weld C3 Axial Defect - Figure 13b(ii)	5.10	8.60
Weld C1 Axial Defect - Figure 13c	7.80	9.50
Weld V1 Circumferential Defect - Figure 13d	*	19.70
Weld V2 Axial Defect - Figure 13e	*	9.90
Splitter Plate Axial Defect - Figure 13f(i)	*	9.8
Splitter Plate Circumferential Defect - Figure 13f(ii)	10.20	16.20
Manway 1 Defect - Figure 13g(i)	8.50 (4.9)+	16.80 (12.8)+
Manway 2 Defect - Figure 13g(ii)	9.4 (8.8)++	19.2 (18.1)++
Manway 4 Defect - Figure 13g(iii)	6.70	13.60

*Crack driving force too small.
+Bracketed Value - assuming defect in PV wall, i.e. presence of repad ignored.
++Bracketed Value - assuming second repad is removed.

Table 7: Tensile Test Results

Spec. No.	Orientation and Location	Yield Strength (MPa)	Ultimate Strength (MPa)	% Elongation
W1-11	All Weld Metal Parallel to Weld C2	476	604	33.4
W1-12		404	590	32.9
W1-13	Base Material Parallel to Weld C2 (for axial defects subject to hoop stress)	306	579	34.4
W1-20	Base Material Perpendicular to Weld C2 (for circumferential defects subject to axial stress)	344	583	29.0

(All specimens were 4.5mm diameter, 15.25mm gauge length and removed from the T/4 position.)

Table 8: Charpy V-Notch Toughness Results (at 20°C)

Spec. Axis	Notch Location	Energy Absorbed, J	Avg. % Shear
Perp. to Weld C2	Weld Metal*	85, 91, 79 (avg. 85)	67
Perp. to Weld C2	Heat Affected Zone**	106, 117, 96 (avg. 106)	100
Perp. to Weld V1	Weld Metal*	63, 65, 71 (avg. 66)	51
Perp. to Weld V1	Heat Affected Zone**	120, 136, 140 (avg. 132)	100
Parallel to Weld C2	Base Material	52, 59, 54 (avg. 55)	58
Perp. to Weld C2	Base Material	78, 80, 66 (avg. 75)	60

Weld C2 is circumferential, and Weld V1 is axial.

* 2mm subsurface, weld metal centreline.

**Approx. T/4 position to maximize notch location in the HAZ.

Table 9: CTOD-R Curves for the Specimens Tested**

Specimen No.	Specimen Axis**	Notch Location	k	Avg. k	n	Avg. n	CTOD (mm) at Δa = 0.2 mm	Comment
W1-1 W1-2 W1-3	Perpendicular to Weld C2	Weld Metal	.3367 .4824 .4489	0.4227	.5940 .6007 .6509	0.6152	0.157	
W1-4 W1-5 W1-6	Perpendicular to Weld C2	Heat Affected Zone	.3132 .4631 .5476	0.4413	.4182 .6025 .3705	0.4637	0.209	
W1-14 W1-15 W1-16	Parallel to Weld C2	Base Material	.5020 .5127 .4878	0.5008	.4226 .6774 .4946	0.5305	0.213	Use for axial defects subject to hoop stress
W1-17* W1-18 W1-19	Perpendicular to Weld C2	Base Material	.5884 .5313	0.5599	.2964 .4857	0.3911	0.298	Use for circumferential defects subject to axial stress

CTOD (mm) = $k \cdot (\Delta a)^n$
Weld C2 is circumferential
*Specimen accidentally overloaded
**Specimens were BXB, side grooved and with a/w $\pm$0.5

Table 10: Summary of Failure Pressure Prediction (Stage II)

Figure for Defect	Stress	Flaw Tip Location	Residual Stress (MPa)	Fracture Stress (MPa)	Failure Pressure (MPa)
Fig 12a	Axial	Base Material	0	302	18.8
		Base Material	86	297	18.6
Fig 12b(ii)	Hoop	Base Material	0	303	9.5
		Base Material	76	299	9.3
		Weld Metal	0	301	9.4
		Weld Metal	76	289	9.0
Fig 12b(i)	Axial	Base Material	0	373	23.3
Fig 12c	Hoop	Base Material	0	341	10.7
Fig 12e	Hoop	Base Material	0	355	11.1
Fig 12f	Hoop	Base Material	0	352	11.0
Fig 12g (defect 1) 11.43 mm deep	Radial at 45°	Base Material	0	222	9.5
		Base Material	81	201	8.6
		Weld Metal	0	208	8.9
		Weld Metal	81	163	7.0
8.89 mm deep		Base Material	0	259	11.1
		Base Material	81	249	10.7
		Weld Metal	0	251	10.8
		Weld Metal	81	226	9.7

Table 11: Summary of Failure Pressure Prediction From Defects Shown in Figures 13a and 13b(ii) Under Various Assumptions

Figure for Defect	Stress	Flaw Tip Location	Residual Stress (MPa)	Stress for Tangential Driving Force Curve (MPa)	Approximate Stable Crack Growth (mm)	Failure Pressure (MPa)
Fig 12a	Axial	Base Material	0	~ 299	0.15	18.7
		Base Material	86	~ 295	0.25	18.5
Fig 12b(ii)	Hoop	Base Material	0	~ 302	0.20	9.4
		Base Material	76	~ 299	0.35	9.3
		Weld Metal	0	301	0.30	9.4
		Weld Metal	76	198	0.50	9.3

Table 12: Acoustic Emission Intensity Rating - MONPAC and Hydrotest Portion

Sensor	Closest Defect	AE Intensity Rating			
		Unfiltered Data		Filtered Data	
		MONPAC	Hydro	MONPAC	Hydro
1	C1/V1	C	D	A	B
2	Demister Ring	C	C	A	B
3	Demister Ring	C	C	C	B
4		C	C	A	A
5	N1	C	C	A	A
6	C2/V2	D	D	A	A
7	C3/Defect #19	C	C	A	A
8		C	C	B	A
9		C	D	B	A
10		C	C	C	C
11		C	D	B	A
12	N1	C	D	A	--
13		C	D	B	--
14		C	C	A	A
15		--	--	--	--
16	Manway	C	D	B	A
17	Manway	C	D	--	--
18	Manway	B	A	--	--
19	N1 Splitter Plate	D	D	--	--

AE Intensity Ratings

-- Insignificant AE Sources
A Minor defect; note for reference on future tests
B Note on future tests. Check for surface defects such as corrosion/pitting/gouges/cracked fillet welds.
C Defect requiring follow up evaluation
D Immediate follow up inspection with NDT methods
E Immediate shutdown until inspection with NDT methods.

TABLE 13: Summary of Flaw Depth Determination

Flaw Location		Manual UT 1st Assessment	Manual UT 2nd Assessment	TOFD Tech.	Digitized* Pulsed Echo Technique	Fractography
Manway MW1 Fig. 13g		11.43				2.0
Weld C3 Fig. 13b(ii) Fig. 13b(i)		7.62 3.56	7.11			2.70 2.84
Demister Ring Fig. 13a	F1	7.62	– – 7.90	2.70 1.90 2.40	5.20 0.0 6.20	1.92 2.36 3.20
	F2	8.89	7.0 7.0 7.6	4.4 3.9 4.4	6.70 6.20 6.70	4.32 4.36 4.77
Splitter Plate Fig. 13f	S1	6.35				3.57
	S2	5.08				4.76

* Corrected value after further manipulation of data by contractor; slightly different from values in Table 3.

TABLE 14: Summary of Flaw Length Determination (mm)

Flaw Location	Manual UT	Fractography
Manway MW1 Figure 13g	22.22 (Recorded as Continuous)	12 & 9 (Revealed to be Discontinuous)
Weld C3 Figure 13b(ii)	95.25	55
Splitter Plate Figure 13f	28.58* 25.4*	28.59 9.52

*Not specifically recorded as S1 or S2

TABLE 15: SUMMARY OF FAILURE PRESSURE PREDICTION FROM PRELIMINARY AND DETAILED FRACTURE ANALYSES (All Figures Assuming Zero Residual Stress)

Defect Identity	Simple Failure Pressure, MPa		Complex Failure Pressure, MPa	
	Fracture	Plastic Collapse	Plastic Collapse	
Demister Ring Defects - Figure 13a	8.0	15.0	18.8[3]	
Weld C3 Circumferential Defect - Figure 13b(i)	16.20	18.50	23.3[3]	
Weld C3 Axial Defect - Figure 13b(ii)	5.10	8.60	9.4[2] 9.5[3]	
Weld C1 Axial Defect - Figure 13c	7.80	9.50	10.7[6]	
Weld V1 Circumferential Defect - Figure 13d	*	19.70		
Weld V2 Axial Defect - Figure 13e	*	9.90	11.1[3]	
Splitter Plate Axial Defect - Figure 13f	*	9.8	11.0[2]	
Splitter Plate Circumferential Defect - Figure 13f(ii)	10.20	16.20		
Manway Defect 1 - Figure 13g(i)	8.50	16.80	8.9[5] - 9.5[6]	10.8[5]-11.1[6]
Manway Defect 2 - Figure 13g(ii)	9.40	19.20		
Manway Defect 4 - Figure 13g(iii)	6.70	13.60		

*Crack driving force too small
[1]Base material
[2]Weld metal
[3]Weld metal - defect 11.43mm deep
[4]Base metal - defect 11.43mm deep
[5]Weld metal - defect 8.89mm deep
[6]Base metal - defect 8.89mm deep

TABLE 16: FAILURE PRESSURES CORRESPONDING TO DEFECT SIZE MEASUREMENTS BASED ON PRE-BURST TEST NDE*, AND ON POST-BURST TEST FRACTOGRAPHY (Zero residual stress; crack tips in base material)

Defect Location	Demister Ring Fig.13a	Weld C3 Axial Fig.13b(ii)	Weld C1 Axial Fig.13c	Weld V2 Axial Fig.13e	Splitter Plate End Fig.13f	Manway Defect 1 Fig.13g
Defect Depth (mm)						
NDE	7.62	7.62	5.08	5.08	6.35	11.43
Fractography	4.77	2.70	0.30	1.70	4.76	2.0
Defect Length (mm)						
NDE	Full Circum.	95.3	38.2	12.7	12.7	965
Fractography	Full Circum.	~55.0	40.0	12.7	28.6	965
Failure Pressure Preliminary Analysis						
NDE-Plastic Collapse	15.0	8.6	9.5	9.9	9.8	16.8
Fractography-Plastic Collapse	17.1	9.8	10.2	10.1	9.7	19.8
NDE-Fracture	8.0	5.1	7.8	**	**	8.5
Fractography-Fracture	**	**	**	**	**	**
Failure Pressure Detailed Analysis						
NDE	18.8	9.5	10.7***	11.1***	11.0***	9.5
Fractography	21.2***	11.3***	11.3***	11.3***	10.8	15.1***

*Using magnetic particle and manual ultrasonic data only.

**Crack driving force too small in simple analysis.

***Internal pressure for plastic collapse, i.e. net section stress equal to flow stress.

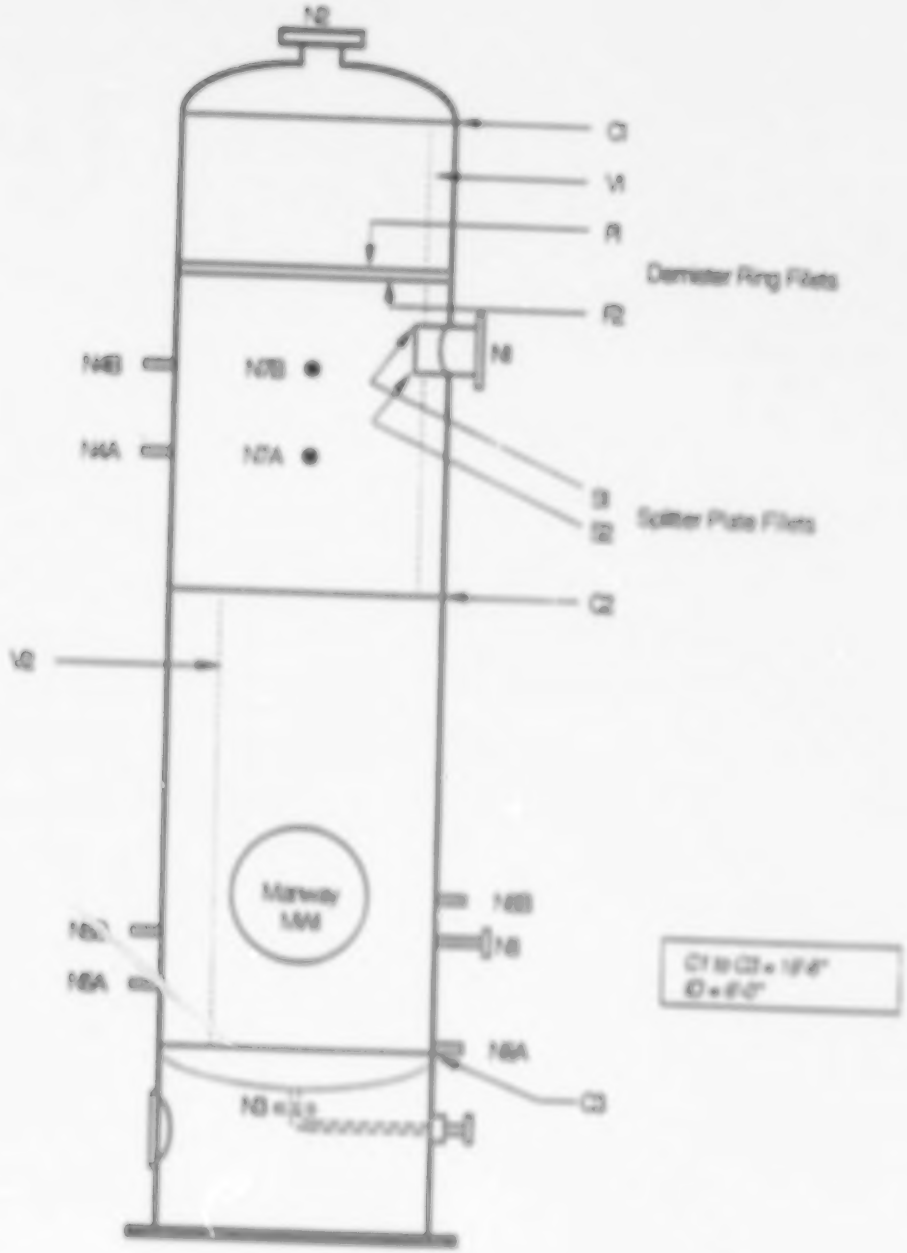

Figure 1: Schematic of Vessel, Illustrating Major Weld Locations

Figure 2: View of vessel after removal of reinforcing band over internal fillet welds F1 and F2 (arrowed). The additional reinforcement to the manway is still in place.

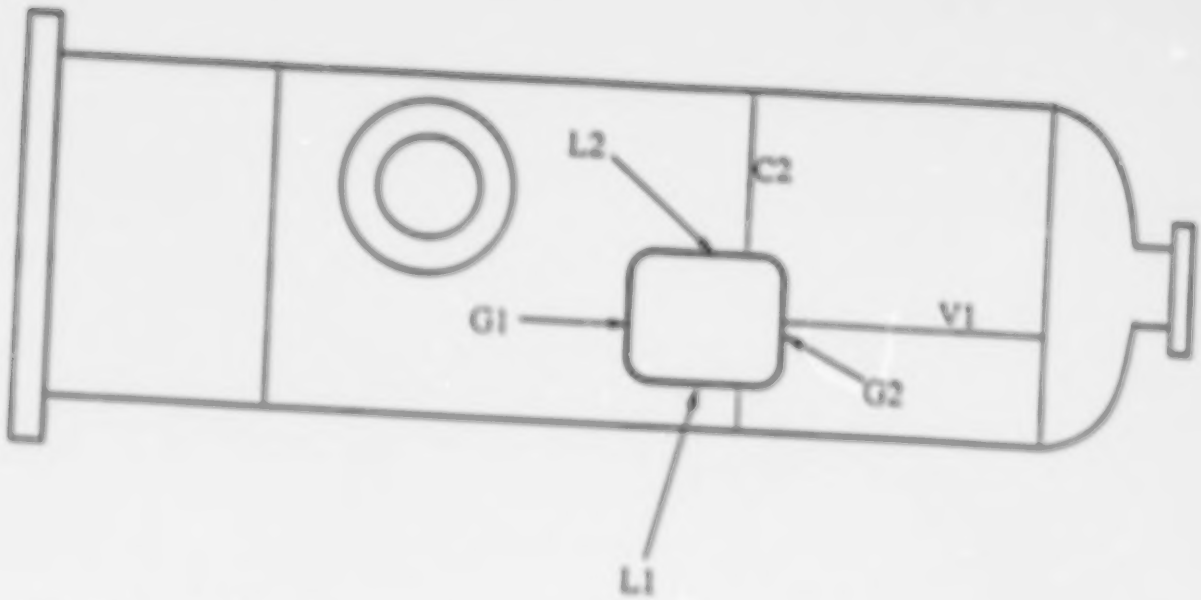

Figure 3 Schematic diagram showing location of patch insert and identification of longitudinal and girth seams

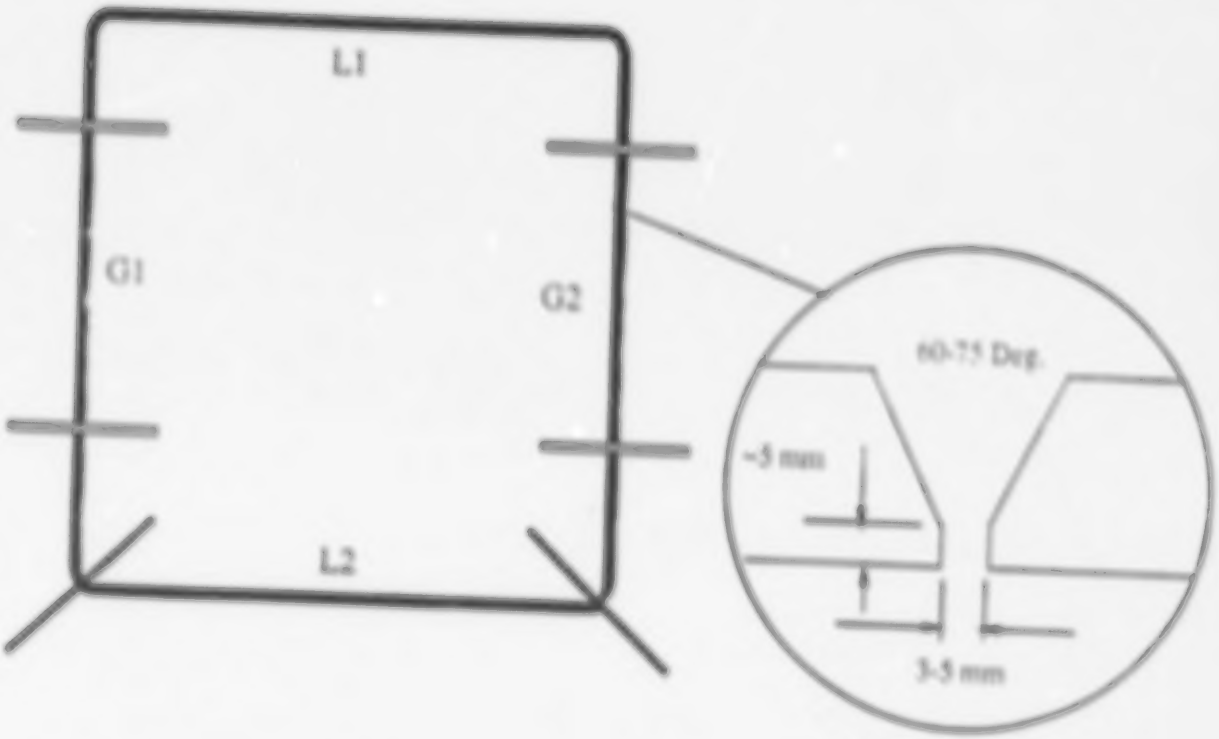

Figure 4 Schematic diagram showing fairing attachments and joint design preparation for patch insert

Figure 5: Representative photograph showing patch insert plate (preheat elements and insulating blankets positioned on exterior shell)

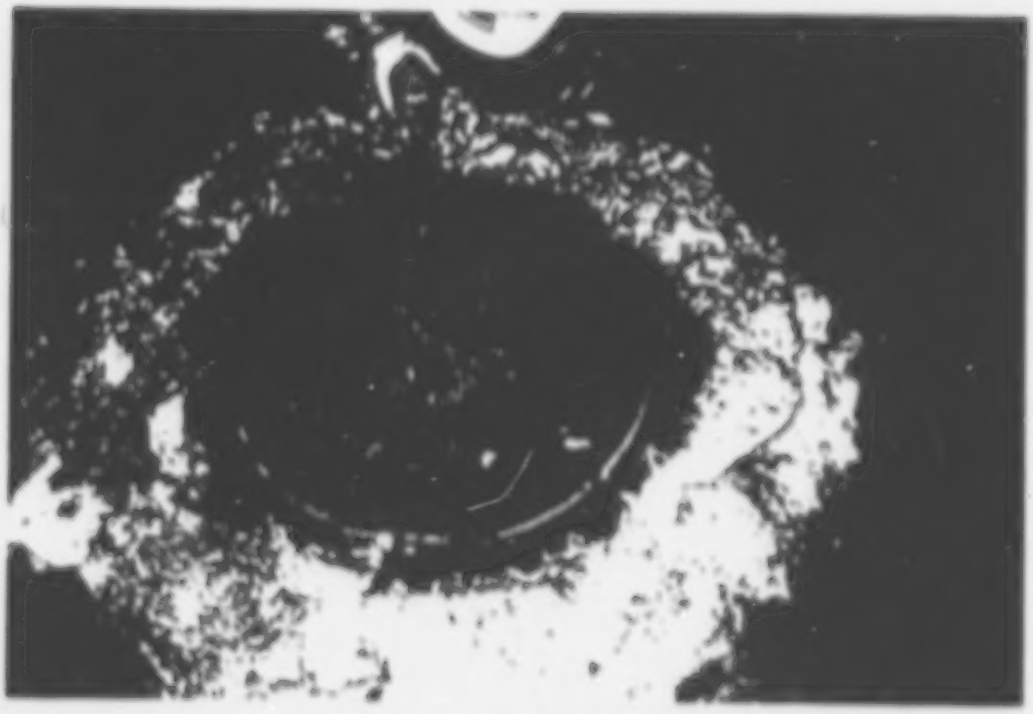

Figure 6: Manway sealing. Magnetic Particle Inspection (MPI) of root pass.

Figure 7: Typical toe cracking at demister ring fillet weld F2

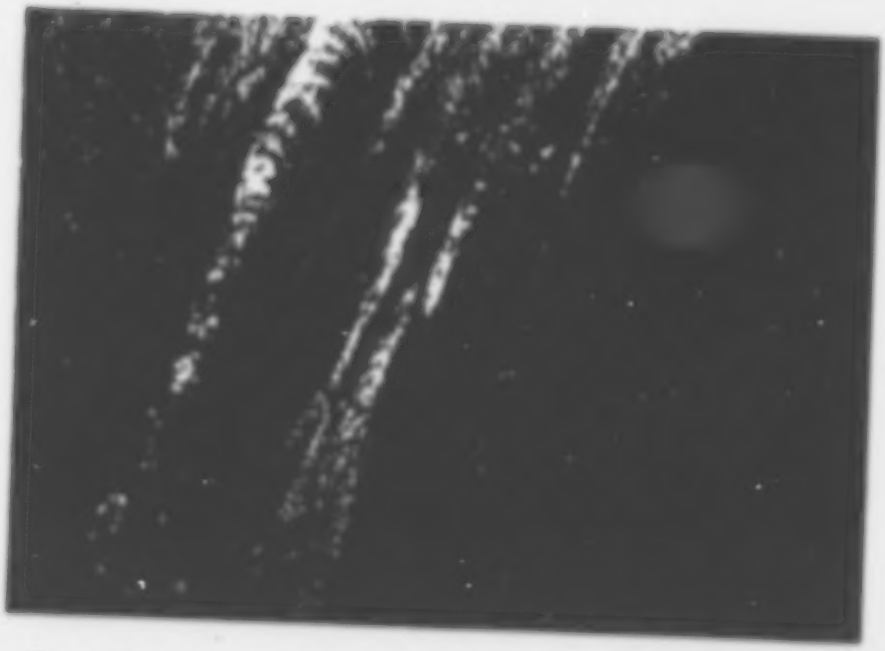

Figure 8: Cracking in HAZ of repair weld at manway (MW1). Also shown are transverse cracks on nozzle pipe.

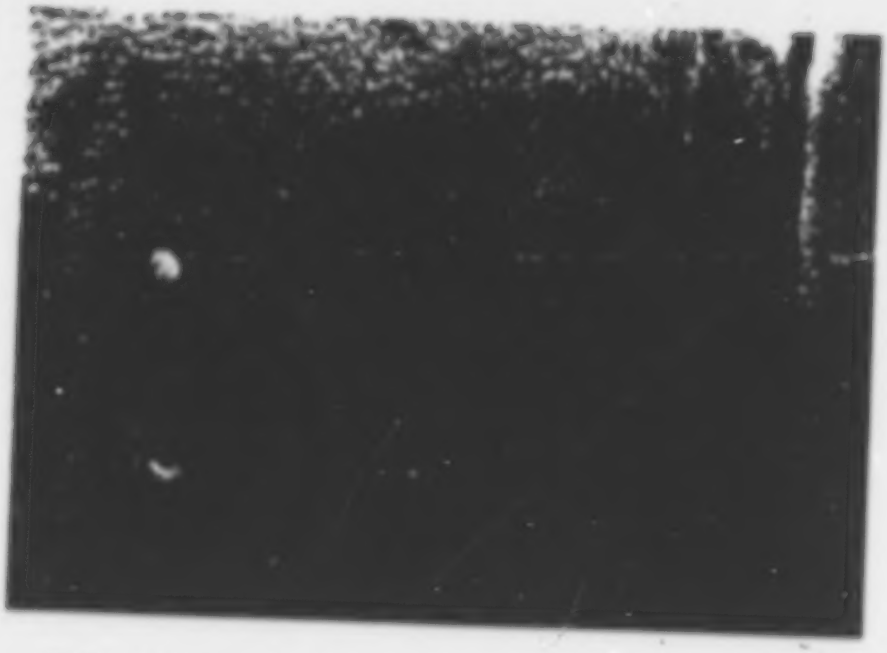

Figure 9: Defect designated as #19, transverse to circumferential weld C3

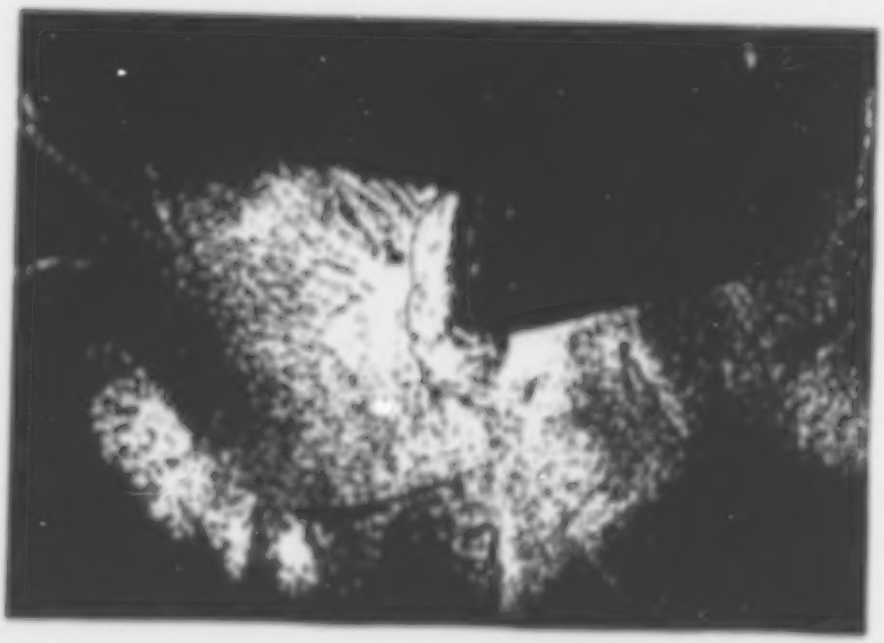

Figure 10: Typical cracking at toe of Splitter Plate fillet weld S2

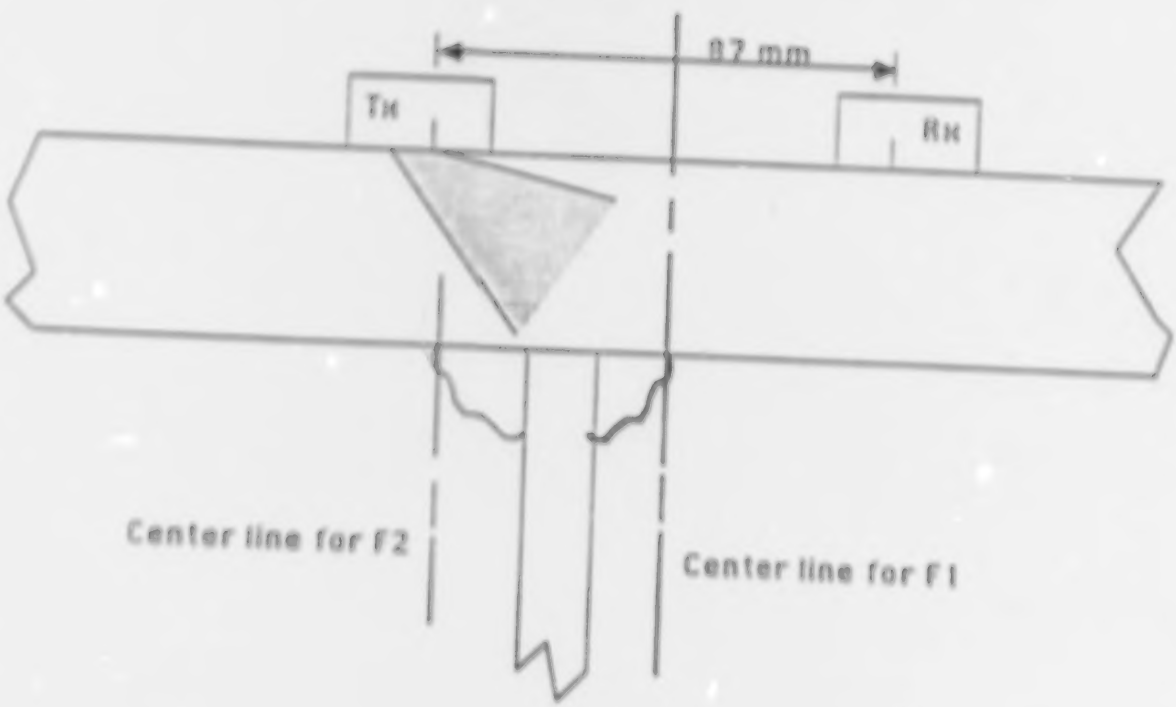

Figure 11: Time Of Flight Diffraction (TOFD) transducer arrangement for Welds F1 and F2

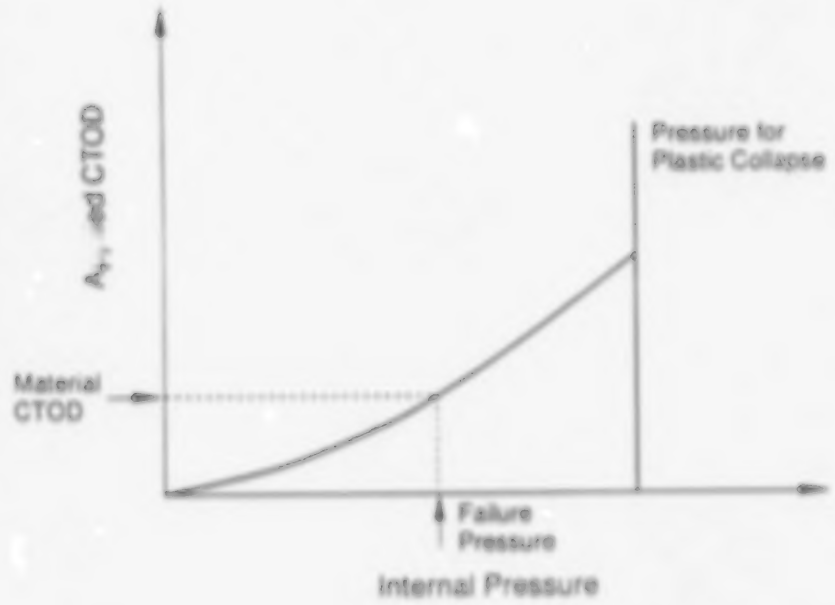

Figure 12: Estimating Failure Pressures in the Preliminary Approach (Schematic)

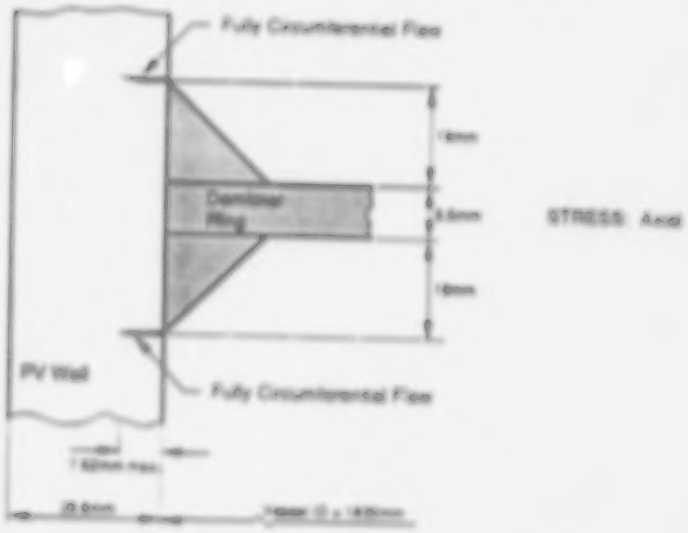

Figure 13a: Demister Ring Flaws

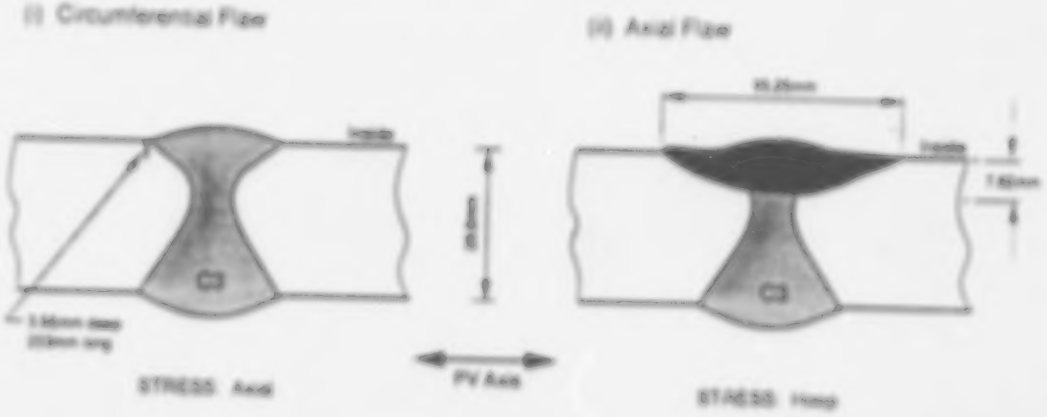

Figure 13b: Weld C3 Flaws

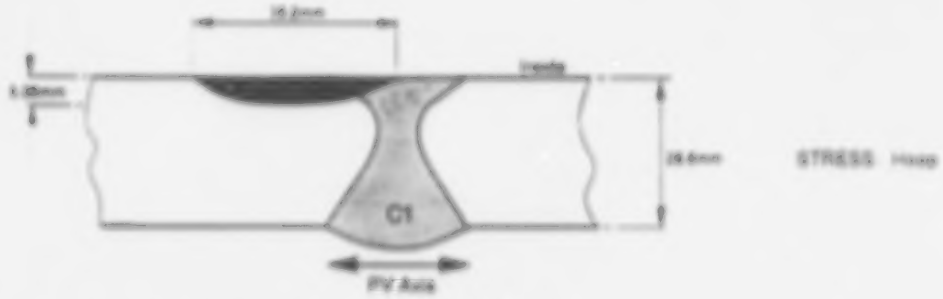

Figure 13c: Weld C1 Axial Flaw

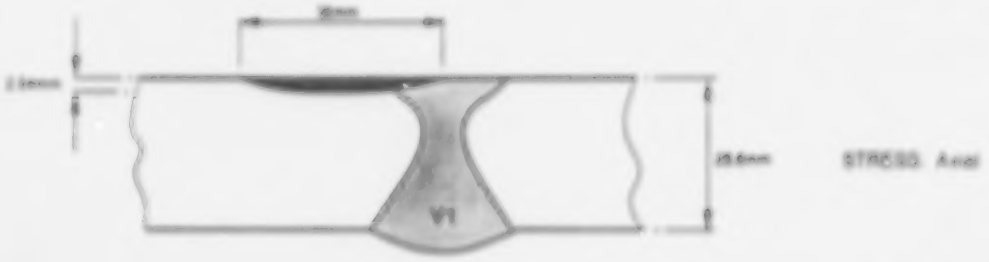

Figure 13d: Weld V1 Circumferential Flaw

Figure 13e: Weld V2 Axial Flaw

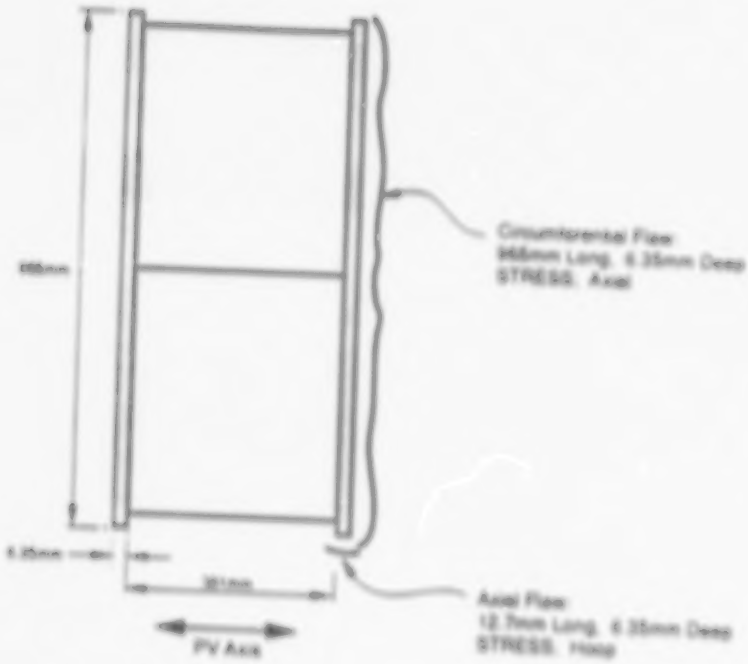

Figure 13f: Splitter Plate Flaws

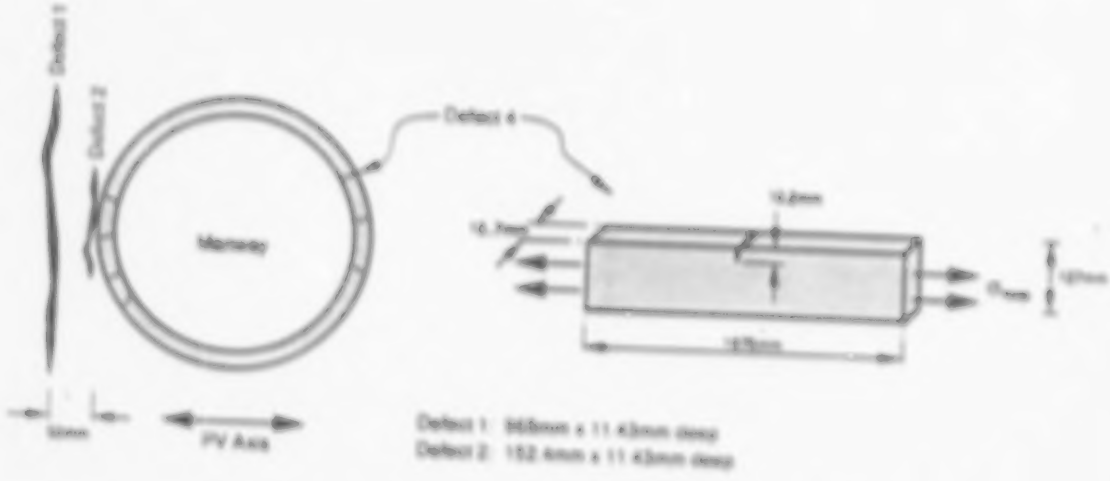

Figure 13g: Manway Defects

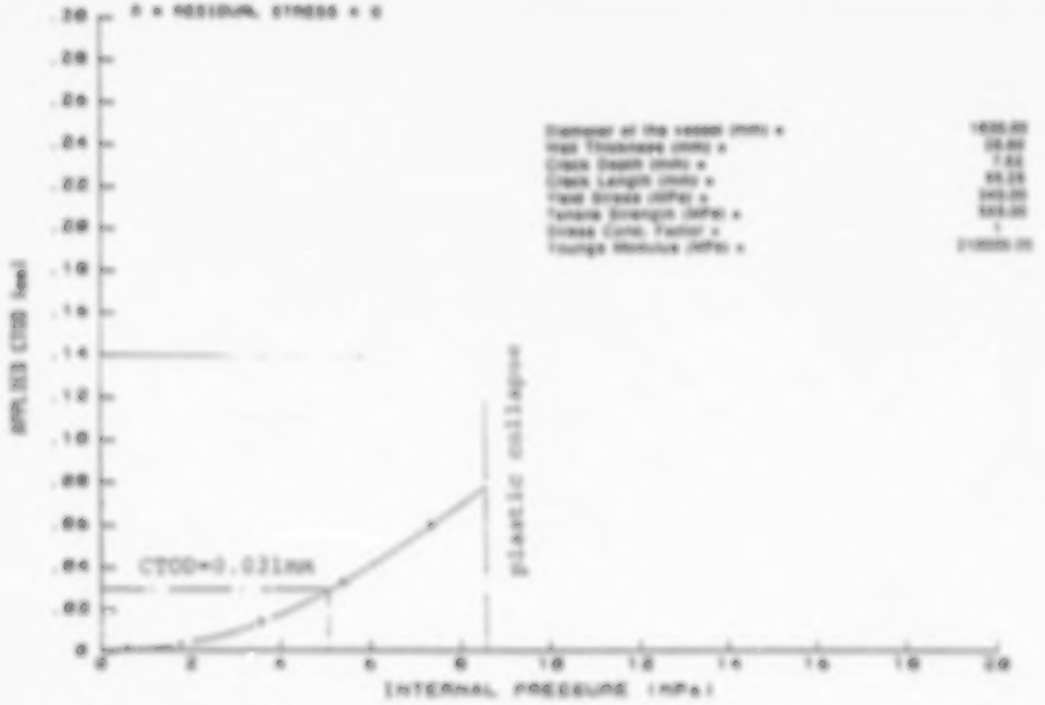

Figure 14a Weld C3 axial flaws (refer to Figures 9 and 12b)

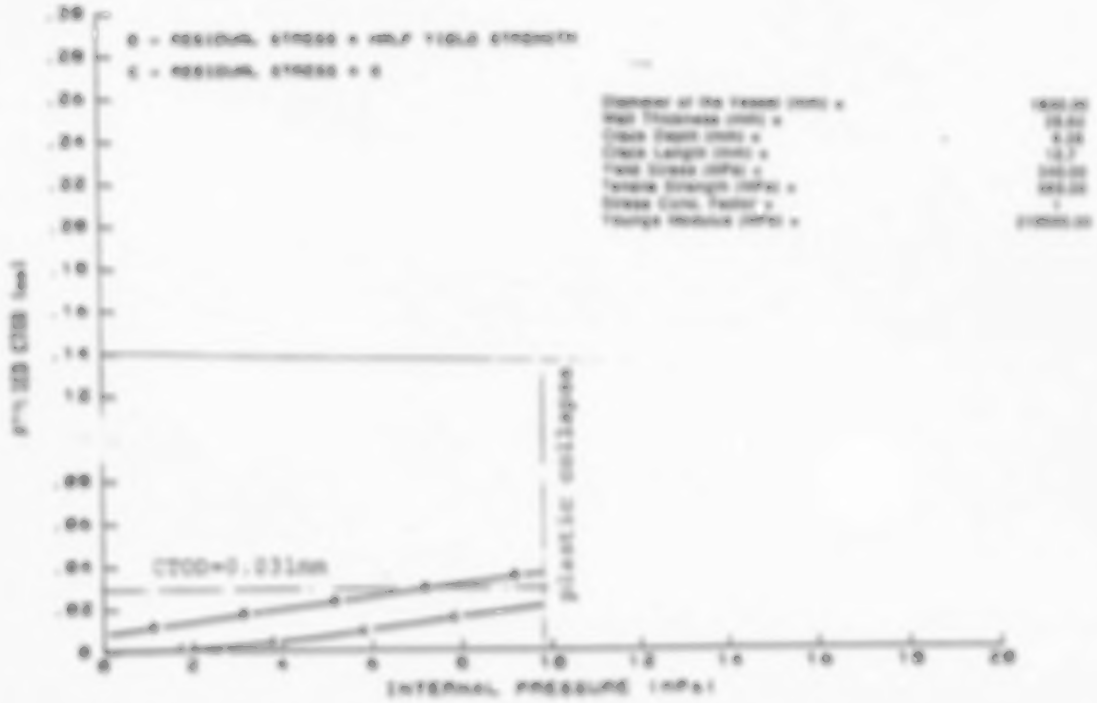

Figure 14b Splitter plate axial flaws (refer to Figures 10 and 12f)

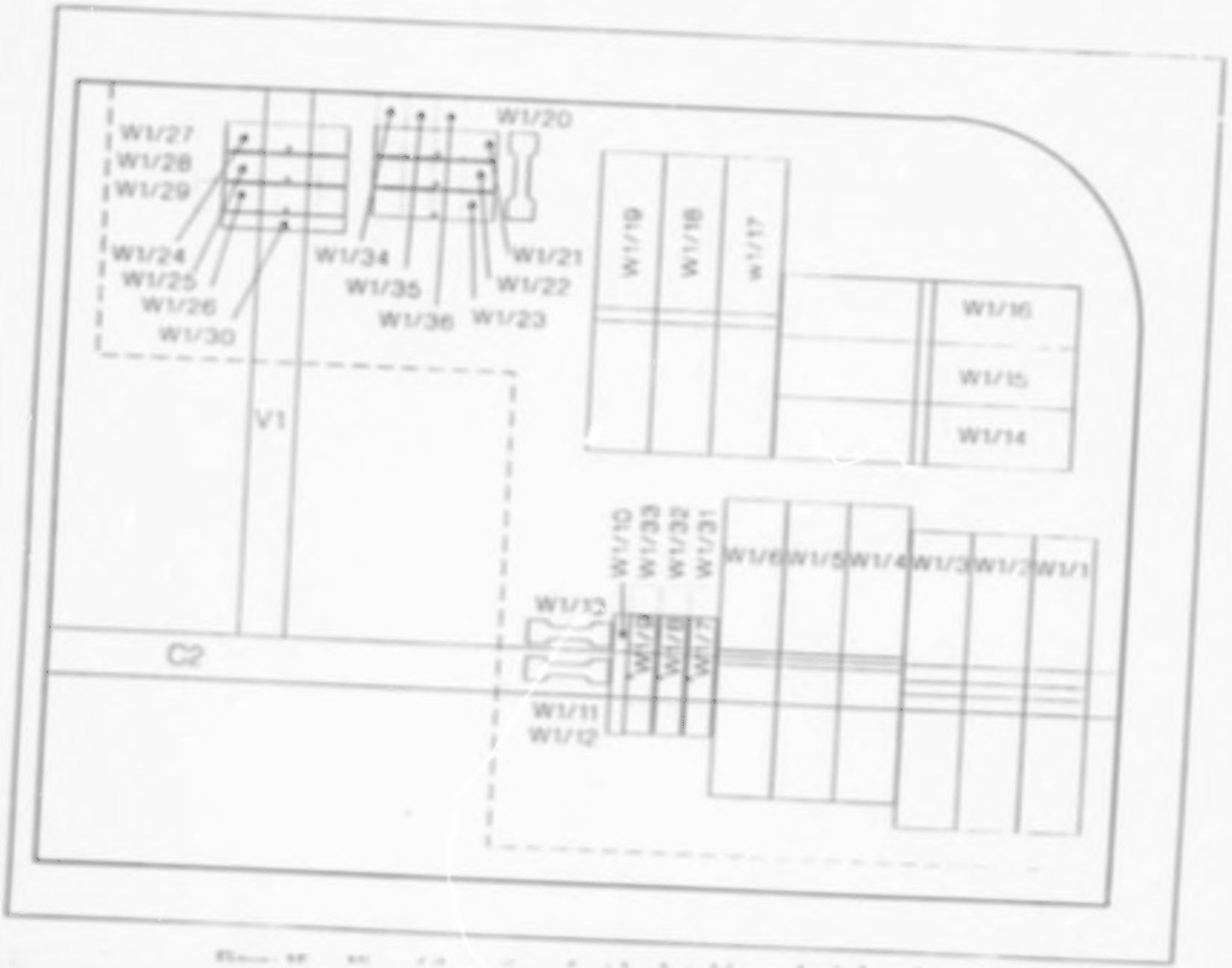
W1/27
W1/28
W1/29
W1/24
W1/25
W1/26
W1/30
W1/34
W1/35
W1/36
W1/20
W1/21
W1/22
W1/23
V1
W1/19
W1/18
W1/17
W1/16
W1/15
W1/14
W1/10
W1/9
W1/8
W1/7
W1/6
W1/5
W1/4
W1/3
W1/2
W1/1
W1/13
C2
W1/11
W1/12

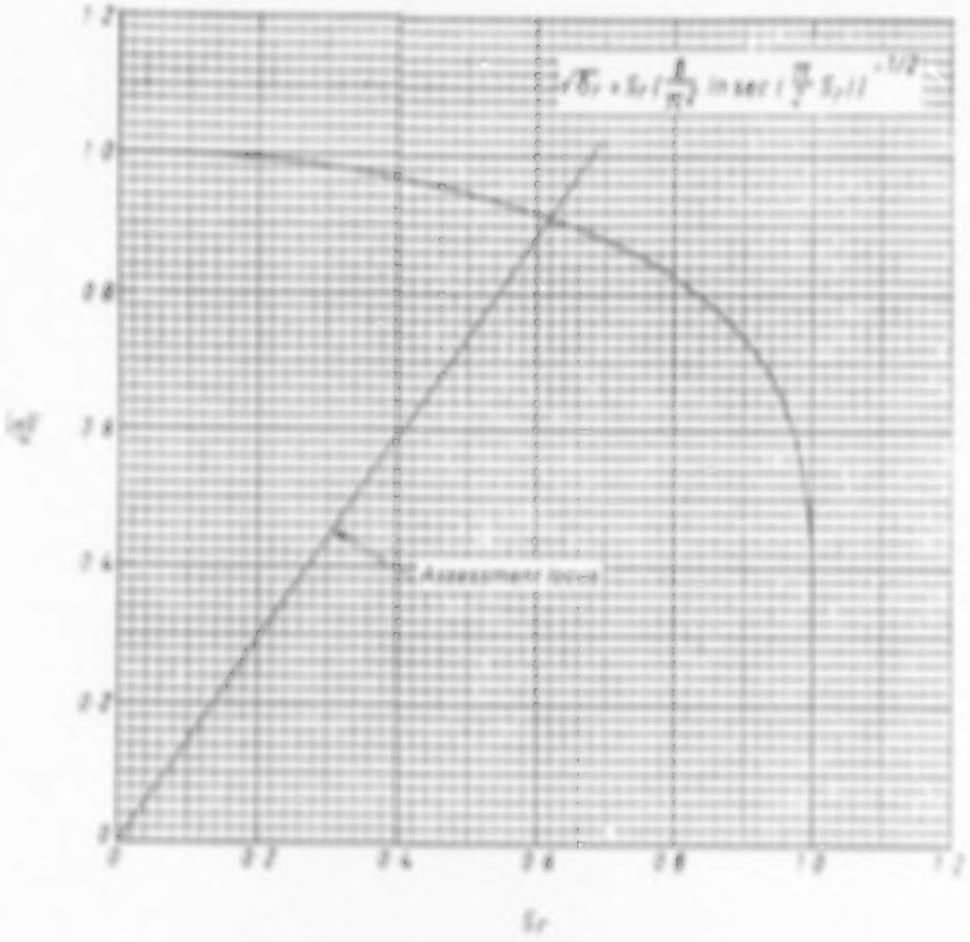

Figure 1b: Level 2 FAD with assessment locus (from Ref. 11)

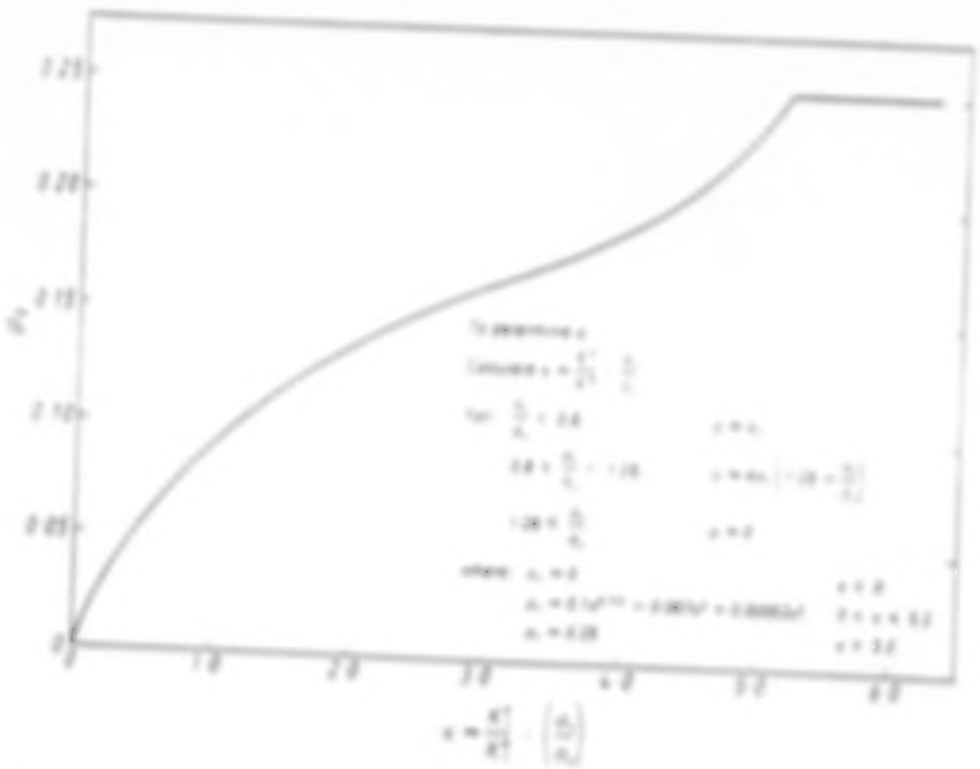

Figure 17 Values of ρ, the plasticity interaction term between primary and secondary stresses (from Ref. 11)

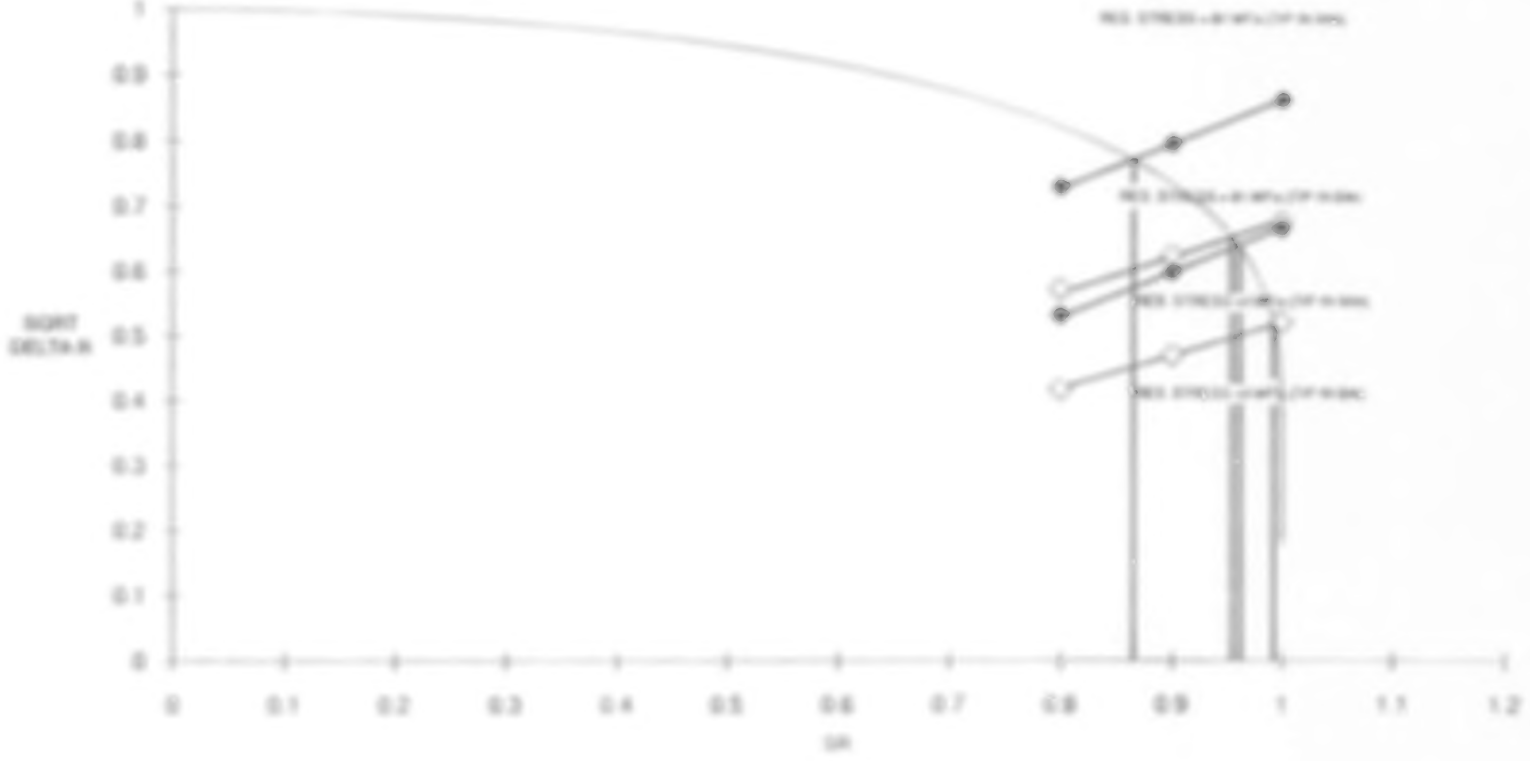

Figure 10: Stress Ratio, SR, for Failure from Defect 1 shown in Figure 13g based on δ_{max} = 0.256 mm for Base Material and .157 mm for Weld Metal; Yield Strength = 325 MPa and Flaw Depth = 8.89 mm

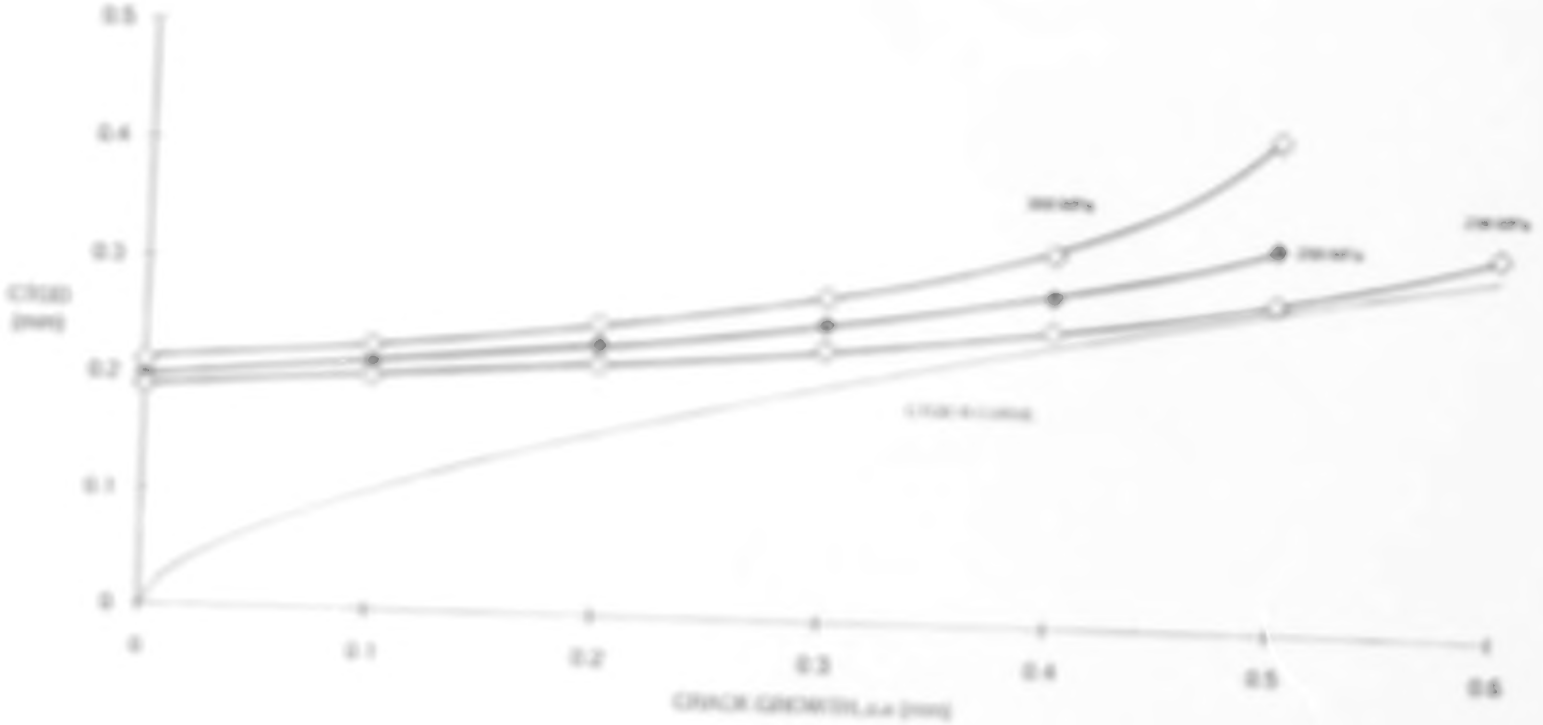

Figure 19: CTOD-R Curve (Average) and Driving Force Curves for the Flaw shown in Figure 18b. (Residual Stress = 76.5 MPa. Flaw Tip in the Weld Metal)

Figure 20

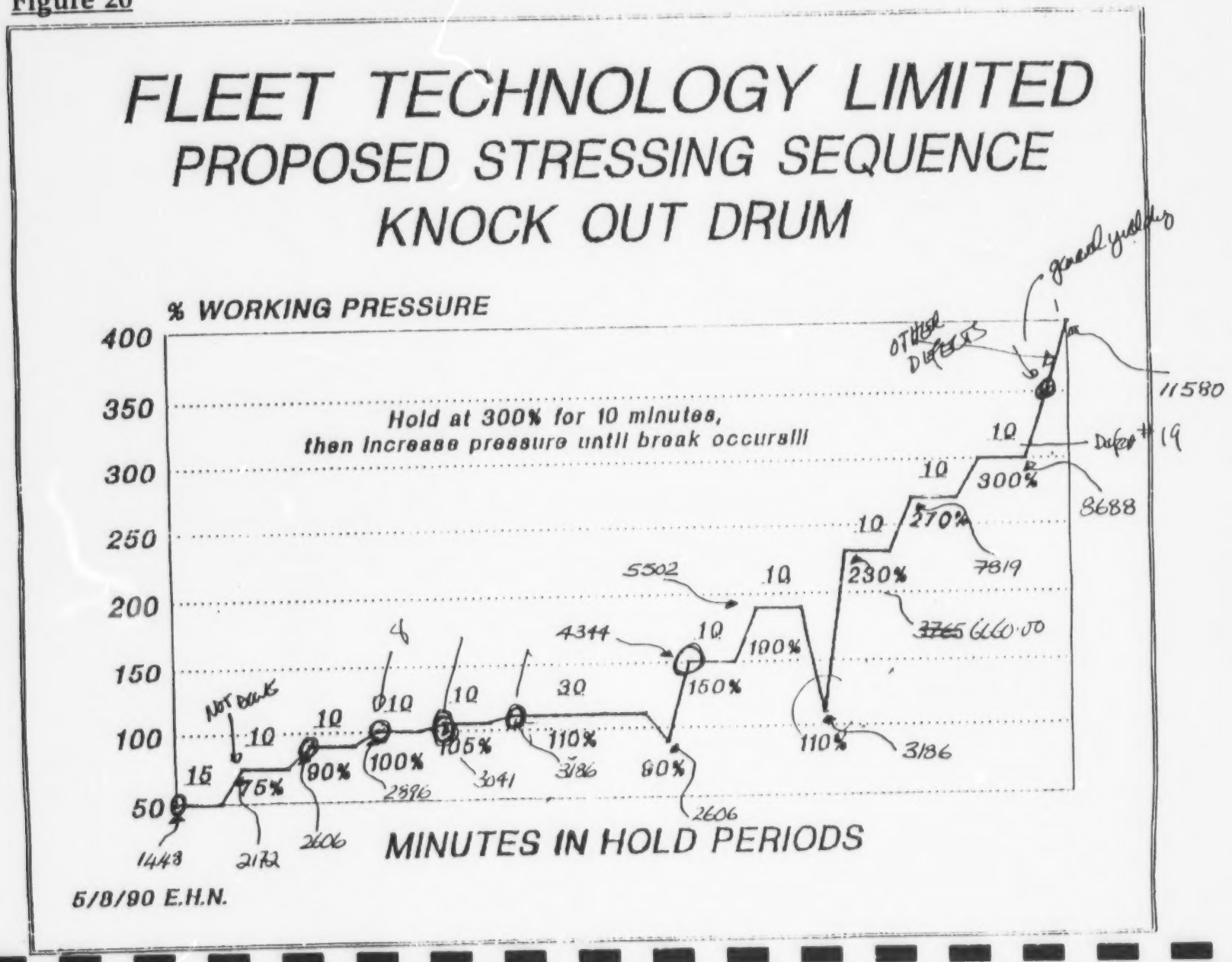
FLEET TECHNOLOGY LIMITED
PROPOSED STRESSING SEQUENCE
KNOCK OUT DRUM
% WORKING PRESSURE
400
350
300
250
200
150
100
50
Hold at 300% for 10 minutes,
then increase pressure until break occurs!!!
MINUTES IN HOLD PERIODS
5/8/90 E.H.N.

Figure 21: Hydrotest Pressure Chart

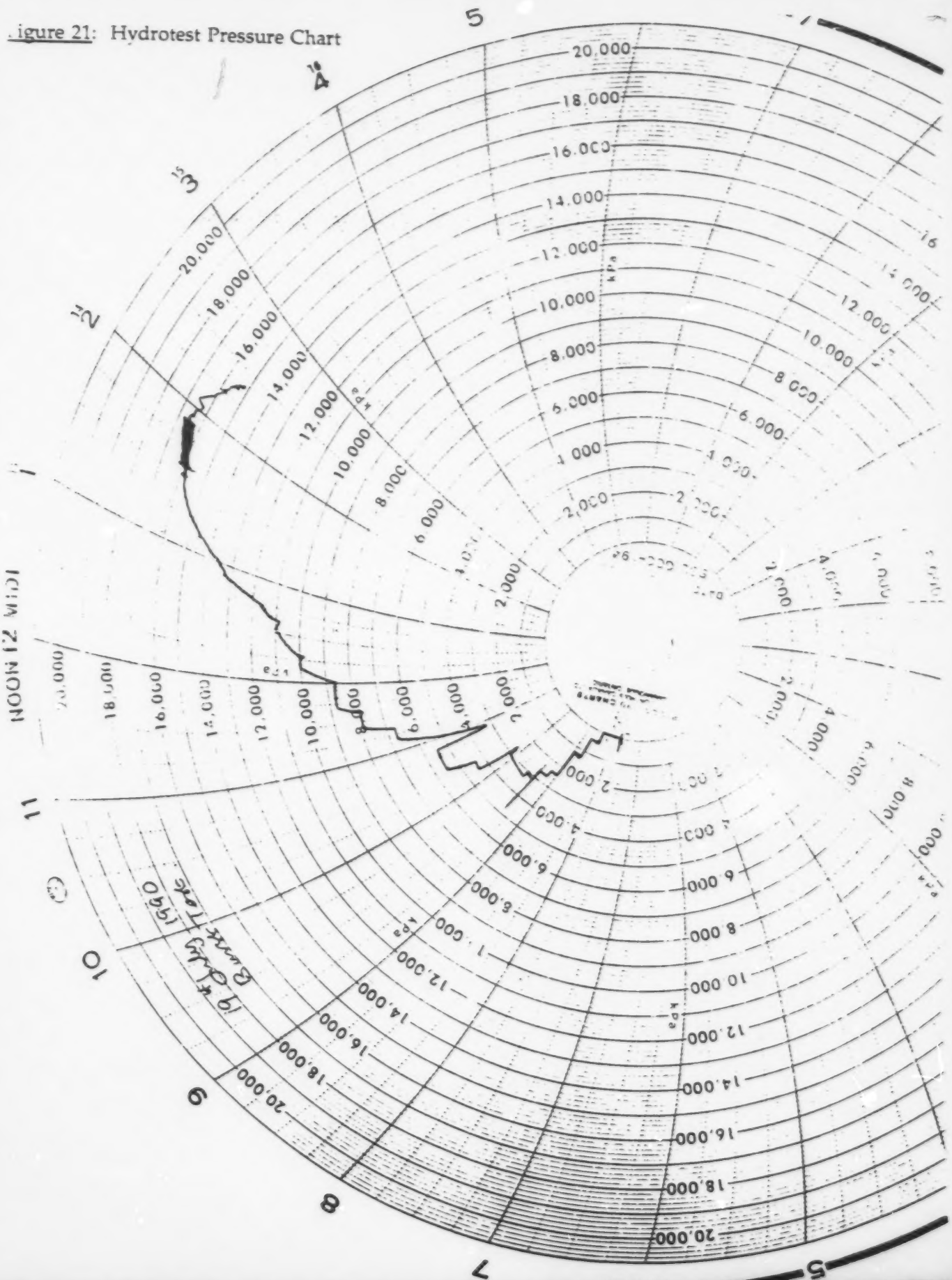

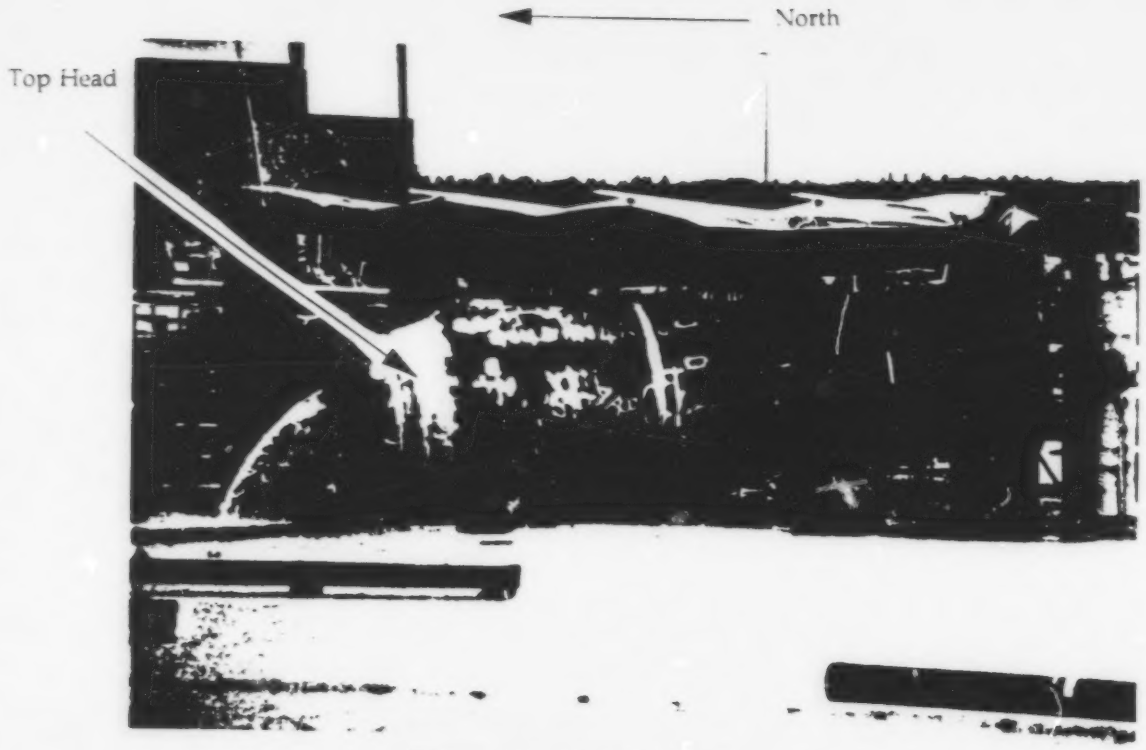

Figure 22: Vessel after burst test

Figure 23: Showing splitter plate and crack arresting in nozzle N2 attachment weld

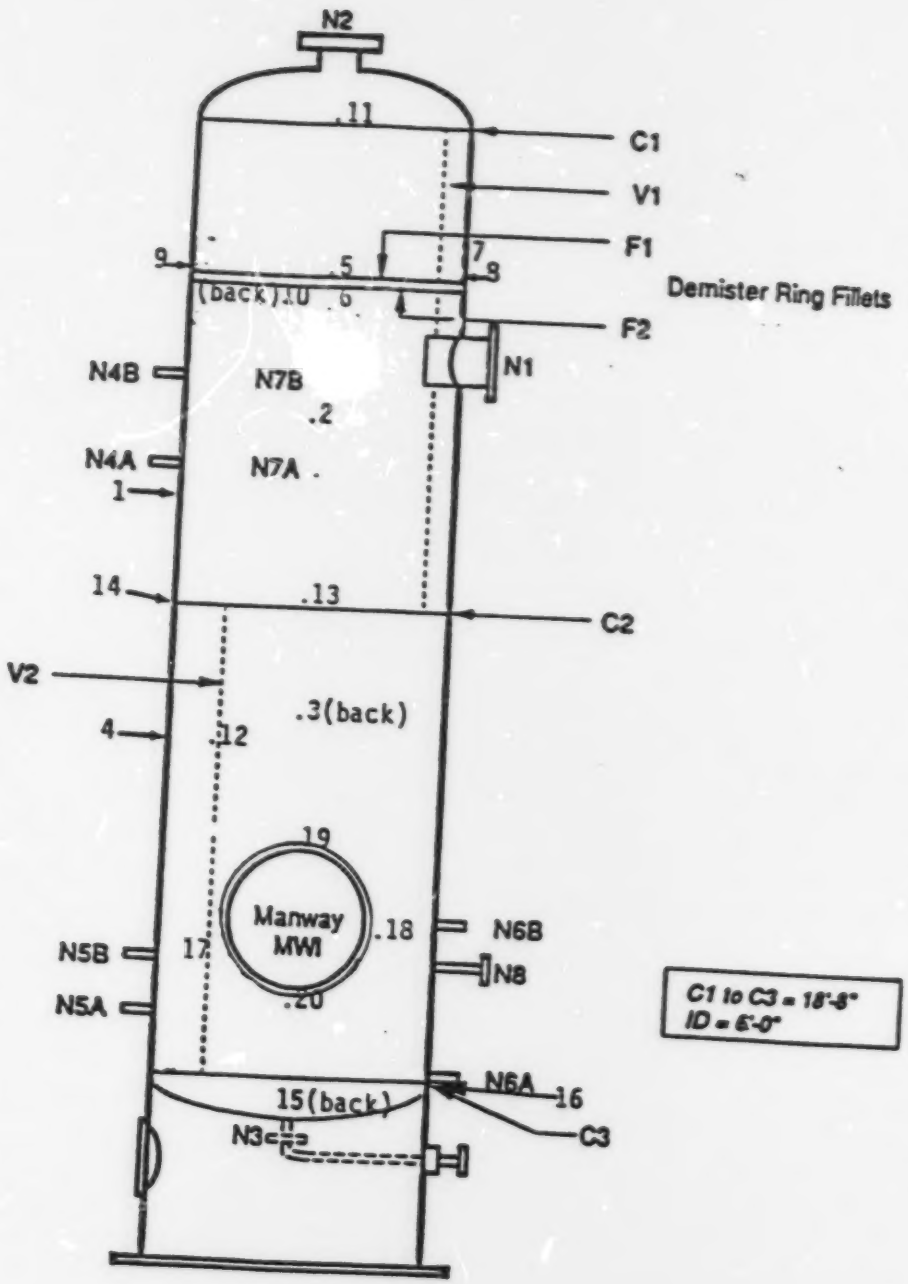

Figure 24: Strain gauge locations

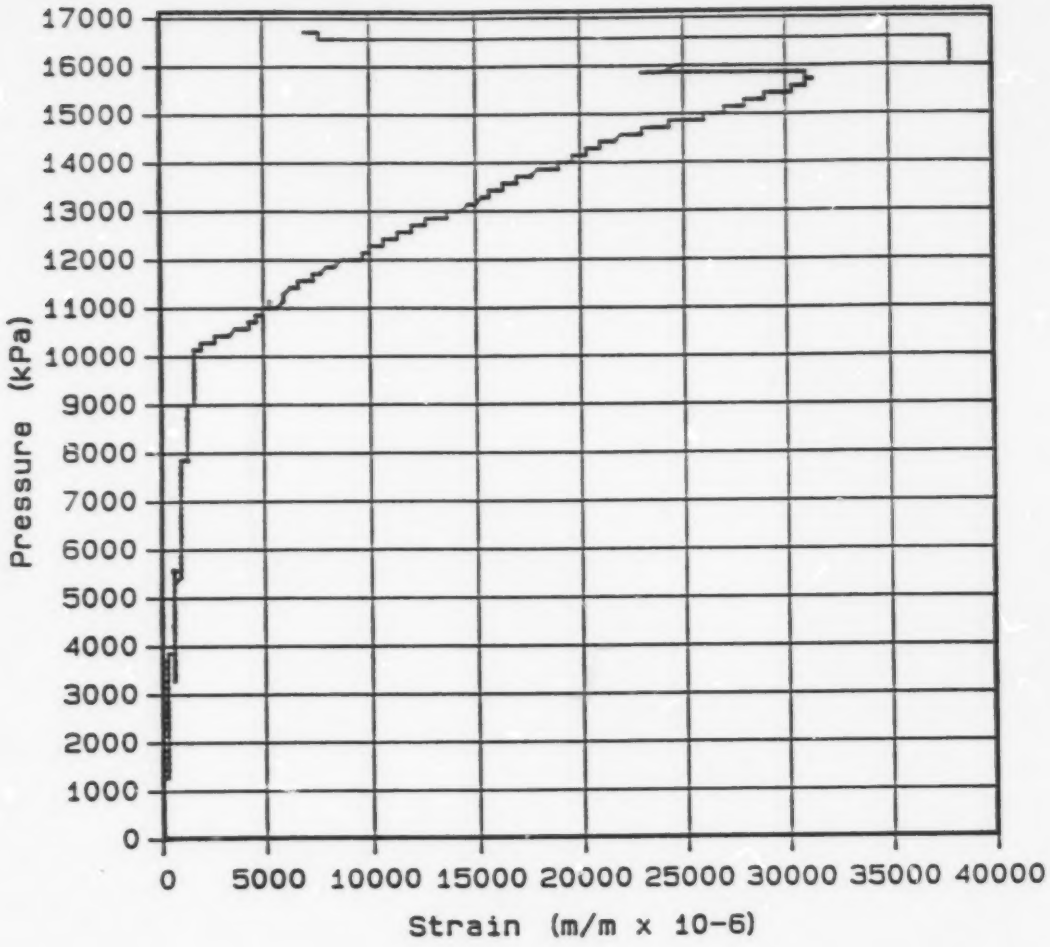

Figure 25: Typical plot of pressure versus circumferential strain in upper shell

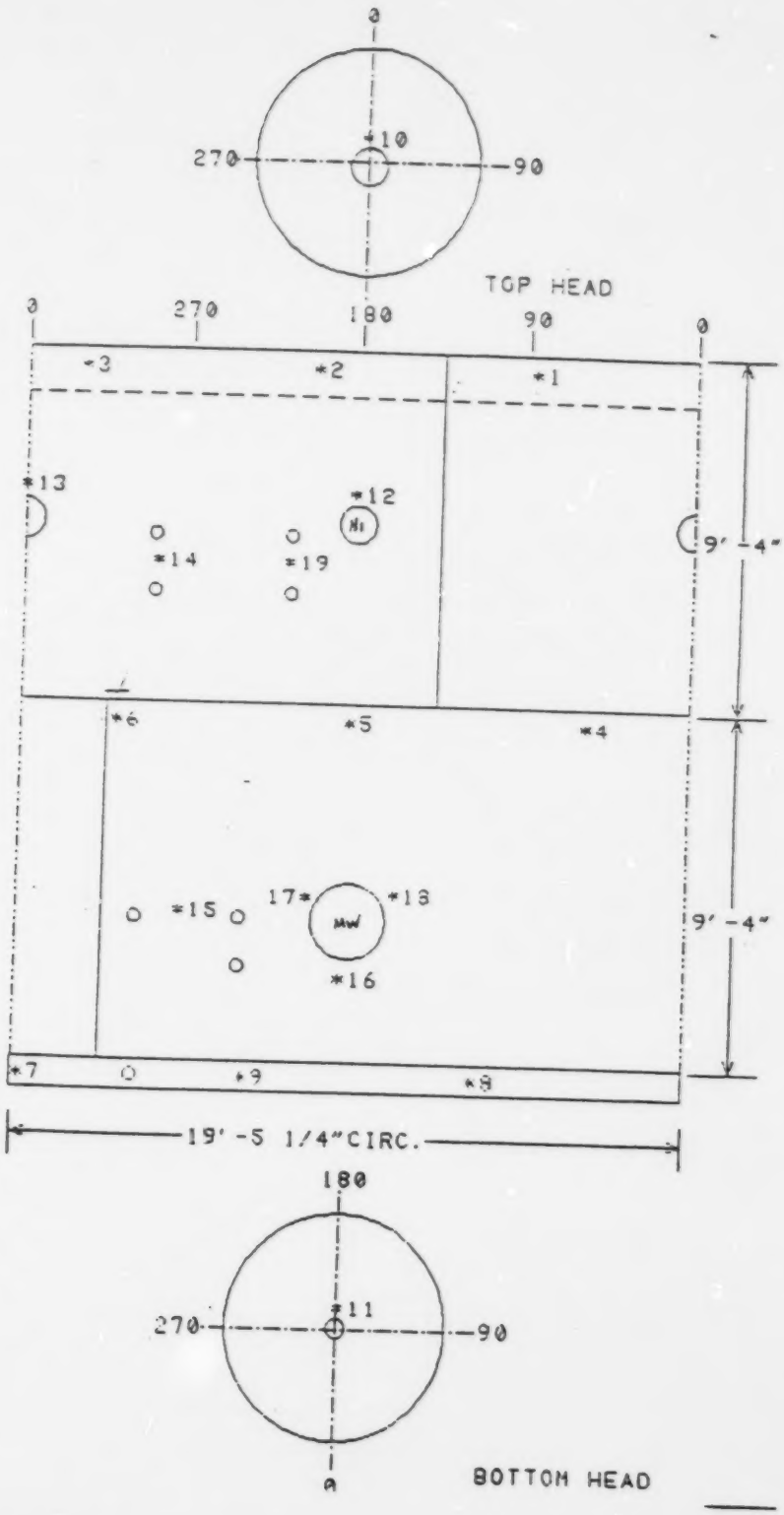

Figure 26: Location of acoustic sensors on vessel

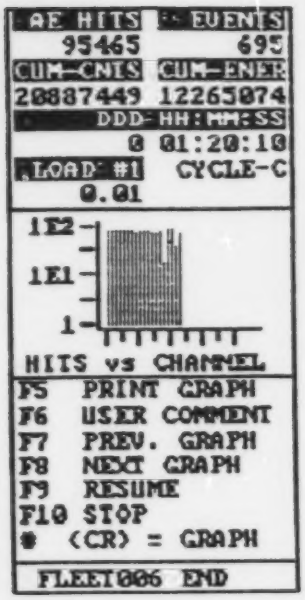

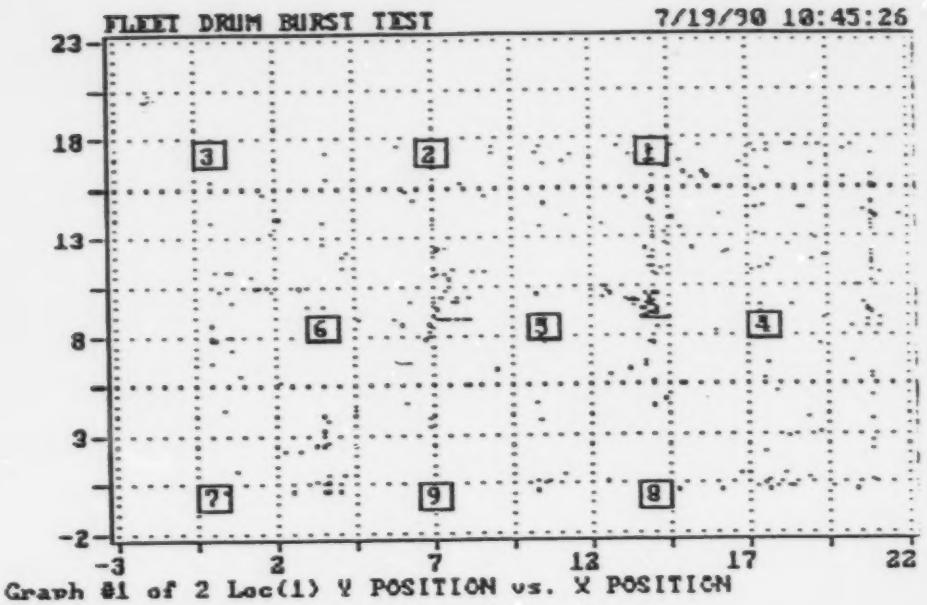

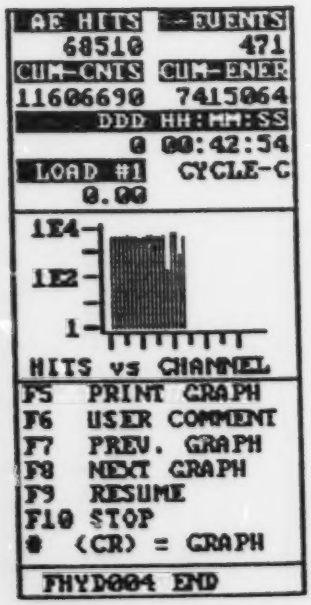

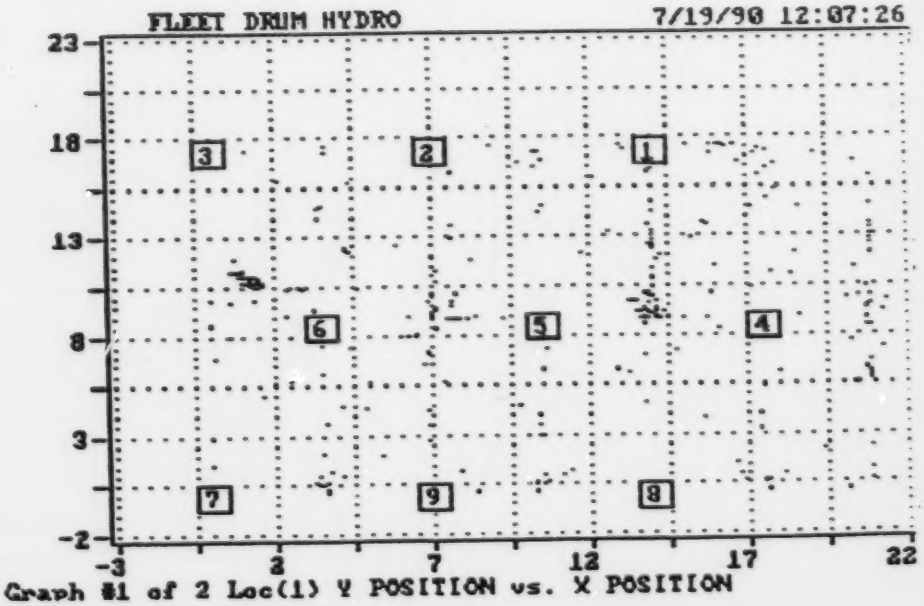

Figure 27: Source location plots - Sensors 1 through 9

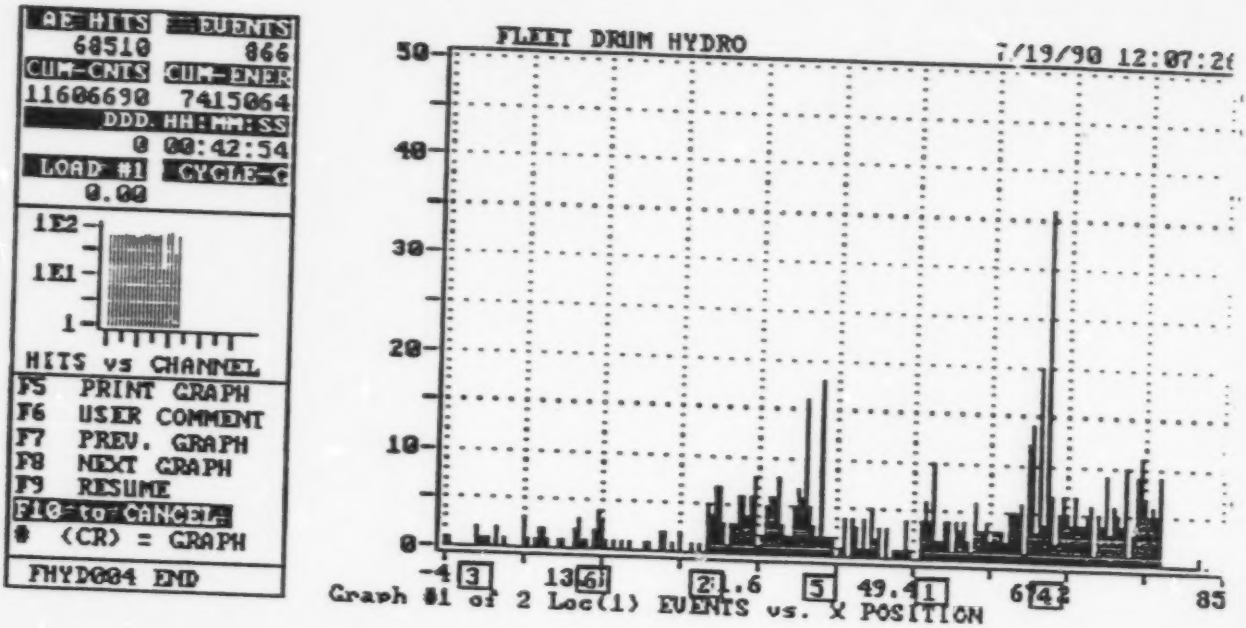

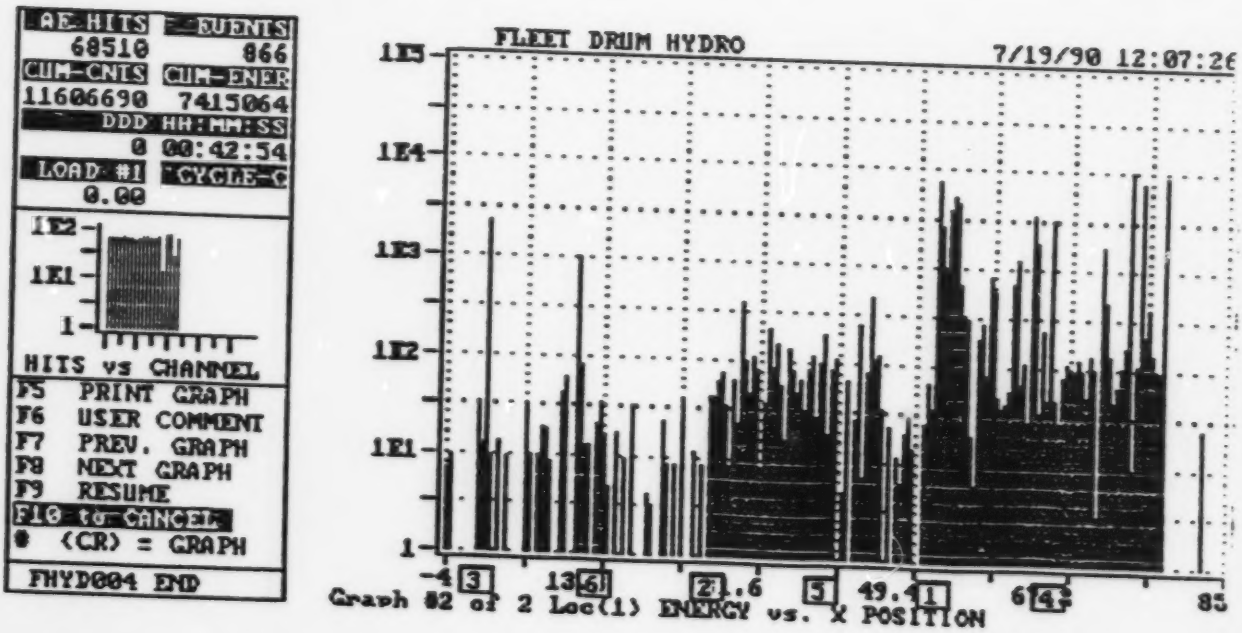

Figure 28a: Acoustic emission events versus sensor (1-6)

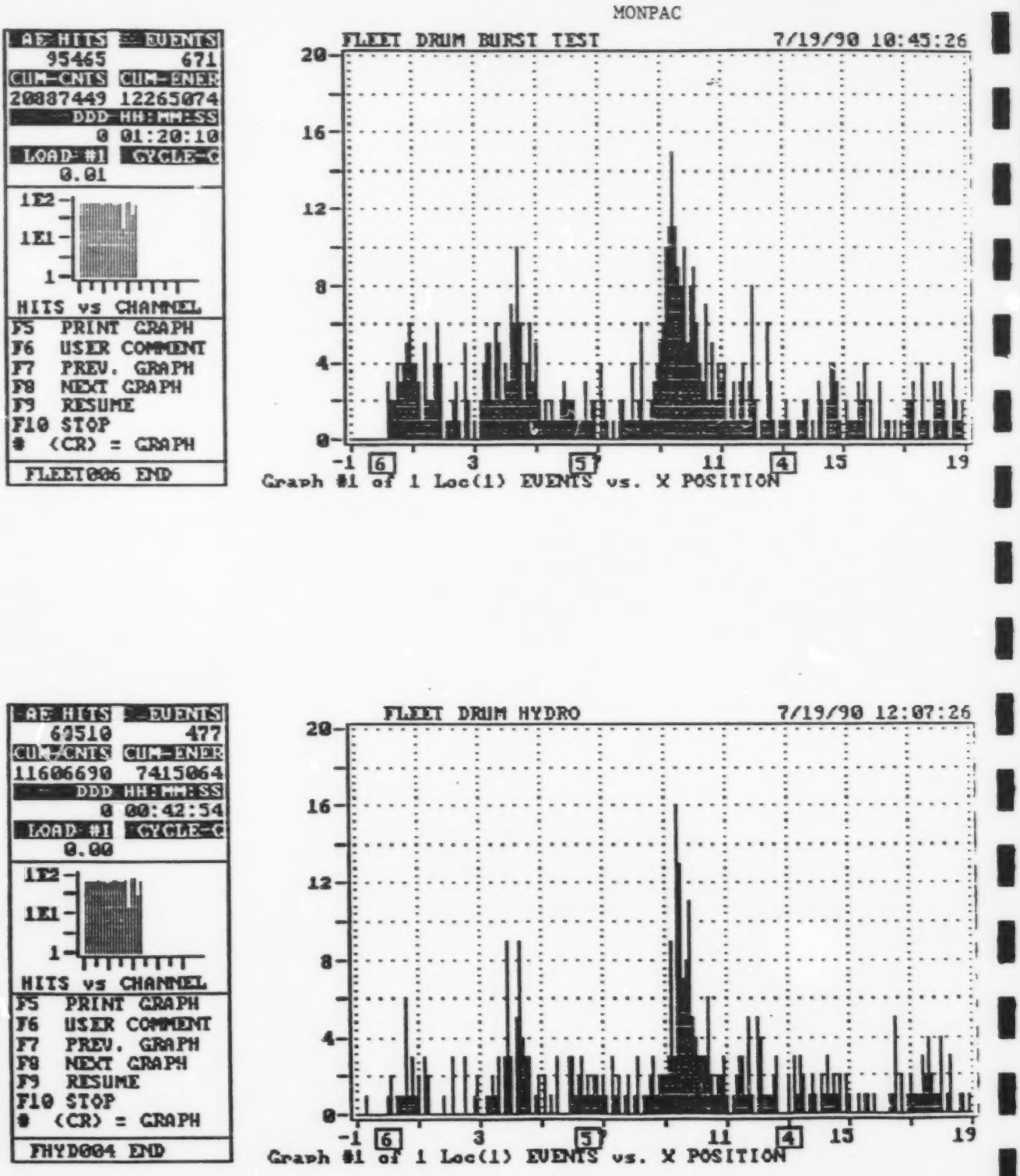

Figure 28b: Acoustic emission events versus sensor (1-6)

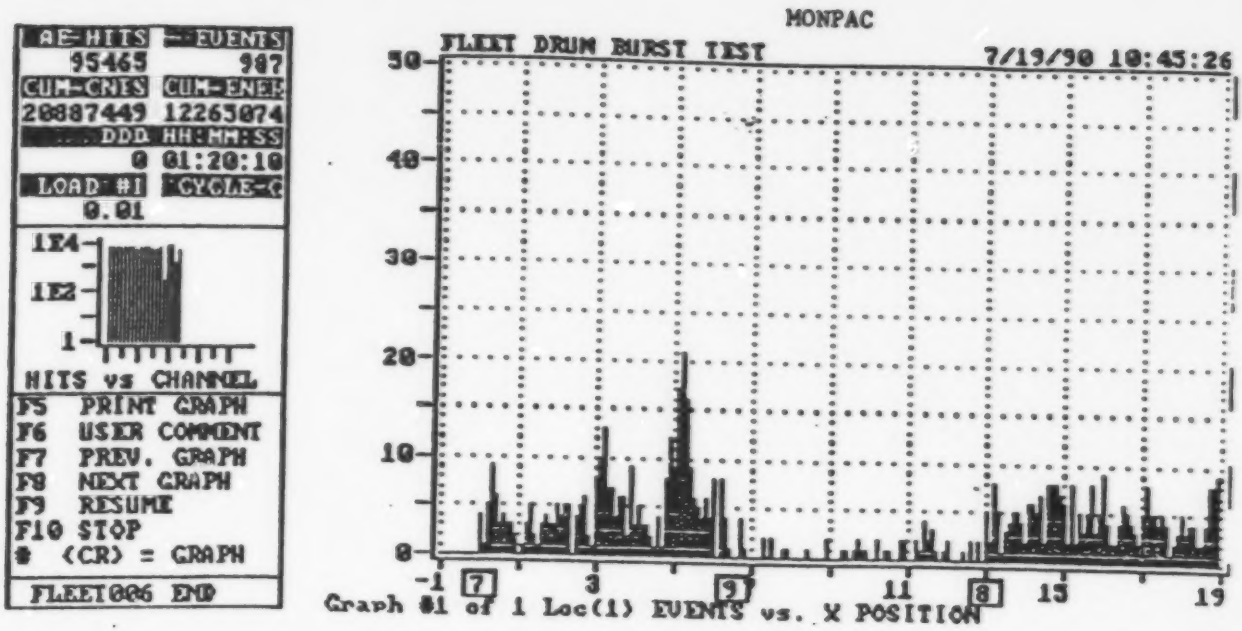

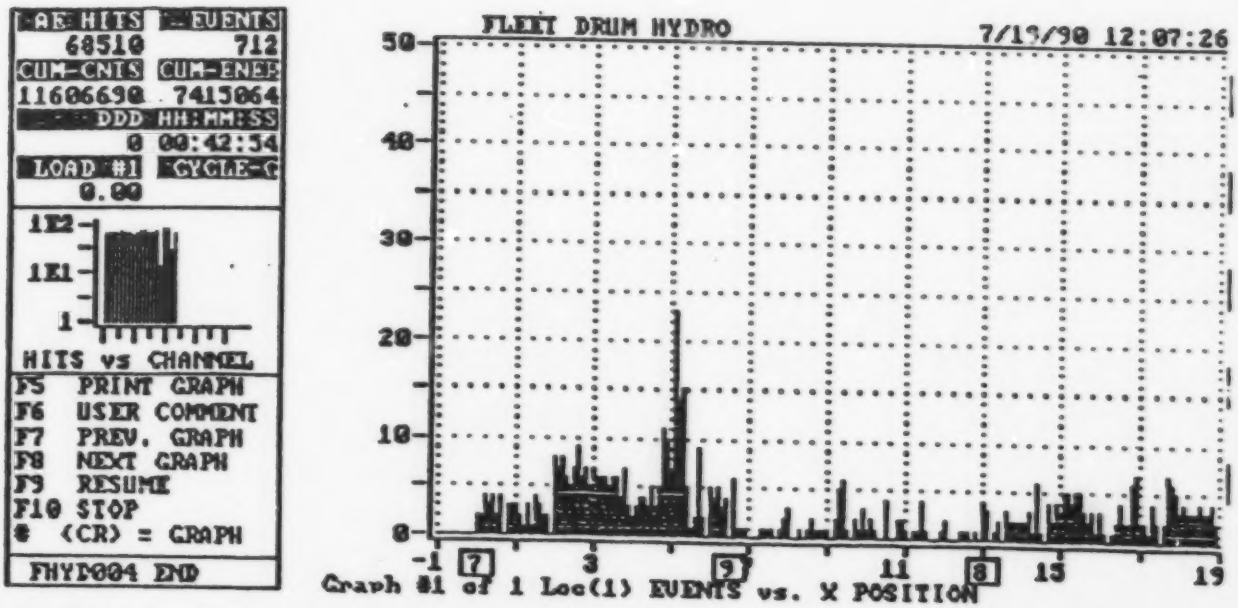

Figure 28c: Acoustic emission events versus sensor (7-9)

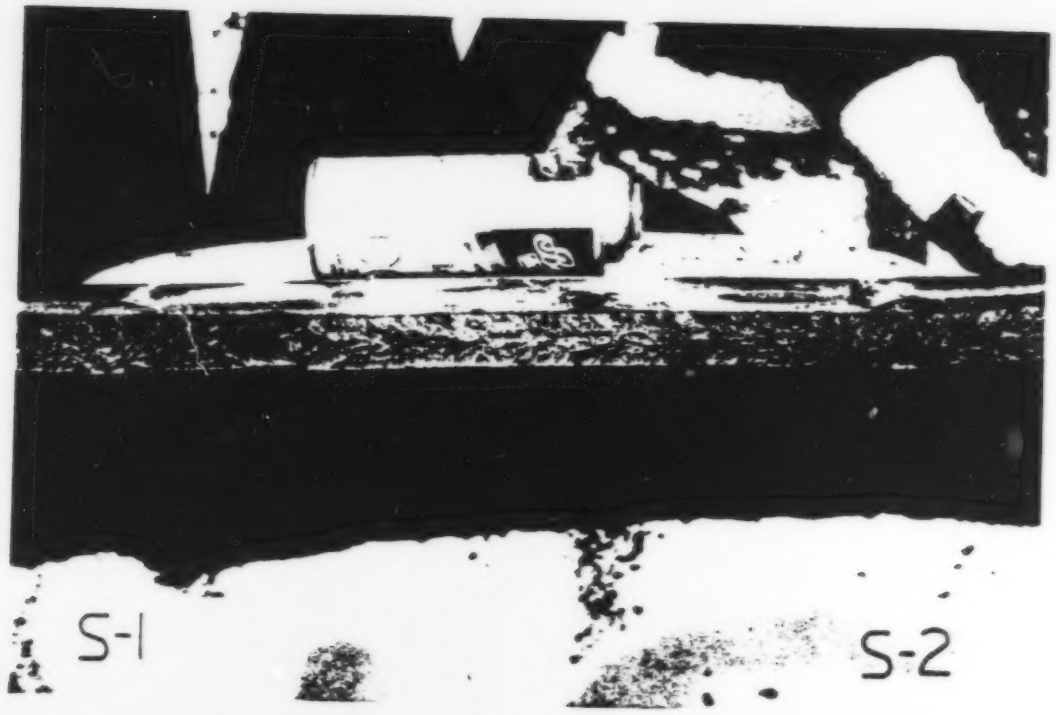

Figure 29: Fracture surface containing the failure initiation site at splitter plate end.

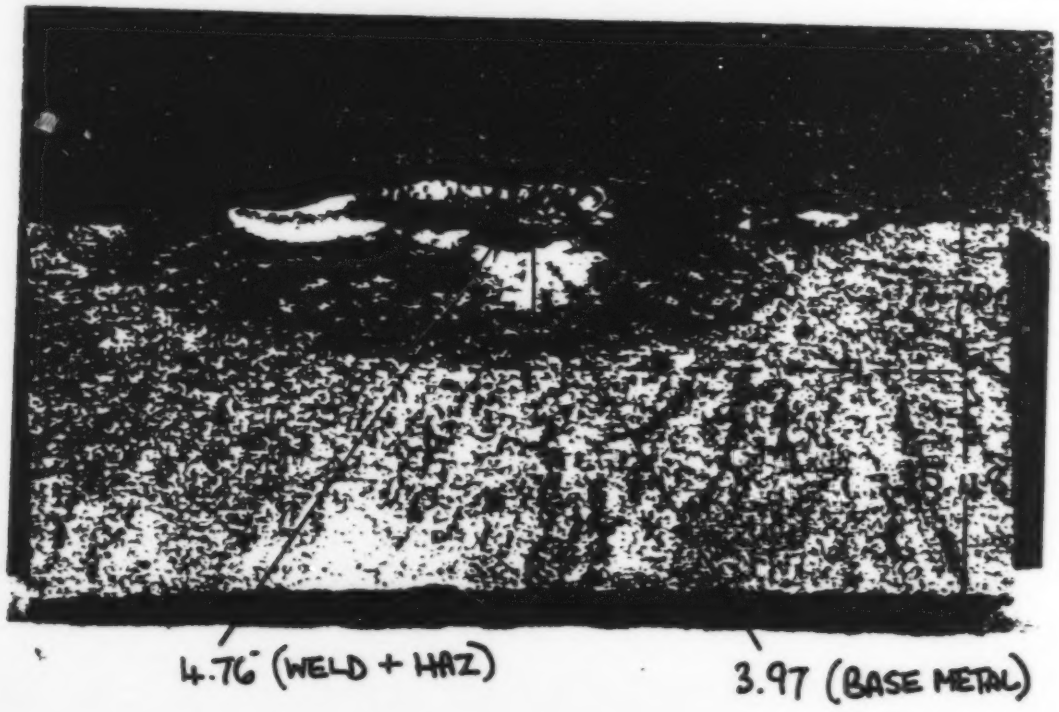

Figure 30: Photomacrograph showing the initial flaw, pop-in and stable tearing at the crack at splitter plate end.

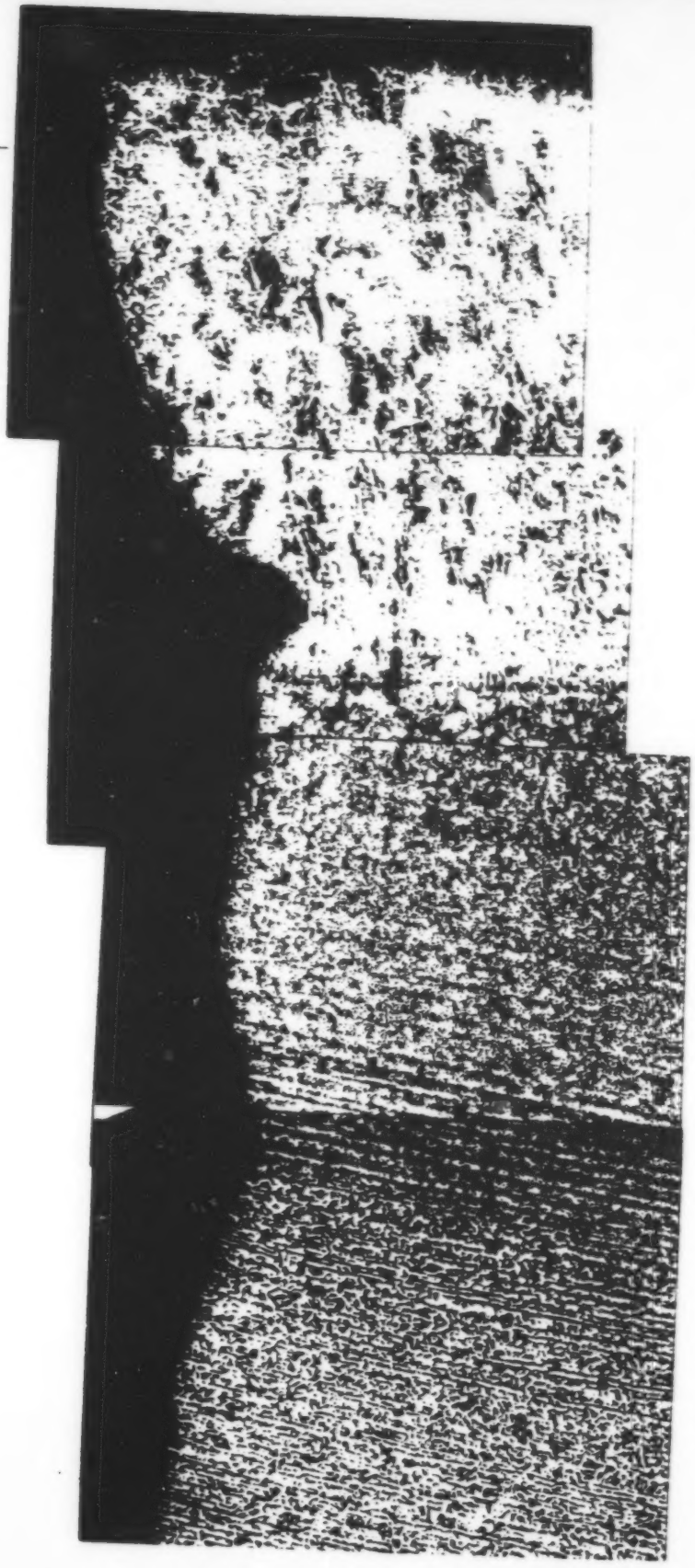

Figure 31: A transverse section through the failure initiation site.

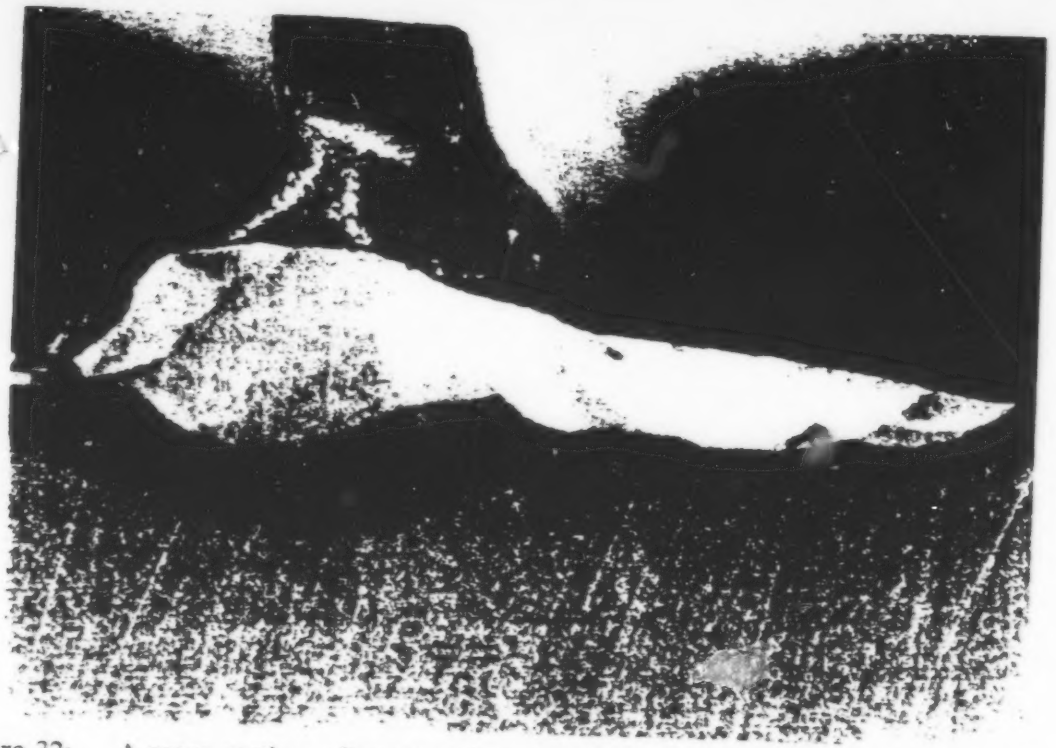

Figure 32: A cross-section adjacent and parallel to the fracture surface at the initiation site, indicating presence of repair weld.

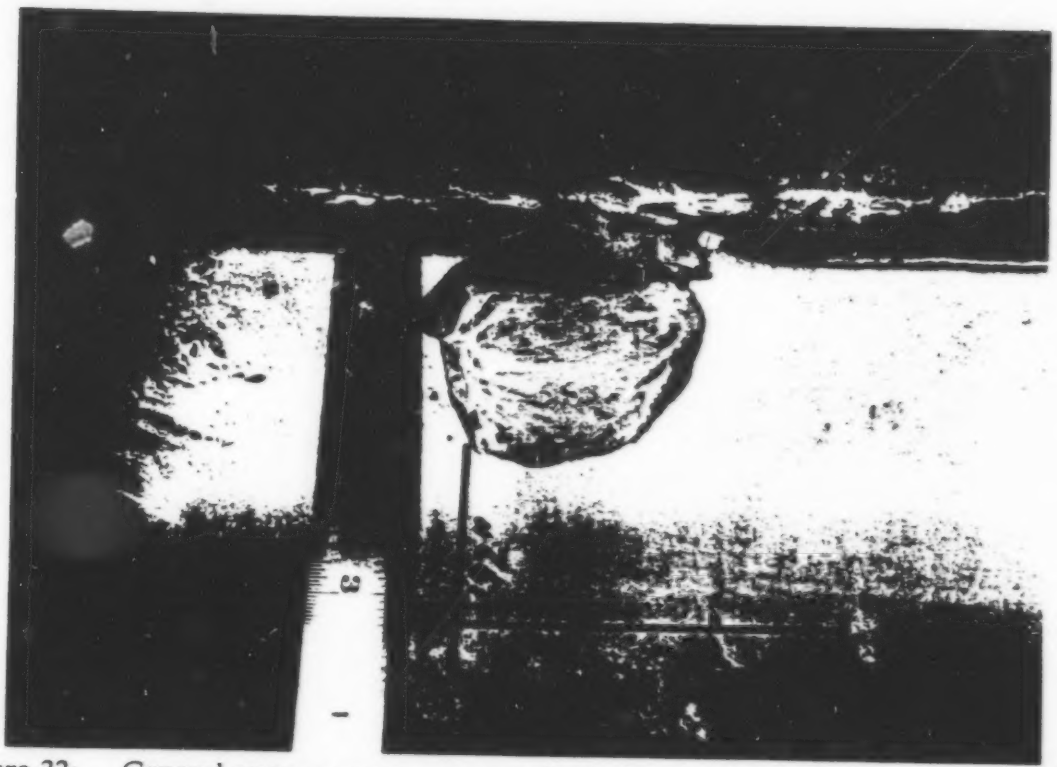

Figure 33: General appearance as macroetched of the weld repair at flaw zone #19.

Figure 34: General appearance of the flaw zone #22 (HAZ cracks in the long weld); see also another repair weld at toe of C3.

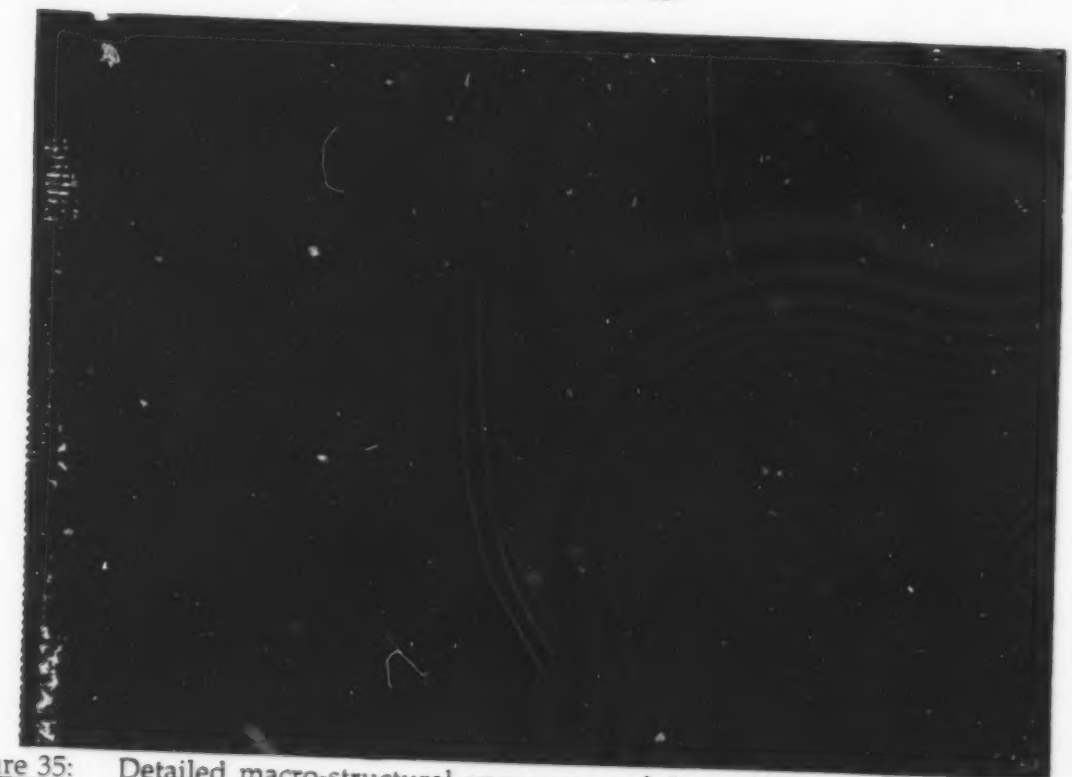

Figure 35: Detailed macro-structural appearance of the welding and cracks at flaw zone #19.

Figure 36: Transverse section through weld toe and crack zone at about 4 o'clock location in Fig. 35 (Mag. X50).

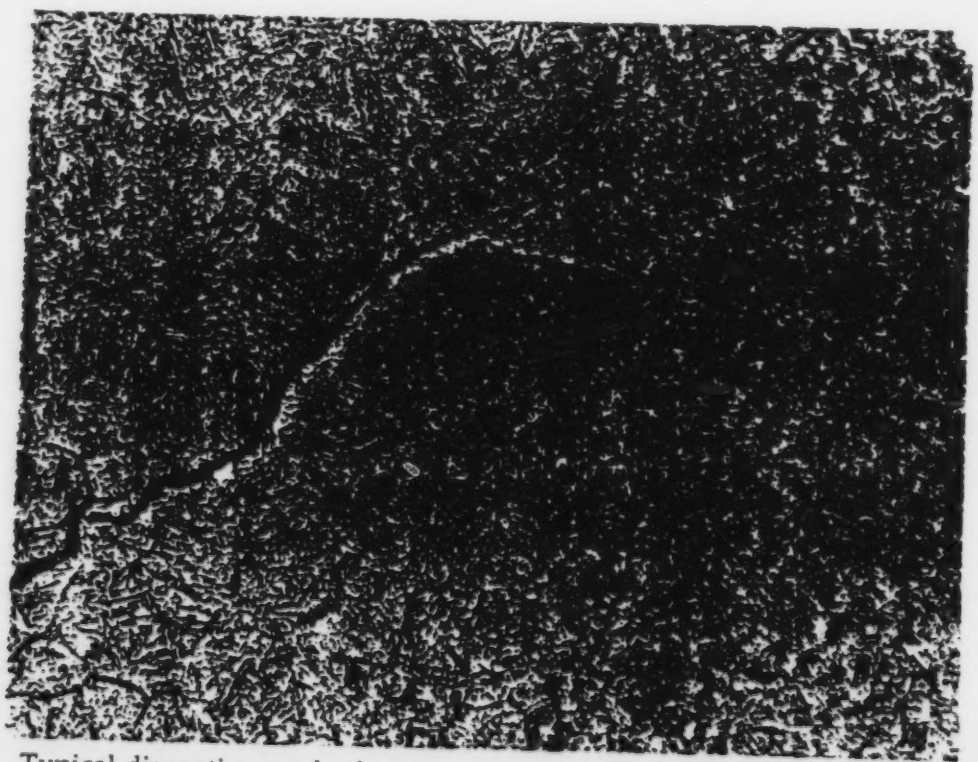

Figure 37: Typical discontinuous hydrogen cracking in the hard size HAZ of weld at flaw #22 (Mag. X100).

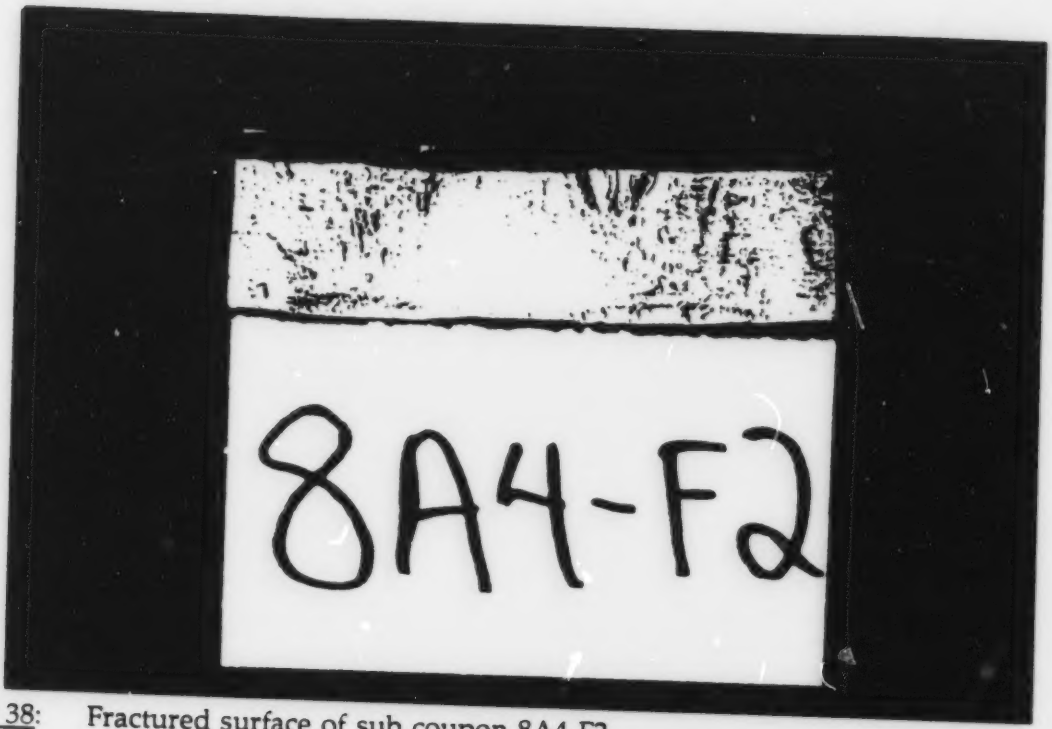

Figure 38: Fractured surface of sub coupon 8A4-F2.

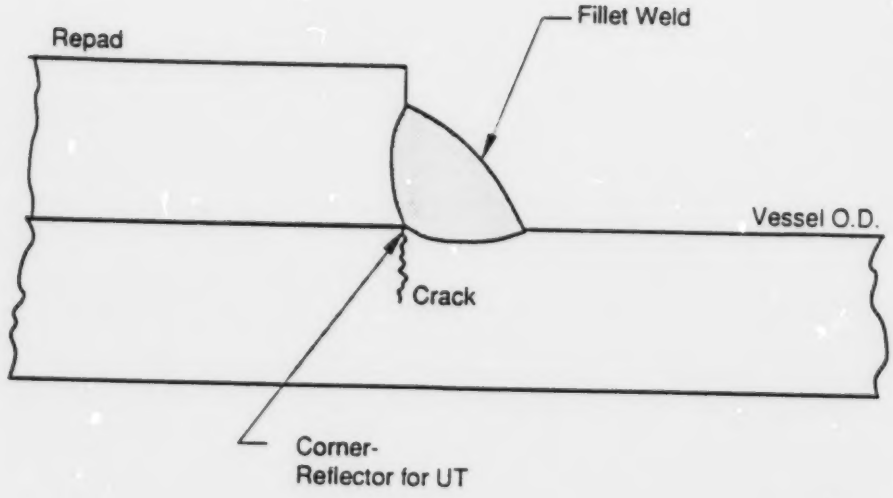

Figure 39: Schematic diagram Showing the Location of Crack at the Manway MWI.

Figure 40: Tearing in the splitter plate indicative of the locally high bending stress.

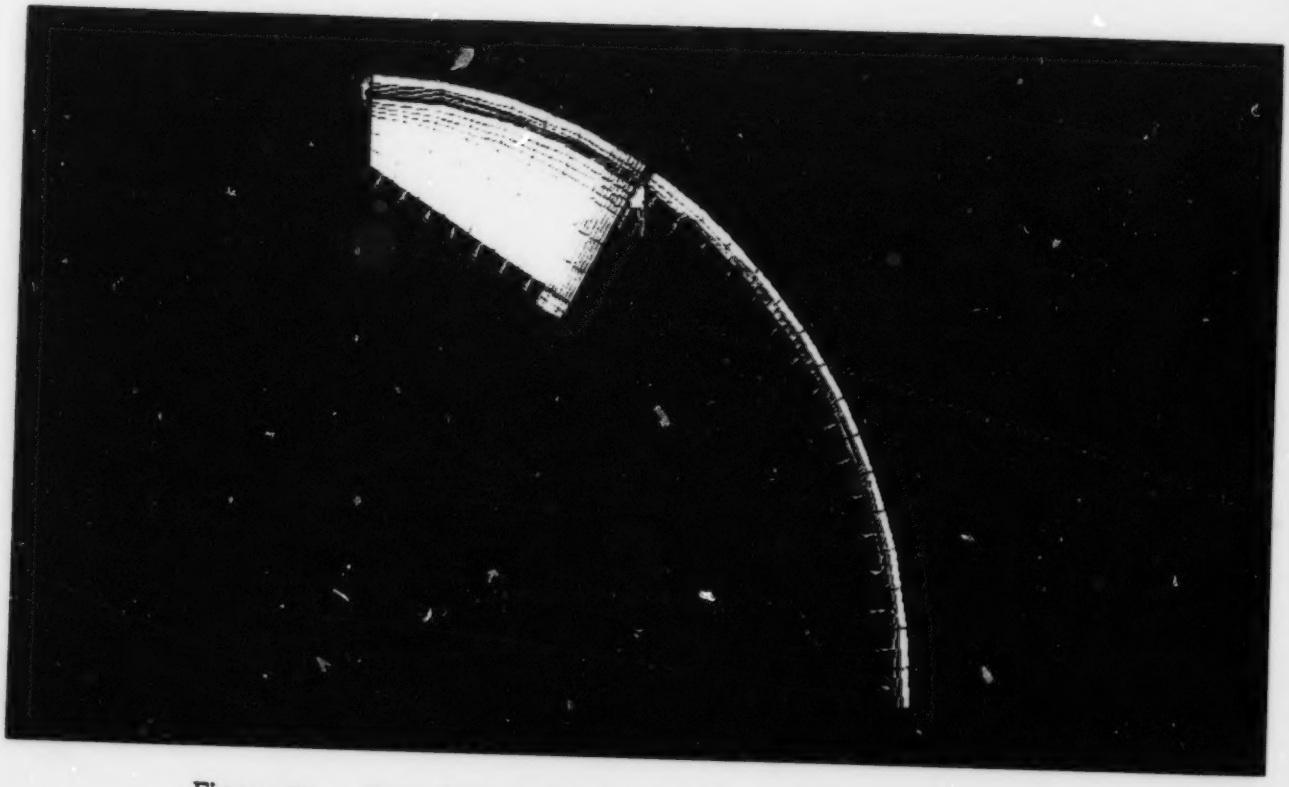

Figure 41: Finite Element Mesh for 2-D Modelling of Splitter Plate

Figure 42(a): Through-Thickness Hoop Stress Distribution at the Splitter Plate End - Shell Region for Uniform Elastic Modulus

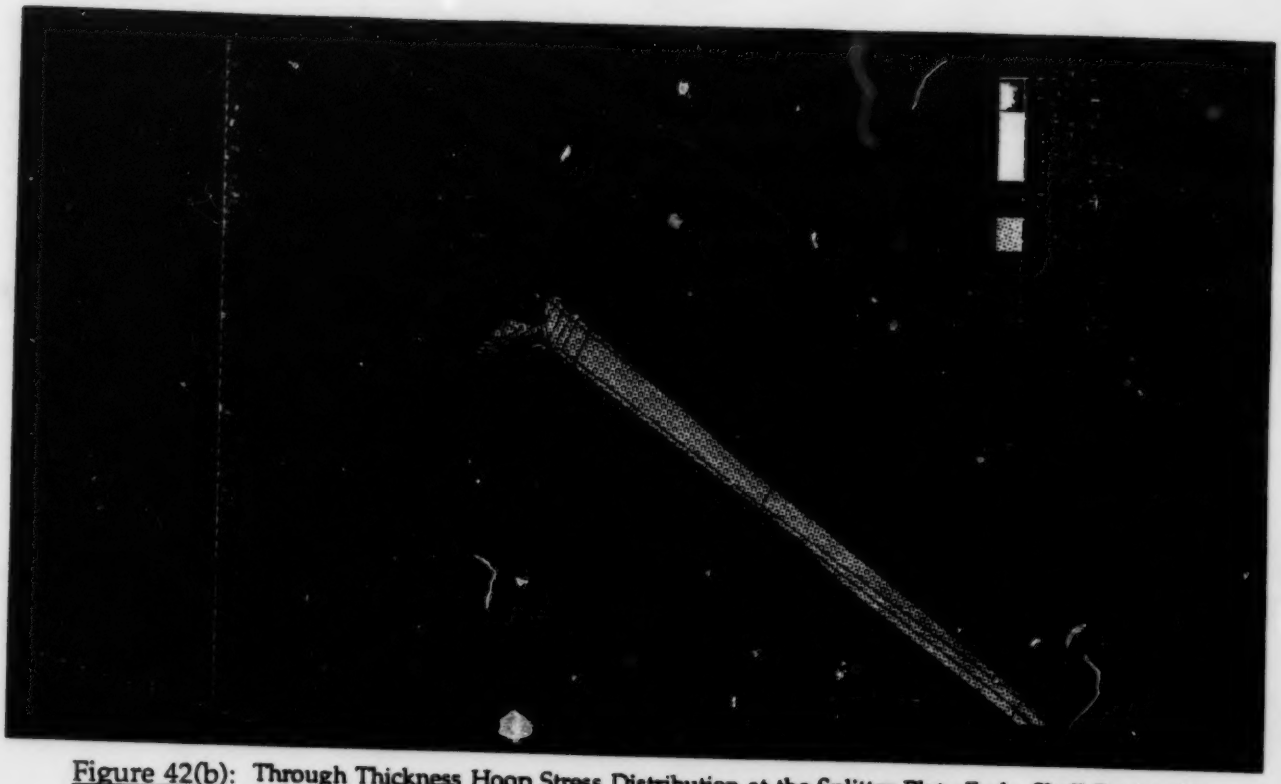

Figure 42(b): Through Thickness Hoop Stress Distribution at the Splitter Plate End - Shell Region for Lower Elastic Modulus in the Splitter Plate Region

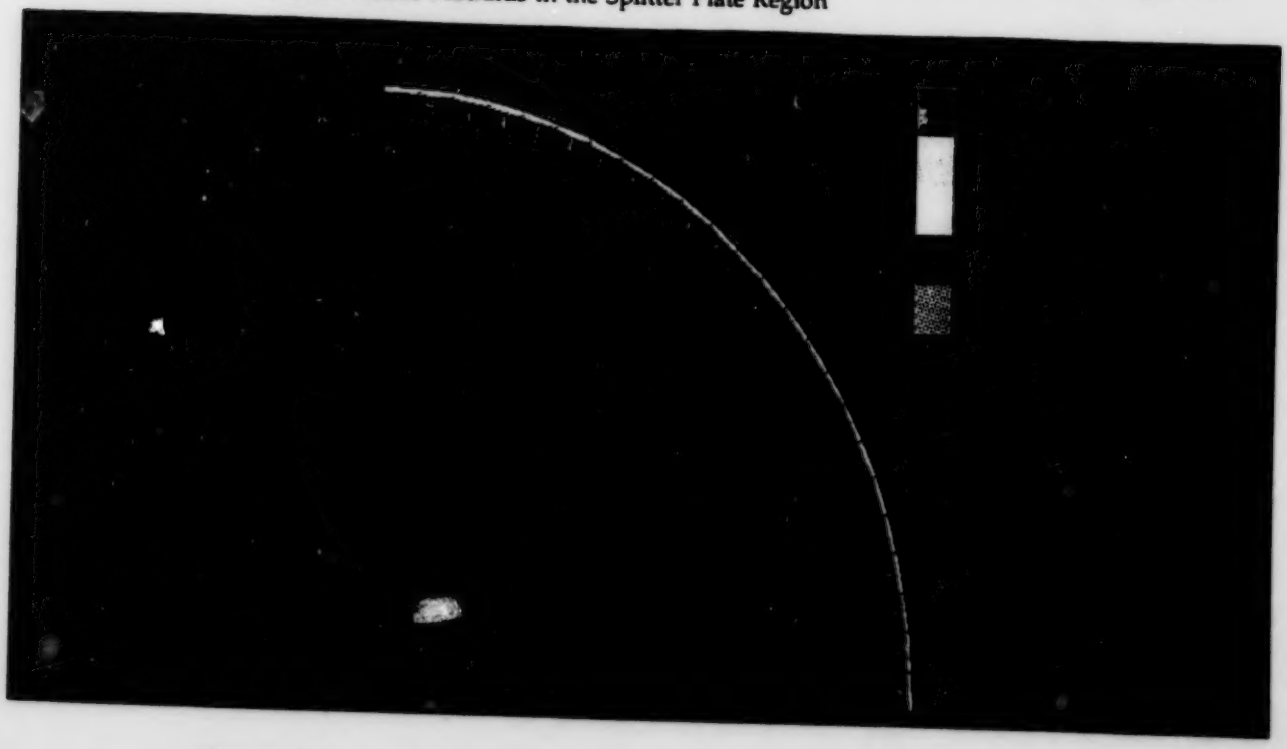

Figure 43: Hoop Stress Distribution in the Absence of Splitter Plate

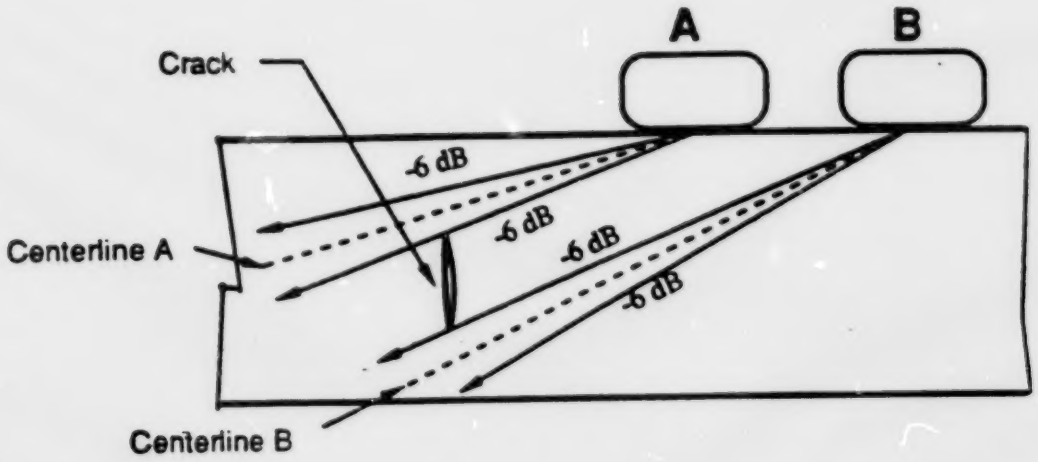

Figure 44: Illustration of source of error in crack sizing using the pulse-echo ultrasonic technique. The accuracy of the method is dependent on the focus of the transducer.